POLITECNICO
MILANO 1863

SCUOLA DI INGEGNERIA INDUSTRIALE
E DELL'INFORMAZIONE

CFD analysis of a motorbike SI engine equipped with a passive pre-chamber

Tesi di Laurea Magistrale in
Mechanical Engineering - Ingegneria Meccanica

Author: **Alessandro Nodi**

Student ID: 968822
Advisor: Dr. Lorenzo Sforza
Co-advisor: Prof. Tommaso Lucchini
Academic Year: 2021-22

Abstract

The complete abatement of carbon dioxide and pollutants emissions on motorcycle spark-ignition (SI) engines is a challenging topic, considering the small size, the low cost and the high power-to-weight ratio required by the market of such powertrain. In this context, the Turbulent Jet Ignition (TJI) technology is an attractive solution. The air-fuel mixture is ignited inside a small volume, called pre-chamber, which releases high-velocity jets of burned gases to the main combustion chamber. This allows to significantly speed-up the combustion process of the closed-valves domain, opening to the possibility of increasing the engine efficiency without penalizing the peak performances. In this thesis, a numerical CFD investigation was carried out on a motorbike SI engine equipped with a passive TJI configuration. The initial part of the thesis work concerned the generation of the fluid domain mesh. The mesh was created such to have a sufficiently fine volume discretization for obtaining accurate results, but at the same time requiring a reasonable computational effort. The focus of the thesis was on the simulation of the gas exchange process in the engine, with specific care given to the flow behaviour inside the pre-chamber and its interaction with the main chamber. An extensive analysis of the trends of the various flow quantities was performed, proving that the simulation results are realistic and consistent with the available experimental data, hence demonstrating the good quality of the numerical setup used. Reliable results of the cold-flow analysis were considered as the essential prerequisite for a proper initialisation of the subsequent power-cycle simulation. The pre-chamber filling and combustion phases were analysed, showing the dependency of the hot gas ejection process from the flow field inside the pre-chamber. Promising results were obtained also from the simulation of the combustion process, but further investigations are necessary to better understand what caused the discrepancies between numerical and experimental results.

Keywords: CFD, internal combustion engine, Turbulent Jet Ignition, passive pre-chamber

Abstract in lingua italiana

Il completo abbattimento delle emissioni di anidride carbonica e sostanze inquinanti è un tema particolarmente sfidante per i motori motociclistici, considerando la loro piccola taglia, il basso costo e l'elevato rapporto potenza-peso che il mercato richiede per questo tipo di propulsori. In questo contesto, la tecnologia Turbulent Jet Ignition (TJI) è una soluzione attraente. La miscela aria-carburante viene accesa all'interno di un piccolo volume, chiamato pre-camera, che causa il rilascio di getti di gas combusti ad alta velocità nella camera principale. Questo permette di aumentare notevolmente la velocità di combustione nel cilindro, aprendo alla possibilità di un miglioramento del rendimento del motore senza penalizzarne le prestazioni. In questa tesi è stata svolta un'investigazione numerica di CFD su un motore ad accensione comandata di una moto, equipaggiato con una tecnologia TJI nella sua configurazione passiva. La parte iniziale di questo lavoro di tesi ha riguardato la generazione della mesh del dominio fluido. La mesh è stata creata in modo da avere un volume con una discretizzazione sufficientemente fine per ottenere risultati accurati, ma allo stesso tempo che richiedesse un tempo computazionale ragionevole. La tesi è stata incentrata principalmente sulla simulazione di ricambio fluido nel motore, con un occhio di riguardo per il comportamento del flusso all'interno della pre-camera e la sua interazione con la camera principale. É stata condotta un'estesa analisi dell'andamento delle varie quantità che caratterizzano il flusso, provando che i risultati della simulazione sono realistici e consistenti rispetto ai dati sperimentali a disposizione, dimostrando quindi la buona qualità del setup numerico utilizzato. Risultati affidabili dell'analisi di ricambio fluido sono stati considerati come un prerequisito essenziale per una corretta inizializzazione della seguente simulazione del ciclo attivo. Sono state analizzate le fasi di riempimento e combustione in pre-camera, mostrando la dipendenza del processo di espulsione dei gas dal campo di moto nella pre-camera. Sono stati ottenuti risultati promettenti anche dalla simulazione del processo di combustione, ma ulteriori investigazioni sono necessarie per una migliore comprensione delle cause della discrepanza tra risultati numerici e sperimentali.

Parole chiave: CFD, motore a combustione interna, Turbulent Jet Ignition, pre-camera passiva

Contents

Introduction

In the following years are expected more restrictive regulations concerning greenhouse gases and pollutant species emissions to become law in all the countries of the European Union, in order to prevent a worsening of the global warming phenomenon and to reduce the concentration in the air of harmful chemical species for humans health.
This situation is pushing the internal combustion engines manufacturers to find innovative technical solutions to further reduce the tailpipe emissions of carbon dioxide (CO_2) and pollutant species, such as carbon monoxide (CO), unburned hydrocarbons (HC), nitrogen oxides (NO_x) and soot.
In the past years, a remarkable improvement of the after-treatment systems in the automotive sector led to a significant reduction of all pollutants. For motorcycle engines, it is becoming increasingly difficult to comply with the current and future more severe emissions regulations, especially considering the need of keeping small-size high-performance engines, avoiding to install bulky after-treatment systems. Figure 1 shows the evolution of the pollutant emissions regulations in the last twenty years. Moreover, the upcoming regulations will enforce not only a further reduction of harmful emissions, but also a much stronger limit regarding the greenhouse gases emissions, especially for the CO_2. The most effective way of reducing the emissions of CO_2 is to burn fuels containing a low or null amount of carbon, such as hydrogen, ammonia and other types of e-fuels. Nevertheless, for all the fuels containing carbon, one of the most convenient strategies is to reduce the engine fuel consumption. Therefore, nowadays an important effort is put on the research of new solutions to improve the engines efficiency, which is beneficial for any kind of fuel.

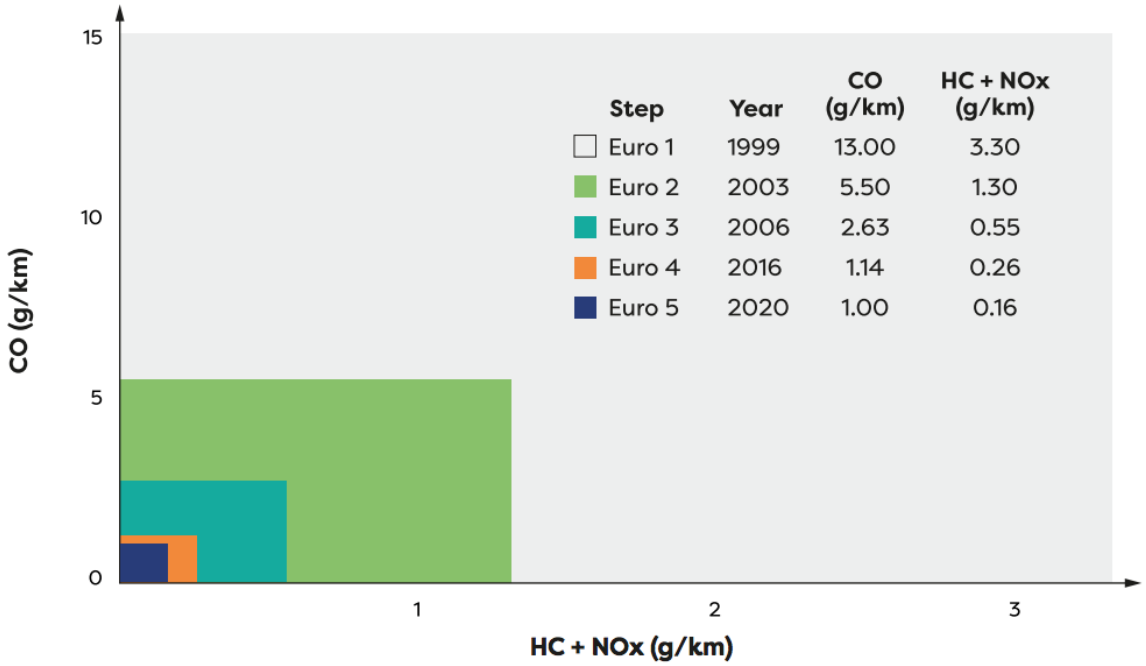

Figure 1: Development of EU motorcycle legislated emissions limits (source: AECC)

Several solutions were studied in the past to increase the brake thermal efficiency by applying advanced combustion modes. Some of the most attractive are the HCCI (Homogeneous Charge Compression Ignition) combustion, the RCCI (Reactivity Controlled Compression Ignition) combustion, or the CAI (Controlled Auto-Ignition) combustion. Among the innovative combustion strategies, one of the most promising is the Turbulent Jet Ignition (TJI) [9].

This solution consists of a combustion pre-chamber applied on the cylinder head in place of the spark plug, which is installed inside it. The pre-chamber is connected to the main combustion chamber through a series of orifices. The air-fuel mixture is ignited by the spark plug and the consequent combustion development significantly increases temperature and pressure in the pre-chamber. The pressure difference between pre-chamber and main chamber leads to the release of extremely hot turbulent jets flowing through the orifices into the main chamber. The ejection process causes the ignition of the air-fuel mixture inside the cylinder simultaneously from several spots. This ignition technology leads to a very fast combustion, with a remarkable reduction of the cyclic variability. An example of combustion pre-chamber in its active configuration is shown in Figure 2.

The studies on this technology are mainly focused on optimizing both the pre-chamber design and the engine operating conditions, in order to achieve Diesel-like brake thermal efficiencies.

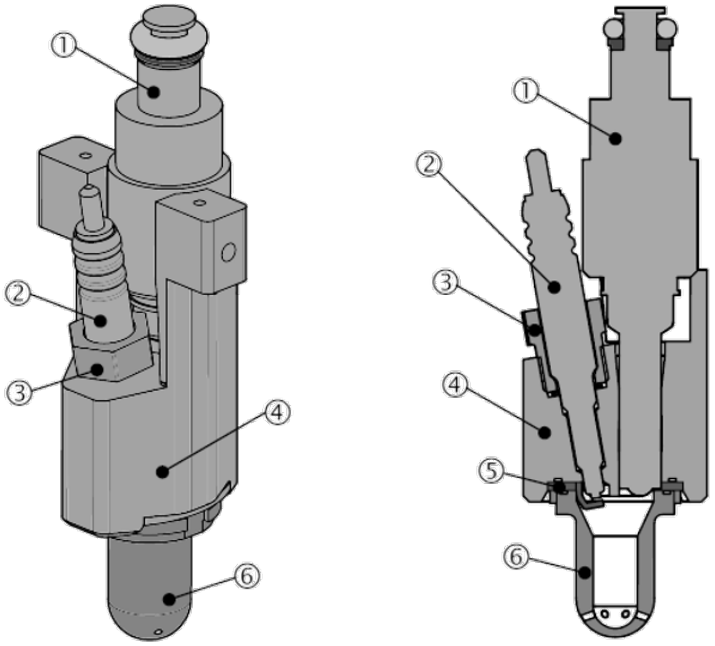

Figure 2: Example of an active pre-chamber [25]

Focusing on the passive pre-chamber configuration, its low cost and easy addition to engines already in production represent attractive features for automotive and motorcycle engines manufacturers, to improve their powertrains performances.
A passive pre-chamber has already been used in the last years on the high-performance turbocharged F1 engines, proving its great potential to increase the engine efficiency.
More details on the passive pre-chamber ignition technology and its impact on the engine performances, according to results available from literature, are described in Chapter 1.

Experimental investigations are fundamental to have a clear idea about the performances of an engine equipped with a pre-chamber. However, the results are not always straightforward to understand, therefore it can be very useful to resort to 3D CFD simulations. In fact, a numerical analysis could provide a better understanding of the flow behaviour inside the engine, clarifying the variations of the engine performances when a pre-chamber is applied. Therefore, a combined experimental-numerical investigation is fundamental for optimizing the pre-chamber geometrical features and the engine operative parameters to

obtain a more stable and efficient operation on the whole engine map.

This thesis work is focused on the numerical study of a passive pre-chamber solution, mounted on an already existing motorbike SI engine. The target is to clarify the behaviour of a selected geometry in terms of scavenging and engine performances, to support future experimental investigations. At this time, no applications of the TJI technology on a motorbike engine are available in literature.
The numerical simulations were carried out by using the open-source CFD code OpenFOAM, modified and integrated with dedicated libraries developed by the ICE group of Politecnico di Milano. The experimental data of the investigated pre-chamber configuration were provided by Marmotors s.r.l., which performed a preliminary measurement campaign.
A brief discussion about the theory behind the Computational Fluid Dynamics (CFD) is presented in Chapter 2. In Chapter 3 some more information are given about the engine subject of this thesis work, supported by a summary of the findings resulting from the experimental test campaign.

The description of the operative part of this thesis work starts from Chapter 4, where it is illustrated in detail the procedure followed to obtain the setup for the subsequent cold-flow and combustion simulations, with a focus on the mesh generation methodology, the assessment of the adopted initial and boundary conditions, as well as the selected numerical discretization schemes for the simulations.
In Chapter 5 the most significant results of the cold-flow simulation are presented and extensively analyzed, investigating the simulation outcomes inside the main chamber and the pre-chamber. The available experimental data are taken as benchmark for the most important quantities in order to assess the quality of the numerical results.
The availability of reliable results from the gas-exchange simulation is fundamental for a proper prediction of the power-cycle. Few preliminary reacting results are illustrated in Chapter 6, obtained by means of a novel approach to simulate combustion in the OpenFOAM framework.

1 | Passive pre-chamber internal combustion engines

Nowadays, the interest in the application of a passive or active pre-chamber on internal combustion engines is growing more and more. A passive pre-chamber is mounted on F1 cars engine since last 8-9 years and it is one of the key technologies that allows to reduce the fuel consumption of such power units. This helps manufacturers to comply with the recently introduced regulation limits related to fuel flow rate and maximum amount of fuel per-race that can be carried [4].
Currently, some engine manufacturers of the automotive and motorcycle industries are investigating the potential benefits of the addition of a combustion pre-chamber also on mass production engines. The final goal of the application of a pre-chamber ignition system on an internal combustion engine consists in increasing the efficiency thanks to an improved combustion process. The rise in engine efficiency may be either converted in emissions reduction or in performance improvement, depending on the final use of the engine (road or motorsport).

The pre-chamber technology is not a completely new concept. Similar ideas for spark ignition engines were already proposed in the past (e.g. torch ignition from Gussak [13]; APIR from Robinet et al. [20]; bowl pre-chamber ignition from Kettner et al. [15] and some others [27]), but were never fully developed nor efficiently exploited because of a lack of deep knowledge about the physical and chemical phenomena characterizing the combustion of an engine equipped with such technology. This aspect prevented their use on commercial engines. The poor knowledge of the processes happening inside the engine cylinder and pre-chamber was due to the fact that in the past the only available data were obtained by means of experimental tests, and merely from these data it is not possible to extensively learn about the thermo-fluid-dynamic behaviour of the gas inside the engine. At present day, thanks to the impressive development of CFD softwares and methodologies that took place approximately in the last thirty years, it is possible to study in much more fine detail the gas flow between pre-chamber and main chamber, paying close

attention to the combustion and jets ejection processes, so this is the main reason why a renewed interest in pre-chamber ignition is growing in these years.

The most modern application of a pre-chamber for improving combustion of spark ignition engines is called TJI (Turbulent Jet Ignition) and its development at a research level began less than twenty years ago (the project from Mahle powertrain was one of the first known tests [1]). After successful use in motorsport high-performance turbocharged car engines, the benefits that TJI technology can guarantee are becoming of great interest also for motorcycle engines and passenger car engines, with the aim of reducing fuel consumption and emissions thanks to the potential advantages of the combustion enhancement provided by the introduction of this system. At this time, there is only one known production car engine with a pre-chamber ignition technology, which is the Maserati Nettuno 3.0L twin-turbo V6 engine. In this application the passive pre-chamber is integrated in a quite complex and expensive engine architecture, featuring two spark plugs and two injectors for each cylinder (both PFI and DI), in order to try to optimize the engine behaviour with a pre-chamber for the whole engine map, avoiding possible problems related to combustion stability and emissions, especially at low loads [2].

In this context, it is worth to mention the main features and differences of active and passive pre-chambers, in order to better understand the potentiality of the application of a passive pre-chamber on an engine.
The main characteristic of engines where an active pre-chamber is applied is the capability of having different air-fuel ratios inside pre-chamber and main chamber, thanks to two different fuel injectors. This feature is generally exploited in order to ignite a very lean mixture inside the main chamber thanks to the high ignition energy that the flame fronts coming out from the pre-chamber can guarantee, while in the pre-chamber a stoichiometric mixture is easily ignited by the spark plug. Hence, this solution allows to overcome the usual flammability limit of lean mixtures, allowing to burn much leaner mixtures inside the main chamber compared to conventional SI engines, with the main target of considerably reducing combustion temperature and pollutant emissions. However, the application of an active pre-chamber on a commercial engine will increase its cost and complexity, since there will be two fuel injectors for each cylinder and a further cost increase will be caused by the need of applying special after-treatment systems to deal with the emissions of a lean combustion (i.e. high amount of NO_x and almost null amount of CO and HC), since conventional three-way catalytic converters are not compatible for lean operation.
On the other hand, passive pre-chambers are very simple and cheap, since they can be screwed on the cylinder head exactly like it is usually done for a conventional spark plug,

and therefore also occupying almost the same space. A passive pre-chamber can be rather easily produced featuring an external thread to be mounted on the engine head and also a threaded hole to host the spark plug. The volume between these two features can be produced with the desired shape and will be in connection with the main chamber through the holes machined on the bottom of the pre-chamber.
Moreover, engines with this kind of pre-chamber will keep working with a near stoichiometric air-fuel ratio, making it compatible with conventional after-treatment systems [9]. The advantages of the passive pre-chamber on combustion efficiency are still very relevant and will be discussed in the following sections. The latter characteristics make this technology interesting for research and development oriented to a short term application avoiding an excessive production cost increment and minimizing changes to already existing SI engines architecture [7]. Figure 1.1 shows a very basic representation of an engine equipped with an active and passive TJI system, clarifying the differences between the two.

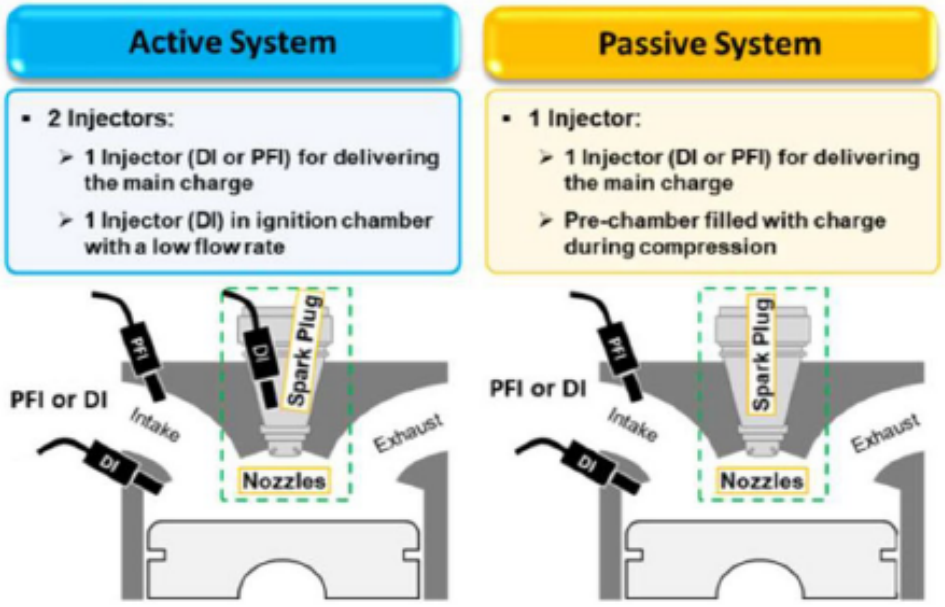

Figure 1.1: Schematic representation of an engine with active or passive pre-chamber [8]

1.1. Pre-chamber main features and operation

The combustion pre-chamber is a small volume connected to the main chamber through one or more channels. A pre-chamber is called "passive" if it is the housing just for the spark plug, whereas it becomes "active" if it also contains a fuel injector. Modern pre-chambers are connected to the main chamber by several orifices, usually in a number that varies from four to eight. The pre-chamber volume can be in the order of 2-8% with re-

spect to the main chamber clearance volume, but usually small pre-chambers are preferred to obtain ideal performance. The higher is the volume of the pre-chamber, the more is the mass trapped inside it and thus the higher will be the energy available for the ignition of the mixture in the main chamber. On the other hand, with a big pre-chamber there will be a greater amount of air-fuel mixture burnt without directly producing a force against the piston, but just needed for the ignition of the main charge. The pre-chamber volume is generally tuned by adjusting its height, since the diameter is generally constrained by the engine head geometry. It also has to be considered that if the pre-chamber is too tall the scavenging process will become more difficult and the risk of having residual gases close to the spark plug electrodes that might inhibit the starting of combustion is not negligible.
The main geometrical characteristics of the pre-chamber are: diameter, height, number of orifices, orifices diameter, orifices length and orifices orientation. To exploit in the best possible way the advantages that the use of a passive pre-chamber can provide, all of these parameters must be finely tuned to find the best combination. Looking at the results of several researches ([3, 18, 24, 25]), it can be concluded that there are not some optimal parameters for the whole engine operating map, thus the pre-chamber is generally optimized only for certain ranges of engine speed and load.

Differently from a traditional spark ignition engine, combustion does not start inside the main chamber, but inside the pre-chamber. After the spark ignition, the combustion quickly burns all the available air-fuel mixture inside the pre-chamber, then the flame front moves through the orifices and finally highly turbulent hot jets propagate into the main chamber. This behaviour allows to ignite the air-fuel mixture inside the main chamber from multiple ignition spots at the same time and significantly increases the flame front surface and turbulence, therefore reducing the combustion duration and improving its stability compared to a traditional SI engine where ignition starts from just one point inside the main chamber in correspondence of the spark plug. The air-fuel ratio is homogeneous between main chamber and pre-chamber, because the pre-chamber filling takes place mainly during the compression stroke where the piston pushes inside the pre-chamber the fresh charge already entered in the main chamber during the intake stroke.
The peculiarity of the TJI system is that the pre-chamber flame front is quenched when it flows through the orifices due to their small diameter, therefore the ignition of the fresh charge in the main chamber is caused by the high temperature intermediate reaction products ejected from the nozzles [5, 30]. In some conditions the jets can contain not only high temperature active radicals, but also wrinkled turbulent flames [29]. This is one of the features that differs the TJI system from the old torch ignition, where there was just

a flame front coming out from the pre-chamber, because it was connected to the main chamber through a hole of a much bigger diameter.
To obtain the desired behaviour of the jets, the parameter that governs the flame fronts quenching is the nozzles diameter: if the diameter is too small the flow becomes chocked, thus reducing the ignition energy; on the other side, if the diameter is too big the jets will only include flames generating an ignition system similar to the torch ignition, which is less effective compared to the high-velocity and high-turbulence jets of active radicals typical of TJI. The nozzles diameter dictates the flow outlet velocity from the pre-chamber orifices and hence also the jets penetration in the main chamber.
The diameter and the number of orifices have an important role also for what concerns the pre-chamber scavenging. The ratio between total surface of the holes and volume of the pre-chamber must be properly tuned to obtain the best compromise between pre-chamber filling and ignition energy. If the orifices diameter is too high, the pre-chamber scavenging will be good, but the velocity and penetration of the combustion jets will be sacrificed, thus reducing combustion velocity. Vice-versa, if the orifices diameter is too low, the pre-chamber scavenging will be hindered due to a higher pressure drop when the fluid flows through the nozzles. Moreover, also the space available on the bottom of the pre-chamber has to be considered to know the maximum number of holes that can be drilled: the distance between the nozzles must be sufficient to guarantee an adequate heat rejection, avoiding the melting of the pre-chamber material.
The nozzles orientation should be chosen to avoid the impingement of the hot jets against the piston or cylinder walls and at the same time impose to the jets a direction such to travel the longest possible distance inside the combustion chamber. The nozzles length is a parameter of secondary importance, apart from the influence that it has on the pressure drop between main chamber and pre-chamber during the filling process, but considering the small variations of this parameter that could be accommodated by the pre-chamber and engine head geometries, overall the differences are not so relevant [24].

1.2. Effects on engine performances

The two main advantages that the use of a passive pre-chamber provides are: a significant increase of combustion velocity (i.e. reduction of the 10-90% MFB duration) and a considerable reduction of the cyclic variability (i.e. CoV of the IMEP reduction). These two characteristics, demonstrated by several research papers ([3, 6, 8, 14, 21]), give the possibility of modifying the engine design and operating conditions with the aim of increasing the efficiency.
The risk of knock is greatly reduced, thanks to multiple aspects of pre-chamber operation:

the lower combustion duration reduces the time available for the end-gas to auto-ignite; the flame jets travelling distance helps to initiate combustion starting from the mixture close to the cylinder walls, which is the region where end-gas more prone to auto-ignition are generally located; in addition, the enhanced combustion stability almost eliminates the presence of extreme cycles that often lead to knock. In the end, the reduced knock tendency allows to design engines with a higher compression ratio, hence with higher efficiency. Even for already existing engines, the advantage of pre-chamber ignition can be exploited by selecting the spark advance to reach the MBT (Maximum Brake Torque) point for those operating conditions in which before it could not be achieved to avoid the risk of knocking cycles. The superior combustion stability guarantees a more regular engine operation, keeping the cycle-by-cycle pressure peak in a more limited range of CAD (Crank Angle Degrees). This, as already mentioned, reduces the risk of having knocking cycles generated by a pressure peak earlier than the MBT point (i.e. too close to the TDC) and also helps the engine to keep a higher average value of efficiency, which is the lower than the ideal value the more anticipated or delayed is the pressure peak with respect to the MBT point.
Pre-chamber ignition may allow to run the engine with a more diluted mixture in those conditions where with a conventional SI engine the combustion would not be enough stable, thus increasing engine efficiency and reducing emissions (e.g. compared to an operation with richer mixture) [17]. For example, for those engine map regions where an engine was operated with a rich mixture, the use of a TJI combustion strategy helps to obtain a reduction of emissions thanks to the leaner air-fuel ratio, without sacrificing engine performance: the reduction of flame speed caused by the leaner mixture is partially or totally compensated by the faster combustion that a pre-chamber ignition system can provide.
The considerable increase of turbulence inside the main combustion chamber, generated by the ejection of high-velocity jets from the pre-chamber nozzles, gives the opportunity of reducing the intensity of charge motions, thus increasing the volumetric efficiency, which might be an advantage especially for naturally aspirated engines. For this last configuration, and more specifically for PFI (Port Fuel Injection) strategies, the mixture enters into the cylinder already with a sufficiently good homogeneity. Therefore, the charge motions would not be useful for an enhancement of the air-fuel mixing, but just to increase the combustion speed, which is an advantage that can be guaranteed by the use of the TJI.

Possible drawbacks of the use of a combustion pre-chamber are mainly related to heat losses and residual gases remaining inside cylinder and pre-chamber after exhaust valve closing. The increase of heat losses is a topic of non-trivial explanation. Some hypotheses

state that it might be caused by the additional pre-chamber surface and by the fact that the hot jets coming out from the pre-chamber nozzles might be impinging on the piston or cylinder surfaces, therefore transferring an important amount of heat directly to the solid walls. This aspect must be taken into account especially for low engine speeds, where the influence of heat losses on efficiency is more relevant.

The scavenging of the pre-chamber after each combustion phase is more problematic compared to the main chamber, because of the more complicated path that the fresh charge has to follow to replace the burnt gases inside the pre-chamber. Examples of such obstacles are the orifices, which are too narrow for a traditional scavenging, and the geometrical features of the cylinder head. Indeed, the fresh mixture enters in the pre-chamber mainly during the compression stroke, making more tricky for the burnt gases to exit from it, since they tend to be compressed against the top of the pre-chamber volume. Therefore, the amount of residual gases inside the pre-chamber must be carefully evaluated to avoid misfires caused by an excessive amount of inert gases nearby the spark plug electrodes. This issue is of particular importance especially at low loads where, due to the low pressure difference between cylinder and intake duct, also inside the main chamber a higher amount of residual gases remains. Further decrease of pre-chamber efficiency at low loads is caused by the lower intake pressure (due to a more closed throttle valve position), which in turn leads to a lower mass trapped inside cylinder and pre-chamber and finally to weaker jets during combustion.

Another aspect to be evaluated is the risk of pre-ignition from hot spots on the pre-chamber surface. This risk can be avoided by using pre-chambers made of a material with a good heat conductivity and/or designing a cooling circuit which allows to the coolant to flow also around the pre-chamber surface.

2 | Numerical CFD models

Computational fluid dynamics (CFD) is the analysis of systems involving fluid flow, heat transfer and associated phenomena such as chemical reactions by means of computer-based simulation. From the 1960s onwards the aerospace industry has integrated CFD techniques into the design, R&D and manufacture of aircraft and jet engines. More recently the methods have been applied to the design of internal combustion engines and combustion chambers of gas turbines. Furthermore, motor vehicle manufacturers now routinely predict drag forces, under-bonnet air flows and the in-car environment with CFD [28].

The main reason why CFD needed many more years to spread in the industrial community compared to other CAE (Computer Aided Engineering) strategies is the tremendous complexity of the underlying behaviour, which precludes a description of fluid flows that is at the same time economical and sufficiently accurate. The availability of affordable high-performance computing hardware led to an increase of interest since the 1990s.

The growing interest in CFD simulations has been pushed by the potential cost and time saving that can ensure compared to experimental testing. Once the models and setups used for simulations are validated (i.e. produce results that can be trusted), there is the opportunity of performing a much greater number of trials without the need of practically testing several different configurations of a certain equipment, which would be definitely more expensive and also will not anyway allow to easily investigate the fluid flow behaviour inside the tested machine/system. However, some experimental data are often needed to properly setup the initial and boundary conditions for the CFD simulations and, up to now, numerical errors and approximated models do not allow to be completely sure about how predictive are the results obtained from the CFD simulations. In conclusion, at present day, the combined use of experimental and numerical approaches is the best choice to obtain the most trustworthy results, taking advantage of the positive aspects of both these methodologies.

All the information contained in the following sections were taken from different references ([11, 16, 28]) and elaborated in order to highlight the most significant concepts for the purpose of this thesis work.

2.1. Navier-Stokes equations

To completely define the fluid-dynamic and thermodynamic flow behaviour it is necessary to write three equations, which are: the continuity equation (i.e. mass conservation equation), the momentum conservation equation and the energy conservation equation. In the case of a compressible flow these three equations cannot be solved independently because they are linked to each other by means of the pressure-velocity coupling and of the dependency of the density from pressure and temperature of the fluid. The following system of equations illustrates the most general form of the fluid flow governing equations:

$$\begin{cases} \dfrac{\partial \rho}{\partial t} + \boldsymbol{\nabla} \cdot (\rho \boldsymbol{U}) = 0 & \text{(2.1a)} \\ \dfrac{\partial (\rho \boldsymbol{U})}{\partial t} + \boldsymbol{\nabla} \cdot (\rho \boldsymbol{U}\boldsymbol{U}) = \rho \boldsymbol{g} + \boldsymbol{\nabla} \cdot \bar{\bar{\boldsymbol{\sigma}}} & \text{(2.1b)} \\ \dfrac{\partial (\rho E)}{\partial t} + \boldsymbol{\nabla} \cdot (\rho E \boldsymbol{U}) = \rho \boldsymbol{g} \cdot \boldsymbol{U} + \boldsymbol{\nabla} \cdot (\bar{\bar{\boldsymbol{\sigma}}} \cdot \boldsymbol{U}) + \boldsymbol{\nabla} \cdot (\kappa \boldsymbol{\nabla} T) + q_H & \text{(2.1c)} \end{cases}$$

The term $\bar{\bar{\boldsymbol{\sigma}}}$ is the internal stress tensor, its description depends on the properties of the fluid object of the study. The most used model for common fields of application assumes that the fluid is Newtonian, therefore the internal stress tensor is expressed as the sum of the isotropic pressure component and the viscous shear stress tensor, that represents the internal friction force of fluid layers against each other.

$$\bar{\bar{\boldsymbol{\sigma}}} = -p\bar{\bar{\boldsymbol{I}}} + \bar{\bar{\boldsymbol{\tau}}} \tag{2.2}$$

According to Newton's viscous constitutive law, the shear stress tensor $\bar{\bar{\boldsymbol{\tau}}}$ is related to the viscosity of the fluid and to the velocity gradient. In accordance with this assumption, the divergence term of the stress tensor $\bar{\bar{\boldsymbol{\sigma}}}$ in equation (2.1b) becomes:

$$\boldsymbol{\nabla} \cdot \bar{\bar{\boldsymbol{\sigma}}} = -\boldsymbol{\nabla} p + \mu \boldsymbol{\nabla}^{\mathbf{2}} \boldsymbol{U} + \frac{1}{3} \mu \boldsymbol{\nabla} (\boldsymbol{\nabla} \cdot \boldsymbol{U}) \tag{2.3}$$

Combining the governing equations of the fluid flow (2.1) with the assumption of Newtonian fluid expressed in equations (2.2) and (2.3), the Navier-Stokes equations are finally obtained:

$$\begin{cases} \dfrac{\partial \rho}{\partial t} + \boldsymbol{\nabla} \cdot (\rho \boldsymbol{U}) = 0 & \text{(2.4a)} \\ \dfrac{\partial (\rho \boldsymbol{U})}{\partial t} + \boldsymbol{\nabla} \cdot (\rho \boldsymbol{U}\boldsymbol{U}) = \rho \boldsymbol{g} - \boldsymbol{\nabla} p + \mu \boldsymbol{\nabla^2} \boldsymbol{U} + \dfrac{1}{3}\mu \boldsymbol{\nabla}(\boldsymbol{\nabla} \cdot \boldsymbol{U}) & \text{(2.4b)} \\ \dfrac{\partial (\rho E)}{\partial t} + \boldsymbol{\nabla} \cdot (\rho H \boldsymbol{U}) = \rho \boldsymbol{g} \cdot \boldsymbol{U} + \boldsymbol{\nabla} \cdot (\bar{\bar{\boldsymbol{\tau}}} \cdot \boldsymbol{U}) + \kappa \boldsymbol{\nabla^2} T + q_H & \text{(2.4c)} \end{cases}$$

In equation (2.4c) the energy E represents the sum of the internal energy and the kinetic energy of the fluid, but it can also be expressed as function of the enthalpy H, thus allowing to rewrite the energy equation in its enthalpy form, which is often preferred for practical use in CFD codes.

$$E = u + \frac{1}{2}U^2 \qquad , \qquad E = H - \frac{p}{\rho} \tag{2.5}$$

Replacing the second formulation of equation (2.5) inside equation (2.4c), the most widely used version of the energy conservation equation is obtained:

$$\frac{\partial (\rho H)}{\partial t} + \boldsymbol{\nabla} \cdot (\rho H \boldsymbol{U}) = \frac{\partial p}{\partial t} + \rho \boldsymbol{g} \cdot \boldsymbol{U} + \boldsymbol{\nabla} \cdot (\bar{\bar{\boldsymbol{\tau}}} \cdot \boldsymbol{U}) + \kappa \boldsymbol{\nabla^2} T + q_H \tag{2.6}$$

At this point, looking at the final formulation of the Navier-Stokes equations (2.4a), (2.4b) and (2.6), there are still 8 unknowns (i.e. ρ, p, μ, H, T and the three components of the velocity vector U_x, U_y, U_z), but only 5 equations (i.e. mass, energy and momentum in the three directions of the space). Therefore, 3 more equations must be added to obtain a close system of equations and they have to be found by defining a constitutive law of the fluid. For the present thesis work, the missing equations come from the assumption of ideal gas and the correlations of viscosity and specific heat with the temperature, shown by the system of equations (2.7), that will be combined with the set of Navier-Stokes equations (2.4). For the viscosity of an ideal gas the Sutherland's law is commonly used (2.8), while for the specific heat some complex polynomials exist to express its dependency with the gas temperature (2.9).

$$\begin{cases} p = \rho R T & \text{(2.7a)} \\ \mu = \mu(T) & \text{(2.7b)} \\ H = C_p(T) T & \text{(2.7c)} \end{cases}$$

$$\mu = \mu_{ref} \left(\frac{T}{T_{ref}} \right)^{\frac{3}{2}} \frac{T_{ref} + S_\mu}{T + S_\mu} \tag{2.8}$$

$$c_p = aT + bT^2 + cT^3 + O(T^4) \tag{2.9}$$

Due to their mathematical complexity and to the chaotic nature of the turbulent flow behaviour of a fluid generated by the non-linear convective term of equation (2.4b) (i.e. $\boldsymbol{\nabla} \cdot (\rho \boldsymbol{U}\boldsymbol{U})$), an analytical solution for the most general form of the Navier-Stokes equations does not yet exist. For this reason, the Navier-Stokes equations have to be solved numerically. However, the direct numerical solution of a turbulent flow is very cumbersome and would require a huge computational power to solve all the length scales of the various turbulence levels up to the smallest eddies, which would mean using an extremely refined time and space discretization. Even supposing to find the most accurate numerical solution of a turbulent flow, in the end we would obtain a random oscillating trend for the most significant flow variables, from which, for most of the industrial applications, we would extrapolate a mean value of the calculated quantity (e.g. $p, \boldsymbol{U}, ...$) at which it would be added a certain range of variability. For this reason, the equations that are usually solved in practical CFD simulations are the RANS equations, which are an averaged form of the Navier-Stokes equations (2.4) that allow to directly obtain the mean values of the quantities characterising the flow behaviour, just by solving the large scale instabilities of the flow and modelling all the turbulence scales. Even if the solution achieved is of the highest level of approximation, the results are usually precise enough for most of the industrial applications.

2.1.1. RANS: Reynolds Averaged Navier-Stokes

The starting point of the procedure to move from the standard Navier-Stokes equations to the RANS equations is to express each flow quantity as the summation of a mean and a fluctuating component:

$$\Phi = \overline{\Phi} + \Phi' \tag{2.10}$$

The mean component is the integral average of the generic flow quantity Φ over a time window that ideally tends to infinite, while the fluctuating component is the difference

between the actual value and the the mean value of Φ at every instant, needed to account for the turbulent behaviour of the flow.

The second step is to apply the averaging process to the whole equation. The most important property of this procedure is that when the mean is applied on the fluctuating component of a quantity, this will be eliminated (i.e. $\overline{\Phi'} = 0$). However, when the mean is applied to the product of two fluctuating components, the result is different from zero. For instance, in the case of the mass conservation equation (2.4a), the Reynolds averaging procedure will produce the following result:

$$\overline{\frac{\partial \rho}{\partial t} + \boldsymbol{\nabla} \cdot (\rho \overline{\boldsymbol{U}}) + \boldsymbol{\nabla} \cdot (\rho \overline{\boldsymbol{U'}}) = 0} \qquad \Longrightarrow \qquad \frac{\partial \rho}{\partial t} + \boldsymbol{\nabla} \cdot (\rho \overline{\boldsymbol{U}}) = 0 \tag{2.11}$$

For the sake of simplicity, in this explanation the RANS equations will be developed for the case of a flow with constant properties of density, specific heat, viscosity and thermal diffusivity (i.e. not considered as mean + fluctuating component, but just as constant), because in this context the purpose is just to give a general idea about the implications of the averaging process on the Navier-Stokes equations, but being aware that for compressible flows (i.e. with variable density) the Favre averaging procedure is advised to be applied on the Navier-Stokes equations in place of the Reynolds averaging. In the Favre averaging technique the dynamic quantities are subjected to a density weighted average and this procedure introduces additional mathematical complexity, but is generally preferred for compressible flows since it allows to obtain a simpler version of the averaged non-linear convective term of the Navier-Stokes equations, compared to the development that would be obtained by applying the standard Reynolds averaging procedure.
By applying the same procedure seen in equation (2.11) to the whole set of Navier-Stokes equations (2.4), the RANS equations are obtained:

$$\begin{cases} \dfrac{\partial \rho}{\partial t} + \boldsymbol{\nabla} \cdot (\rho \overline{\boldsymbol{U}}) = 0 & \text{(2.12a)} \\ \dfrac{\partial (\rho \overline{\boldsymbol{U}})}{\partial t} + \boldsymbol{\nabla} \cdot (\rho \overline{\boldsymbol{U}}\, \overline{\boldsymbol{U}}) = \rho \boldsymbol{g} - \boldsymbol{\nabla} \overline{p} + \mu \boldsymbol{\nabla^2} \overline{\boldsymbol{U}} + \dfrac{1}{3} \mu \boldsymbol{\nabla} (\boldsymbol{\nabla} \cdot \overline{\boldsymbol{U}}) - \boldsymbol{\nabla} \cdot (\rho \overline{\boldsymbol{U'} \boldsymbol{U'}}) & \text{(2.12b)} \\ \dfrac{\partial (\rho C \overline{T})}{\partial t} + \boldsymbol{\nabla} \cdot (\rho C_p \overline{T}\, \overline{\boldsymbol{U}}) = \rho \boldsymbol{g} \cdot \overline{\boldsymbol{U}} + \boldsymbol{\nabla} \cdot \overline{(\bar{\bar{\boldsymbol{\tau}}} \cdot \boldsymbol{U})} + \kappa \boldsymbol{\nabla^2} \overline{T} + q_H - \boldsymbol{\nabla} \cdot (\rho C_p \overline{T' \boldsymbol{U'}}) & \text{(2.12c)} \end{cases}$$

As it can be seen from equations (2.12b) and (2.12c), the Reynolds averaging procedure causes the presence of a new term in the momentum and energy equations, produced by the averaging of the non-linear convective term.
Focusing on the additional term in the momentum conservation equation (i.e. $\boldsymbol{\nabla} \cdot (\rho\overline{\boldsymbol{U}'\boldsymbol{U}'})$), it is formed by the combination of the fluctuating components of the velocity and it can be seen like a stress added to the viscous molecular one. This term is called Reynolds stress tensor $\bar{\bar{\boldsymbol{r}}}$ and it physically represents the driving force that enhances diffusivity and mixing rates in turbulent flows. Unfortunately, the equations do not provide any direct expression for the Reynolds stresses and the same can be said also for the additional term in the energy equation (that can be seen like a turbulent heat flux), therefore these two terms have to be modelled to find a solution of the problem.

All what has been previously said leads to the conclusion that the RANS equations cannot be solved by themselves, but they have to be coupled with a turbulence model. Several turbulence models exist, but the foundation of most of them are based on the Boussinesq's hypothesis, which, in short, states that the terms previously discussed resulting from the averaging procedure are considered as an additional viscosity for the momentum equation and an additional thermal diffusivity for the energy equation. The non-linear fluctuating terms in equations (2.12b) and (2.12c) are replaced by the turbulent viscosity and the turbulent diffusivity, thus the viscosity of the fluid is now formed by two contributions $(\mu + \mu_T)$ and the same happens for the thermal diffusivity $(\kappa + \kappa_T)$. The terms added to the molecular properties of the fluid have the purpose of modelling the effect of turbulence, which induces enhanced mixing rates.
After including the Boussinesq's hypothesis in the momentum equation (2.12b) and applying some simplifications to the energy equation (2.12c), the final version of the set of RANS equations looks like the following:

$$\begin{cases} \dfrac{\partial \rho}{\partial t} + \boldsymbol{\nabla} \cdot (\rho\overline{\boldsymbol{U}}) = 0 & \text{(2.13a)} \\ \dfrac{\partial (\rho\overline{\boldsymbol{U}})}{\partial t} + \boldsymbol{\nabla} \cdot (\rho\overline{\boldsymbol{U}}\,\overline{\boldsymbol{U}}) = \rho\boldsymbol{g} - \boldsymbol{\nabla}\overline{p} + (\mu + \mu_T)\boldsymbol{\nabla^2}\overline{\boldsymbol{U}} & \text{(2.13b)} \\ \dfrac{\partial (\rho C\overline{T})}{\partial t} + \boldsymbol{\nabla} \cdot (\rho C\overline{T}\,\overline{\boldsymbol{U}}) = \rho\boldsymbol{g} \cdot \overline{\boldsymbol{U}} + (\kappa + \kappa_T)\boldsymbol{\nabla^2}\overline{T} + q_H & \text{(2.13c)} \end{cases}$$

The turbulent thermal diffusivity generally comes from an assumption on the turbulent Prandtl number, which correlates it with the turbulent viscosity:

$$Pr_T = c_p \frac{\mu_T}{\kappa_T} \qquad \Longrightarrow \qquad \kappa_T = c_p \frac{\mu_T}{Pr_T} \tag{2.14}$$

Eventually, it all comes to the modelling of the turbulent viscosity.
One of the most widely used turbulence models is the $k-\varepsilon$. In this model, the turbulent viscosity is expressed as a function of the turbulent kinetic energy (k) and the turbulent dissipation rate (ε), which in turn are derived from the concepts of turbulent length (l_T) and velocity scale (u_T):

$$\begin{cases} \mu_T \propto \rho \cdot u_T \cdot l_T \\ u_T \propto \sqrt{k} \\ l_T \propto \sqrt{k} \cdot \dfrac{k}{\varepsilon} \end{cases} \qquad \Longrightarrow \qquad \mu_T = C_\mu \rho \frac{k^2}{\varepsilon} \tag{2.15}$$

Replacing equations (2.14) and (2.15) inside the RANS equations (2.13) there will be two new unknowns, therefore the RANS equations must be coupled with two additional equations of the turbulence model, one for k and one for ε, to obtain a close system. The turbulent kinetic energy is defined as $k = \frac{1}{2}(\overline{U_x'^2} + \overline{U_y'^2} + \overline{U_z'^2})$ and an equation for it can be obtained rearranging the RANS momentum conservation equation (2.12b) through several mathematical steps, while the equation for the turbulent dissipation rate is completely modelled.

$$\begin{cases} \rho \dfrac{\partial k}{\partial t} + \rho \overline{\boldsymbol{U}} \cdot \boldsymbol{\nabla} k = \bar{\bar{\boldsymbol{r}}} : \boldsymbol{\nabla} \overline{\boldsymbol{U}} + \boldsymbol{\nabla} \cdot ((\mu + \dfrac{\mu_T}{\sigma_k}) \boldsymbol{\nabla} k) - \rho \varepsilon & \text{(2.16a)} \\ \rho \dfrac{\partial \varepsilon}{\partial t} + \rho \overline{\boldsymbol{U}} \cdot \boldsymbol{\nabla} \varepsilon = C_{\varepsilon_1} \dfrac{\varepsilon}{k} \bar{\bar{\boldsymbol{r}}} : \boldsymbol{\nabla} \overline{\boldsymbol{U}} + \boldsymbol{\nabla} \cdot ((\mu + \dfrac{\mu_T}{\sigma_\varepsilon}) \boldsymbol{\nabla} \varepsilon) + C_{\varepsilon_2} \rho \dfrac{\varepsilon^2}{k} & \text{(2.16b)} \end{cases}$$

The values of the coefficients in equations (2.15), (2.16a) and (2.16b) are:

$$C_\mu = 0.09; \quad \sigma_k = 1; \quad \sigma_\varepsilon = 1.3; \quad C_{\varepsilon_1} = 1.44; \quad C_{\varepsilon_2} = 1.92 \tag{2.17}$$

Conservation of mass fractions for gas mixtures

The Navier-Stokes equations as seen up to now are valid for a flow composed of just one molecule. However, the present thesis work deals with flows composed by more gases, since inside an internal combustion engine there is always a mixture of different chemical species. For instance, the fresh mixture is composed by oxygen, nitrogen and fuel, which are mixed also with the residual gas during the gas exchange process.
Therefore, one more equation for each of the chemical species considered must be added to the standard set of RANS equations to enforce the conservation of each mass fraction. The total mass conservation equation (2.13a) is always valid and the mass conservation equation for each generic species k composing the gas mixture is introduced [19]:

$$\frac{\partial \rho Y_k}{\partial t} + \boldsymbol{\nabla} \cdot (\rho(\boldsymbol{U} + \boldsymbol{V}_k)Y_k) = \dot{\omega}_k \tag{2.18}$$

$\boldsymbol{V}_k$ is the diffusion velocity of species k and $\dot{\omega}_k$ is the reaction rate for species k.

In the end, the system of equations resulting from the composition of the set of RANS equations (2.13), the turbulence model equations (2.16) and the mass fractions conservation equations (2.18) can finally be solved by a CFD code implementing a proper discretization procedure.

2.2. Numerical discretization

A computer is not capable of dealing with continuous mathematical functions like derivatives and integrals which are fundamental to write the equations that describe or model the physical phenomena like in the case of the RANS equations for fluid flow modeling, but it can only handle a discretized version of these mathematical functions. For this reason, the various terms composing the analytical mathematical equations must be converted into their discretized counterparts, resulting in an approximated version of the original equation that is now solvable in a finite number of operations, but will give as output a solution affected by a discretization error which will be the bigger the less accurate are the discretization schemes used for the conversion of the continuous problem into an approximated discrete problem.
Most of the CFD codes use the finite volume method that discretizes the fluid domain into a number of small volumes (i.e. cells), therefore it is more appropriate to write the fluid flow equations in their integral form (in section 2.1 the differential form was presented), since the physical quantities describing the fluid-dynamic behaviour are cal-

culated through an integration over the volume of each cell. As a consequence, the most important step to move from the theoretical equations to the algebraic ones that can be solved by the calculator is to define how to discretize the surface and volume integrals that are composing the equations describing the flow motion in every cell.
The value of the different quantities describing the flow is calculated in just one point for each cell, which is the centroid of the cell (defined in a similar way as the center of mass). Starting from the only point in which the calculated quantity is known, a linear variation of the quantity inside the cell is assumed, and the same assumption is done for the variation of the quantity on each of the cell's faces, starting from the centroid of the face.
When it comes to the discretization of a volume integral, the value of the generic quantity Φ (e.g. $\Phi = \rho$ in the case of mass conservation equation; $\Phi = \rho \boldsymbol{U}$ for the momentum conservation equation; etc...) is expressed as the value of the quantity in the center of the considered volume Φ_P, that is known, to which it is added the linear variation of that quantity within the volume, as an hypothesis. However, when it comes to the need of discretizing a surface integral, the same assumption of linear variation along the surface is done, but in this case the value of Φ in the centroid of the face (Φ_f) is not known, thus a relationship between Φ_f and the value of the considered quantity in the only points of the mesh in which it is known (i.e. the centroids of the cells that share this face) has to be imposed.
Based on the chosen scheme to correlate the value of Φ_f with the value of Φ of the closest cell centers, the accuracy and stability of the numerical method used to solve the equations are established.

2.2.1. Integrals discretization schemes

As a simplified example, we can consider the basic conservation equation of a generic quantity Φ composed by the most common terms that can be found in the different fluid flow equations, which are: the time derivative term representing the variation of Φ in the control volume, the surface integrals representing the convective and the diffusive flux, and the volume and surface integrals representing a generic volume or surface source term.

$$\frac{\partial}{\partial t}\oint_V \Phi \, dV = -\oint_S \Phi \boldsymbol{U} \cdot \boldsymbol{n} \, dS + \oint_S \kappa \boldsymbol{\nabla} \Phi \cdot \boldsymbol{n} \, dS + \oint_V q_V \, dV + \oint_S \boldsymbol{q}_S \cdot \boldsymbol{n} \, dS \tag{2.19}$$

The approximation of a generic volume integral is usually performed by resorting to the midpoint rule, which consists in the replacement of the generic value of the quantity Φ inside the control volume with the value of Φ in the centroid of the cell (Φ_P) to which it

is added a linear variation of Φ in the control volume:

$$\oint_V \Phi \, dV = \oint_V \Phi_P \, dV + \oint_V (\boldsymbol{x} - \boldsymbol{x_P}) \cdot (\boldsymbol{\nabla}\Phi)_P \, dV + O(\Delta x^2) \tag{2.20}$$

The centroid of each cell is defined in the following way (i.e. as the center of mass):

$$\oint_V (\boldsymbol{x} - \boldsymbol{x_P}) \, dV = 0 \tag{2.21}$$

Therefore, replacing equation (2.21) inside equation (2.20), it can be seen that the discretized version of the volume integral achieves a second order accuracy (i.e. the first term of the truncation error is of second order) and finally equation (2.20) becomes the following:

$$\oint_V \Phi \, dV = \Phi_P V + O(\Delta x^2) \tag{2.22}$$

The approximation of a generic surface integral is performed with the same rule just seen for the volume integral, thus resulting in the same final expression:

$$\oint_S \Phi \, dS = \Phi_f S + O(\Delta x^2) \tag{2.23}$$

With respect to the volume integral discretization, the difference is that the value of Φ_P was known because it is the point where the quantity Φ is computed, whereas in this case the value of the quantity in the face center (Φ_f) is not known, so it has to be computed by interpolation.

For example, if we consider the case of the convective term of equation (2.19), its discretized form will be the following:

$$\oint_S \Phi \boldsymbol{U} \cdot \boldsymbol{n} \, dS = \sum_f (\Phi \boldsymbol{U})_f \cdot \boldsymbol{S} = \sum_f \Phi_f U_n S \tag{2.24}$$

Eventually, it all comes to the choice of the approach to determine the value of Φ_f. As it was pointed out from equation (2.22), the accuracy of the volume integral discretization is of second order, but the final accuracy of the whole discretization process of the conservation equation will depend on the accuracy of the schemes chosen for the determination of Φ_f for all the surface integral terms of equation (2.19), which should be of second order

too to preserve a global second order accuracy. Unfortunately, for reasons of numerical stability of the problem solution procedure, it is not always possible to achieve the best accuracy.

Approximation of the face center value

The most common first order accuracy approach used for approximating Φ_f is known as "upwind" scheme: the value of Φ in the face center is assigned as equal to the value of Φ in the centroid of one of the two cells (called P and N) that own the face, on the basis of the flow direction. More precisely, it is assigned to Φ_f the value of the upstream cell with respect to the considered cell face.

$$\begin{cases} \Phi_f = \Phi_P \qquad if \quad \boldsymbol{U} \cdot \boldsymbol{n} > 0, & \text{(2.25a)} \\ \Phi_f = \Phi_N \qquad if \quad \boldsymbol{U} \cdot \boldsymbol{n} < 0 & \text{(2.25b)} \end{cases}$$

From this definition, expanding the Taylor series about P in equation (2.24) follows:

$$\sum_f \Phi_f U_n S = \sum_f U_n S \Phi_P + \sum_f U_n S(\boldsymbol{x_f} - \boldsymbol{x_P}) \cdot (\boldsymbol{\nabla}\Phi)_P + O(\Delta x^2) \tag{2.26}$$

From the numerical point of view the upwind scheme is inherently stable (i.e. the solution will be always bounded), but because of its first order accuracy, the global accuracy of the numerical problem will be lower than second order. As it can be noticed from equation (2.26), using a first order accuracy scheme means that there is a truncation error proportional to the gradient of Φ, therefore adding a numerical diffusivity with a coefficient proportional to the mesh spacing. As a consequence, the use of this scheme introduces an artificial viscosity which alters the flow behaviour by smearing sharp variations, with an error that is the bigger the coarser is the mesh.
For this reason, it would be convenient to use a second order accuracy scheme also for the determination of Φ_f, such as the linear scheme. This scheme calculates the value of Φ_f by means of a linear interpolation between the nearest cell centers:

$$\Phi_f = \zeta \Phi_N + (1 - \zeta)\Phi_P \qquad with \quad \zeta = \frac{x_f - x_P}{x_N - x_P} \tag{2.27}$$

By expanding the Taylor series of Φ_f around the centroid of the cell P, it can be seen that the linear approach leads to a second order accurate method, with the leading term of the truncation error proportional to the square of the grid spacing, thus making the

discretization error tending to zero faster than the upwind scheme. This also allows to avoid the introduction of the numerical diffusivity, but the problem is that this method often produces oscillatory solutions, therefore it is highly unstable.
Another scheme that is worth to mention is the linear upwind differencing scheme, which involves two cell center upstream values with respect to the face center value that needs to be calculated. This scheme is sometimes used to try to combine the advantages of both the upwind and the linear schemes, allowing to obtain a better accuracy than the upwind scheme with an improved stability compared to the linear scheme.
Several other methods exist that give the possibility of using a second order scheme, but avoiding the presence of instabilities. These techniques are called flux limiters and their goal is to achieve an accuracy higher than a first order scheme, but also being sufficiently stable: this target is achieved by limiting the value of the flow property in those regions where a too sharp gradient of that parameter is detected, using an upwind discretization scheme locally, only where it is strictly necessary to guarantee the stability of the whole process. In all the other regions the accuracy will be of second order. These methods are all gathered under the name of TVD (Total Variation Diminishing).
Also higher order schemes exist for the approximation of the surface and volume integrals and for the interpolation of the face center value, but since they do not always guarantee a significant accuracy improvement compared to the higher complexity and higher computational cost introduced, they are rarely used.

2.2.2. Linear equation

The Navier-Stokes equations (seen in their partial derivatives formulation in the system of equations (2.4)), and consequently the RANS equations, are a very complex set of equations composed by convective terms, diffusive terms, gradient terms and time-dependent terms. After the discretization of all these terms, a system of algebraic equations is obtained for each of the RANS equations, forming a very big matrix in which every line refers to one cell of the mesh and contains some terms correlating it to its neighbouring cells. The matrix will be of rank n×n, where n is the number of cells forming the entire mesh. Every line of the matrix has the following form:

$$a_P \Phi_P + \sum_N a_N \Phi_N = Q \tag{2.28}$$

The index N is indicating a generic neighbouring cell (e.g. in the case of an hexahedral mesh there will be six neighbouring cells). The coefficient a_P is on the matrix diagonal,

whereas the coefficients related to the neighbouring cells will be off-diagonal terms of the matrix. The vector of known terms $\boldsymbol{Q}$ can be formed by source terms and terms coming from previous time steps that are used in the discretization of the time derivatives.
Finally, the typical matrix problem to be solved has the following formulation:

$$[A]\boldsymbol{\Phi} = \boldsymbol{Q} \tag{2.29}$$

In equation (2.29) the vector $\boldsymbol{\Phi}$ is composed by the generic quantity Φ in the centroid of every cell of the mesh, which in the case of a fluid flow problem is: ρ for the continuity equation, $\rho\boldsymbol{U}$ for the momentum equation and ρE for the energy equation.
A more detailed explanation of the process to move from a partial differential equation to the final system of algebraic equations can be read in Appendix A, where a practical example is presented to clarify this topic.

There are two possible approaches for solving a system of linear equations: direct methods or iterative methods.
The use of a direct method would allow to obtain the exact solution of the matrix problem, but at the expense of a very high computational cost, usually unsustainable for industrial purposes. For this reason, iterative methods are generally used, which allow to obtain an approximated solution through a series of operations starting from a first guess value. The iterative process comes to an end when the value of the residual becomes lower than a certain tolerance fixed by the user; at that point, convergence is considered to be achieved. The computational effort needed by the iterative solver will be the lower the closer is the first guess value compared to the exact solution of the problem and the bigger is the chosen tolerance (at the expense of the accuracy).

In conclusion, the reliability of the final results of a CFD simulation is influenced by the accuracy of the chosen discretization schemes for the various terms present in the equations describing the fluid flow (e.g. convective terms, diffusive terms, gradient terms, ...) discussed in section 2.2.1 and by the iterative method chosen for solving the systems of algebraic equations for every cell of the mesh, but it is also strongly influenced by the quality and the level of refinement of the calculation grid. If the mesh is not flow oriented, all the faces of a cell have a normal component of the velocity, therefore the diffusion of the error is present also in the direction orthogonal with respect to the flow, as it can be deduced from equation (2.24) (while in the case of flow oriented mesh, the diffusion of the error is only on two faces of a cell). Moreover, if some cells of the mesh are characterised by a certain skewness, the truncation error of the convective terms like the one analyzed

in equation (2.24) is proportional not only to the mesh spacing, but also to the skewness index, while if some cells of the mesh are characterised by a certain non-orthogonality, the truncation error resulting from the discretization of the diffusive terms is affected. Consequently, all the previously mentioned aspects must be carefully taken into account when generating the mesh of the fluid domain that has to be simulated.

2.3. Combustion modelling

The combustion modelling approach used in the present thesis work was the flame area evolution (FAE) model from Weller that predicts the reaction rate evolution. Transport equations are solved for mass, momentum, energy, turbulence and mixture fraction. Instead, the chemical composition, laminar flame speed and thickness are extracted from dedicated lookup tables depending on the local thermodynamic condition and mixture properties.
This combustion model was chosen because it has already showed its validity in some recent research papers ([22, 23]), dealing with engine operative conditions and characteristics presenting some similarities with the ones addressed by this thesis work.

The combustion model from Weller is based on the laminar flamelet concept and it describes the flame propagation process in the CFD domain by means of two quantities:

1. The unburned gas fraction b, also called regress variable.
2. The flame wrinkle factor Ξ, which is the ratio between turbulent (S_t) and laminar (S_u) flame speeds.

The first quantity allows to model the flame front propagation through a dedicated transport equation, which can be written as:

$$\frac{\partial \rho \tilde{b}}{\partial t} + \boldsymbol{\nabla} \cdot (\rho \tilde{\boldsymbol{U}} \tilde{b}) + \boldsymbol{\nabla} \cdot (\mu_T \nabla \tilde{b}) = \rho_u \tilde{S}_{\tilde{u}} \tilde{\Xi} |\nabla \tilde{b}| + \dot{\omega}_{ign} \tag{2.30}$$

The term $\rho_u \tilde{S}_{\tilde{u}} \tilde{\Xi} |\nabla \tilde{b}|$ models the reaction rate as function of the local mixture properties and the flame-turbulence interaction. This last effect is predicted by the flame wrinkle factor Ξ.
The ignition process is included through the source term $\dot{\omega}_{ign}$, that is described by a simplified deposition model, in which the initial flame kernel diameter d_k and ignition duration Δt_{ign} are user-specified parameters. Inside the computational cells whose distance from the specified ignition location is less than d_k the ignition source term is imposed

according to:

$$\dot{\omega}_{ign} = \frac{C_s \rho_u b}{\Delta t_{ign}} \tag{2.31}$$

where ρ_u is the unburned gas density while C_s is a user-defined parameter calibrating the amount of energy released by the spark-plug (i.e. ignition strength).
The result is the initialization of a flame brush (i.e. b distribution) around the ignition zone, which is ready for the premixed flame propagation. However, the early flame kernel is laminar and there is a transition process before the achievement of a fully corrugated turbulent flame, which has to be modelled. In this work, this aspect is embedded into the flame wrinkle factor Ξ modelling.
To model the laminar-to-turbulent transition process occurring after the spark-ignition event, the Ξ value is evolved from 1 (laminar flame) to Ξ^*_{eq} (fully turbulent flame) with the expression:

$$\Xi = f \cdot \Xi^*_{eq} \tag{2.32}$$

where the parameter f is computed according to the Herweg-Maly correlation:

$$f = \left[1 - exp\left(-\frac{r_k}{l_T}\right)\right]^{1/2} \cdot \left[1 - exp\left(-\frac{U' + S_u}{l_T} \cdot t_{ign}\right)\right]^{1/2} \tag{2.33}$$

and Ξ^*_{eq} is modelled according to Peters:

$$\Xi^*_{eq} = 1 - \frac{a_4 b_3^2 l_T}{2 b_1 \delta_l} + \left[\left(\frac{a_4 b_3^2 l_T}{2 b_1 \delta_l}\right)^2 + a_4 b_3^2 \frac{U' l_T}{S_u \delta_l}\right]^{1/2} \tag{2.34}$$

The unstrained laminar flame speed in equation (2.30) is estimated according to:

$$S_u = S_{u,ref}(\phi) \cdot \left(\frac{T}{T_{ref}}\right)^{\alpha} \cdot \left(\frac{p}{p_{ref}}\right)^{\beta} \tag{2.35}$$

where $S_{u,ref}$ depends on the equivalence ratio ϕ and is computed according to the Gulder correlation:

$$S_{u,ref} = W \cdot \phi^{\eta} \cdot e^{-\xi(\phi - 1.075)^2} \tag{2.36}$$

The chemical composition in any computational cell is computed from the mass fraction of chemical species in the burned Y_b and unburned state Y_u, and from the regress variable b:

$$Y_k = bY_{u,k} + (1 - b)Y_{b,k} \tag{2.37}$$

2.4. OpenFOAM

The CFD code used for this thesis work is OpenFOAM (Open Field Operation And Manipulation), which is an open-source software that uses the finite volume method for domain discretization and performs an integration of the governing equations of fluid flow over all the control volumes (cells) of the solution domain (mesh). The integral form of the fluid flow equations is converted to a discretized form according to different possible schemes that can be selected by the user independently for the various terms of the equations and finally the resulting system of algebraic equations is solved by means of an iterative method selected by the user among different choices.

OpenFOAM is a framework for developing application executables that use packaged functionality contained within a collection of approximately 100 C++ libraries. OpenFOAM is shipped with approximately 250 pre-built applications that fall into two categories: solvers, that are each designed to solve a specific problem in fluid (or continuum) mechanics; and utilities, that are designed to perform tasks that involve data manipulation. The solvers in OpenFOAM cover a wide range of problems in fluid dynamics. Users can extend the collection of solvers, utilities and libraries in OpenFOAM, using some pre-requisite knowledge of the underlying method, physics and programming techniques involved. OpenFOAM is supplied with pre- and post-processing environments. The interface to the pre- and post-processing are themselves OpenFOAM utilities, thereby ensuring consistent data handling across all environments [12].

The possibility of modifying the software structure and creating new utilities and solvers has been exploited in the last years by the researchers of the internal combustion engines group at Politecnico di Milano. Their work gave birth to a new library called LibICE, that, in conjunction with version 8 of OpenFOAM, allows to generate the mesh and simulate the fluid flows in internal combustion engines through the help of semi-automatic procedures and pre-defined setups that lead to a considerable time saving compared to all the operations that would be necessary to perform manually if using the standard

OpenFOAM version.
For example, a utility was created to test the mesh features and refinements for the various phases of the engine cycle in a quick way, by specifying which crank angle position wants to be tested. Moreover, once the desired meshing setup is defined, another utility gives to the user the possibility of generating all the moving meshes needed for a full cycle simulation (i.e. 720° in the case of a 4-stroke engine). A routine of operations automatically recognizes the STL files that are common for every internal combustion engine and consequently modifies the global 3D geometry according to the specified crank angle by following the imposed motion law. The mesh is generated and deformed to simulate the engine movement until the minimum mesh quality parameters are satisfied. The procedure is then repeated several times for each crank angle from which the previous mesh was not anymore valid, until the full cycle duration is covered.
Several other utilities are available inside the LibICE for cold-flow and combustion simulation of both SI and CI engines, lagrangian spray modelling and after treatment systems modelling.

The potential of this library was exploited at its best for the purpose of this thesis work, with the application of some modifications to the original code to be able to handle the presence of a pre-chamber on the simulated engine, allowing to obtain reliable and detailed results in a reasonable time. This was made possible thanks to the flexibility of the LibICE code, proving itself to be an ideal tool for research purposes.

3 | The selected pre-chamber engine

3.1. Engine data and operative conditions

The engine subjected to the experimental test campaign carried out by Marmotors s.r.l. was an in-line 2-cylinder, 4-stroke, naturally aspirated, 660 cc motorcycle engine. It is characterised by a PFI (Port Fuel Injection) system, a pent-roof combustion chamber with four valves per cylinder and a compression ratio of approximately 13.5.

Figure 3.1: Original engine

The engine is over-squared, as is typical for high revving motorcycle engines, with a bore of 81 mm and a stroke of 63.8 mm (bore-to-stroke ratio of 1.27). Another peculiar characteristic of this engine is that the center-line of the crankshaft is shifted with respect to the cylinder axis, causing an offset between the crankshaft itself and the piston pin. The adoption of this solution, the so-called pin offset, is generally implemented with the aim of reducing the transversal force applied by the piston on the cylinder wall during the expansion stroke, thus helping to reduce friction and wear. The presence of a pin offset means that the TDC (Top Dead Center) is not reached when the crank is in the vertical position, but when crank and rod are aligned, condition that usually happens few CAD after the crank vertical position.

The spark plug seat on the engine cylinder head was slightly modified to host a pre-chamber to be easily mounted on the original engine. The pre-chamber includes the spark plug, that is located at a greater height over the cylinder head compared to the standard engine. Several different kinds of pre-chamber were tested, varying its geometrical parameters, such as volume, nozzles diameters and length in order to find the best solution for the whole engine map. The pre-chamber finally chosen is characterised by six orifices and it was considered as the optimal solution among the others since it showed the best engine performance thanks to the lowest amount of residual gases remaining inside it and the highest level of turbulent kinetic energy close to the spark plug before the start of combustion.

The engine head and pre-chamber were adapted to house the channels for a cooling circuit, needed to reduce the pre-chamber temperature. The possibility of varying the cooling fluid mass flow rate was also implemented. This feature is of great importance, since it allows to control the pre-chamber wall temperature, avoiding the presence of pre-ignition cycles caused by an excessively high temperature in some points of the pre-chamber surface.

The tests were performed at 3500 rpm, 5000 rpm, 9000 rpm and 10500 rpm, with different loads for each engine speed, considering the most likely values of throttle valve opening depending on the rpm (i.e. typically low valve openings for low engine speed, medium and high valve openings for higher engine speeds). For all the operating points tested, a sweep of several λ (i.e. equivalent air-to-fuel mass ratio) values was done to investigate the performance of the engine with a leaner mixture.

The results of the engine tested with the passive pre-chamber were finally compared to the results obtained from the tests of the same engine equipped with a dummy pre-chamber, which had the purpose of positioning the spark plug at the same height as for the original engine, without adding more volume to the main chamber and obtaining the same combustion development of the standard spark ignition engine.

3.1.1. Data from test bench and 1D simulation

The engine was prepared on the test bench with the addition of an in-cylinder pressure sensor and of a spark plug with an integrated pressure sensor on both cylinders. This setup allows to acquire a pressure signal from both the main chamber and the pre-chamber. For the purpose of obtaining a suitable pressure curve to be used as reference for the following simulations, the acquired signal was post-processed by averaging it on 300 engine cycles and by applying a filtering method to eliminate as much a possible the effects of noise and vibrations on the signal acquisition quality.
Despite all the efforts put to obtain the most reliable reference pressure curves, it has to be taken into account that measurement errors and other uncertainties cannot be completely deleted. For instance, the measure performed by the pressure sensor is affected by an intrinsic error and the engine geometrical characteristics are subjected to certain tolerances which may cause a variation not known a priori from the reference values. For example, the determination of the Top Dead Center (TDC) is of fundamental importance to obtain a correct matching between the CAD (which detection is subjected to a measurement error too) and the corresponding pressure value. Indeed, in engines like this one characterised by a certain value of pin offset, the TDC does not correspond to the vertical crank position. The shift between 0 CAD (considered as position of vertical crank) and the CAD corresponding to the effective TDC in this case was determined by resorting to the concept of loss angle, thus from a thermodynamic perspective instead of from a geometrical perspective. In conclusion, the determination of the exact position of the TDC may hide some errors coming from the tolerance on the pin offset and loss angle values given by the manufacturer, which might not be exactly the same for every engine coming out from the factory, due to production and assembly tolerances.
Moreover, the value of compression ratio denoted by the manufacturer was of 13.5 ± 0.5, where the variability is caused by the just mentioned production and assembly tolerances. For this reason, the exact compression ratio of the tested engine is unknown.

The availability of an in-cylinder pressure signal is extremely useful for comparing it with the results obtained from the following simulations and for tuning the simulation setup in order to obtain an in-cylinder pressure trace coherent with the one resulting from the experiments, but always keeping in mind the uncertainties inevitably affecting the experimental data and the probable differences between the real engine tested and the 3D model used for the simulation. For instance, the geometry of the STL file of the engine was tuned to have a compression ratio of 13.5, whereas the precise compression ratio of the tested engine is not known.

However, the availability of this signal is not enough for setting up a 3D CFD simulation, because also pressure and temperature data inside the intake and exhaust ducts are required for imposing the boundary conditions necessary for the simulation. In this case, sensors for measuring pressure and temperature inside the ducts were not available, so all these data are obtained from 1D simulations. In this kind of simulation the boundary conditions are tuned in order to obtain a pressure curve as much as possible similar to the pressure curve measured experimentally, needing much less computational time compared to a 3D simulation. Finally, the temperature and pressure curves resulting from the 1D simulation will be used as boundary conditions for the intake and exhaust ducts of the 3D simulation, being aware that even these data are subjected to uncertainties due to the nature of the 1D simulations that cannot precisely reproduce the flow behaviour, which obviously is three-dimensional.

3.2. Target of pre-chamber application

For current motorcycle engines it is becoming more and more difficult to comply with the most recent emissions regulations, especially looking forward to the forthcoming EURO 5+ standards (expected for 2024) and to the future EURO 6 regulations, specifically referred to motorcycles, which will impose a further decrease of pollutant emissions. In particular, it is quite challenging to keep similar performance and at the same time reduce engine emissions for such high-performance naturally aspirated engines.
It is usual for motorcycle engines to run with a rich air-fuel mixture for the most part of the engine map (like in the case of the engine subject of this research), primarily for two reasons: to maintain a fast combustion that is required especially at high engine speeds (that for a motorcycle engine are much higher compared to the maximum engine speed of common passenger cars) and to keep a stable combustion in the wide range of speeds and loads typical of motorcycle engines. Furthermore, it is ordinary for these engines to delay the spark triggering with respect to the ideal timing in some critical areas of the engine map to avoid the presence of knock.

The role of Turbulent Jet Ignition might become determinant for producing more efficient engines, capable of reducing emissions of the required amount. The major benefits that the pre-chamber ignition technology can provide to this kind of engines are the possibility of reducing combustion duration and appreciably improving combustion stability. These characteristics might allow to increase the spark advance where it is needed (i.e. where the engine was not running at the MBT condition because of a poor combustion stability), thus improving engine performance thanks to a higher pressure peak. Moreover,

thanks to the pre-chamber, the engine can be operated with leaner air-fuel ratios without penalizing the combustion speed. As a consequence, good performance are guaranteed, avoiding knocking cycles and reducing CO, HC and soot emissions (thanks to stoichiometric combustion instead of rich). Clearly, even for those operative conditions where the engine is already working at the MBT point, the spark triggering timing must be delayed to keep the engine running in this optimal condition for performance and efficiency, given the faster combustion velocity that the TJI system guarantees.
The above-mentioned advantages could be gained applying a properly designed pre-chamber on an already existing engine, without any substantial modification. Nevertheless, the full potential of TJI would probably be exploited only by designing a new engine, taking advantage of the pre-chamber strong points and thus, for instance, increasing the compression ratio and reducing the intensity of charge motions.

The innovation and the uncertainties of the research activity developed by Marmotors s.r.l. regarded the application of a passive pre-chamber on a naturally aspirated engine. In fact, a very limited database is available for such system in literature, especially for engines with a wide operative map like in the case of this motorcycle engine. Most of the doubts concerned the quality of the pre-chamber scavenging process and the consequent risk of misfires in case an excessive amount of residual gases remains around the spark plug electrodes in the pre-chamber. This is due by a lower pressure difference between main chamber and pre-chamber caused by the globally lower pressures involved in a naturally aspirated engine compared to a turbocharged configuration.

3.2.1. Experimental findings

The experimental results demonstrated the potential of the application of a passive pre-chamber on a high-revving naturally aspirated engine. The first important success obtained was the possibility of running the engine with a pre-chamber for all the various conditions of speed and load, without detecting problems related to misfires or knocking cycles. Then, from the performance point of view, the results are not uniform for all the operative conditions tested. Comparing the results of the engine equipped with the pre-chamber to the data obtained from the original SI engine, the general trend shows an important reduction of the combustion duration and of the cycle-to-cycle variability, as demonstrated also by other research papers ([3, 8, 10, 26]) on engines with different characteristics compared to the one discussed in the present work. The combination of these two advantages allowed to run the engine efficiently also with a stoichiometric air-fuel ratio, which was not possible for the original engine without facing a significant perfor-

mance loss (and hence efficiency loss) that would have been needed to avoid knocking cycles caused by an excessive operating instability. The possibility of running with a stoichiometric mixture leads to a reduction of CO, HC and soot emissions at the tailpipe, thanks to the lower amount of these pollutant species at the exhaust valve after each combustion and also to the higher working efficiency of the three-way catalyst.
Having seen the improvement of combustion that the use of the TJI system guarantees, it was expected to obtain benefits also in terms of mean effective pressure. However, comparing original and pre-chamber-equipped engines for the same operative conditions, no advantage in terms of IMEP (Indicated Mean Effective Pressure) were noticed, but, on the contrary, a small reduction of the IMEP value is often present for the pre-chamber engine. A straightforward explanation for this aspect has not been found yet and this is one of the reasons why the possibility of performing reliable CFD simulations might allow to better understand the physical phenomena that cause this loss of performance, despite the higher combustion efficiency. The main hypothesis is related to an increase of heat losses, but which is the main contribution still has to be established. One cause may be the additional surface of the pre-chamber that is added to the cylinder head surface (i.e. higher surface-to-volume ratio). Another reason may be related to the likelihood that the hot jets coming out from the pre-chamber orifices are impinging on the combustion chamber walls, thus wasting a remarkable amount of heat.

One of the objectives of the 3D CFD simulations is to help to clarify this issue. At that point, it is supposed to be less difficult to think about a solution for the purpose of exploiting as much as possible the advantages that the pre-chamber ignition can provide and to define a clearer relationship between the pre-chamber features and the expected engine performance.

4 | Simulation setup

4.1. Mesh generation

The initial and one of the most important and time-consuming steps of the simulation setup is the mesh generation.
A good quality mesh is of fundamental importance to obtain accurate and reliable results from the simulations, since it has a significant impact on the outcomes of the discretization procedure of the surface integrals.
One of the goals that should be tried to achieve when meshing the fluid domain is to produce a flow-oriented mesh. This is important because when the surface integrals of the convective terms are approximated, for each face a truncation error is present and is proportional to the normal component of the velocity (as it can be seen from equation (2.26)). As a consequence, if the cells are not flow-oriented, each cell face has a normal component of the velocity, thus on all the directions normal to each cell face there will be a numerical error (i.e. even in directions orthogonal with respect to the real flow direction). On the contrary, if the cell is perfectly flow-oriented, a normal component of the velocity is present only for the two faces with a normal parallel to the flow direction, thus limiting the generation of a numerical error only along the flow direction. Moreover, the diffusion of the error will be bigger when a low accuracy scheme is used for the interpolation of the face center value.
Unfortunately, it is not always possible to generate a flow-oriented mesh in every region of a complex domain and, above all, for many industrial research cases it is not trivial to predict in every part of the domain which will be the orientation of the flow velocity.

In addition to the mesh orientation, also the geometrical quality of the mesh cells is important. The two most used parameters are the non-orthogonality and the skewness:

- Non-orthogonality: it is an index of the alignment between the vector connecting the centroids of two neighbouring cells and the vector normal to the face. When these two vectors are not aligned the truncation error resulting from the discretization of a spatial gradient (e.g. diffusive terms, laplacian terms) is affected and the accuracy is

penalized, thus a correction term is added to compensate the non-orthogonality (i.e. to preserve the original accuracy). Unfortunately, the additional correction term may produce an unbounded solution, especially for high values of non-orthogonality.

- Skewness: it is an index of the distortion of the grid, indicated as the distance between the face center and the intersection point between the face and the vector connecting the centroids of the neighbouring cells, normalized by the distance between the centroids. This distortion affects the interpolation process of the face center value of a flow quantity, since there will be a first interpolation starting from the cell center value and following the vector connecting the two cell centers and then a second interpolation is needed to reach the face center from the point on the face intersected by the vector connecting the two cell centers. This causes an additional term in the truncation error resulting from the discretization of convective terms which is the bigger the higher is the skewness index.

Also other mesh geometrical indexes have to be monitored in order to assess the good quality of a mesh, such as: face concavity, cell pyramid volume, face twist, cell aspect ratio and several others. The minimum value of all the mentioned quality parameters and many others to consider the mesh as valid can be set in the specific OpenFOAM dictionaries for mesh generation.

In case of significant gradients of the flow quantities are present, the refinement level of the mesh plays a key role in obtaining reliable results from the simulations. Therefore, higher levels of mesh refinement are generally applied in those regions of the fluid domain where high gradients of the flow quantities are expected, thus where it is important to reduce as much as possible the numerical errors. Indeed, the truncation error deriving from the interpolation of the face center value is always proportional to the mesh spacing elevated at a certain power that depends on the order of the scheme used. Thus, the error tends to zero faster for a more refined mesh. The level of mesh refinement becomes even more crucial when low accuracy schemes are used (i.e. first order schemes), since in that case the leading term of the truncation error is proportional to the mesh spacing at the first power multiplying the gradient of the flow property, thus introducing an artificial viscosity and tending to zero more slowly compared to second order schemes.

In conclusion, the mesh has to be generated trying to reduce as much as possible the extent of numerical errors, but keeping in mind that a certain error has to be taken into account and accepted, especially for complex fluid domain geometries and for an unsteady

flow behaviour which is really tough to predict, like in the case of internal combustion engines.
From this point of view, the semi-automatic mesh generation procedure made available by the LibICE library in OpenFOAM environment helps in achieving the minimum required mesh quality parameters, since the mesh is not generated if the setup does not allow to obtain a mesh quality compliant with the minimum parameters set by the user or the mesh motion process is stopped when the previously mentioned parameters are not anymore satisfied, consequently generating a brand new mesh and restarting the mesh deformation procedure. These features force the user to modify the mesh generation setup, until the mesh for all the crank angle positions have a sufficient quality and the duration of the motion of each mesh is satisfactory, so that a reasonable number of mesh is needed to cover the full cycle simulation.
For instance, during the initial mesh generation phase of the present work, some problems appeared, causing the failure of the process or a too short duration of each moving mesh in some critical phases, like the overlap phase.
By means of the OpenFOAM checkMesh utility and the possibility of visualizing the cells causing the invalidity of the mesh thanks to the ParaView program, it is possible to understand which are the regions of the mesh causing the problem, thus helping the user to identify where to apply modifications to improve the mesh quality. In this case the problems were related to some cells in the region between the valve and its seat that were causing the invalidity of the mesh after few degrees of mesh deformation, especially when the valve lift was low. These issues were solved by increasing the surface refinement of the patches of the lower part of the ducts, leading to an enhancement of the mesh quality where it was required, resulting in a higher average duration of each mesh in those critical phases.

4.1.1. STL division

The prerequisite for the mesh generation is the availability of an STL (Standard Triangulation Language) file of the engine. Then the user can specify in which regions inside or outside the closed surfaces of the STL a mesh has to be generated. The STL file represents the surfaces of a solid discretized through a combination of triangles connected to each other. Initially, the only file available as starting point for the this thesis work is an STL file where the whole engine is made up of just a single patch. However, for the meshing procedure it is necessary to have a series of STL files, which combined together make the final STL file of the engine made up of several patches. Having a number of different patches gives the possibility in the OpenFOAM environment of imposing different surface

refinements for each of the patches, that is important to refine the mesh only where it is required by the flow conditions or the mesh quality, without generating a high number of cells where not necessary. Moreover, the routines implemented in the LibICE utilities have the need of identifying some patches with a pre-determined name, needed for the STL and mesh motion processes (e.g. piston, liner, valves patches, ...).
Finally, the original STL file of the engine was divided into 30 different patches (Figure 4.1), which can be gathered in the macro categories: piston, liner, cylinder head, valves, ducts and pre-chamber.
Each of these patch macro categories can be further subdivided into a number of other patches. For instance, in the present work the intake and exhaust ducts were divided in several patches, in order to have the possibility during the setup of the meshing process of selecting the most adequate level of refinement for some specific surfaces, like the surface corresponding to the valve seat, without the need of increasing the surface refinement for the whole duct. The same strategy was adopted also for the valves, indeed each of them was divided into 6 different patches, as can be seen from Figure 4.2. For what concerns the pre-chamber, it was divided into 3 different patches: one for the pre-chamber body, one for the spark plug surface and one for the orifices.
The division of the original STL file of the engine into the desired patches was performed thanks to the Meshmixer software. This software offers to the user several functions to manipulate the triangulated surfaces of an STL file. A specific function helps to identify the surfaces of the geometry composed by triangles that have a normal in the same direction; moreover, the software gives the possibility of selecting one-by-one the triangles composing the STL file, which is very useful to extrapolate from the original file exactly the desired surface, creating a new STL file which will be considered as a new patch of the main file.

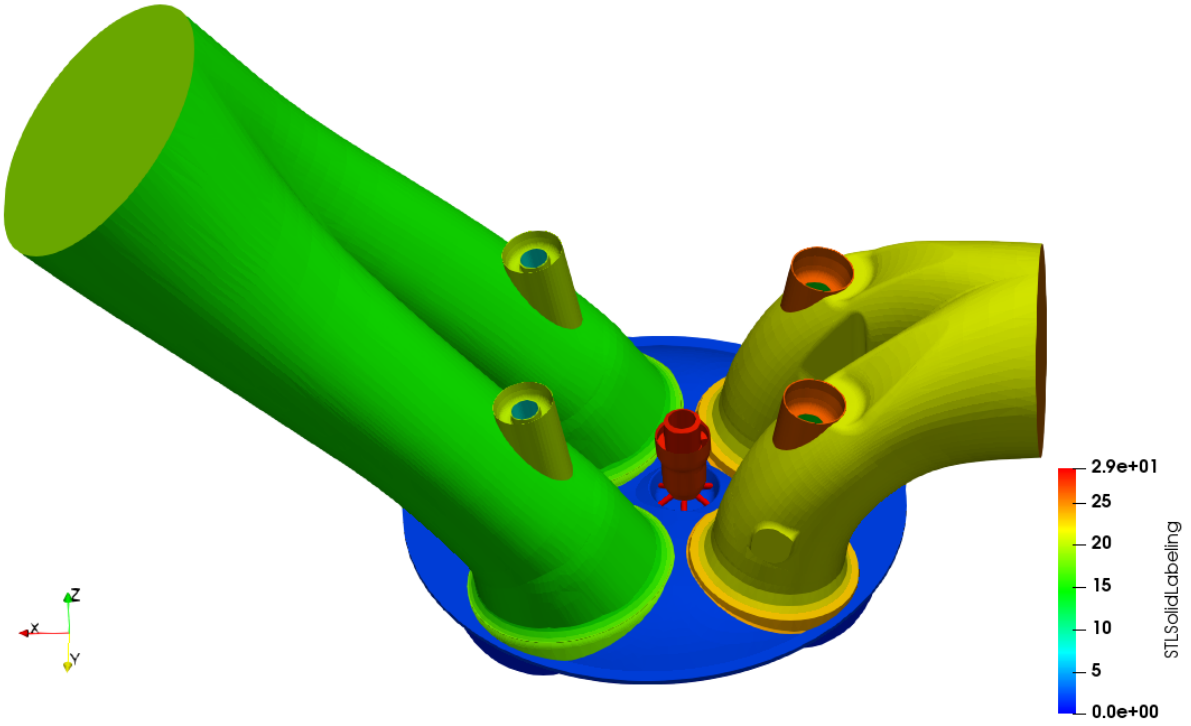

Figure 4.1: Engine STL file after division into different patches

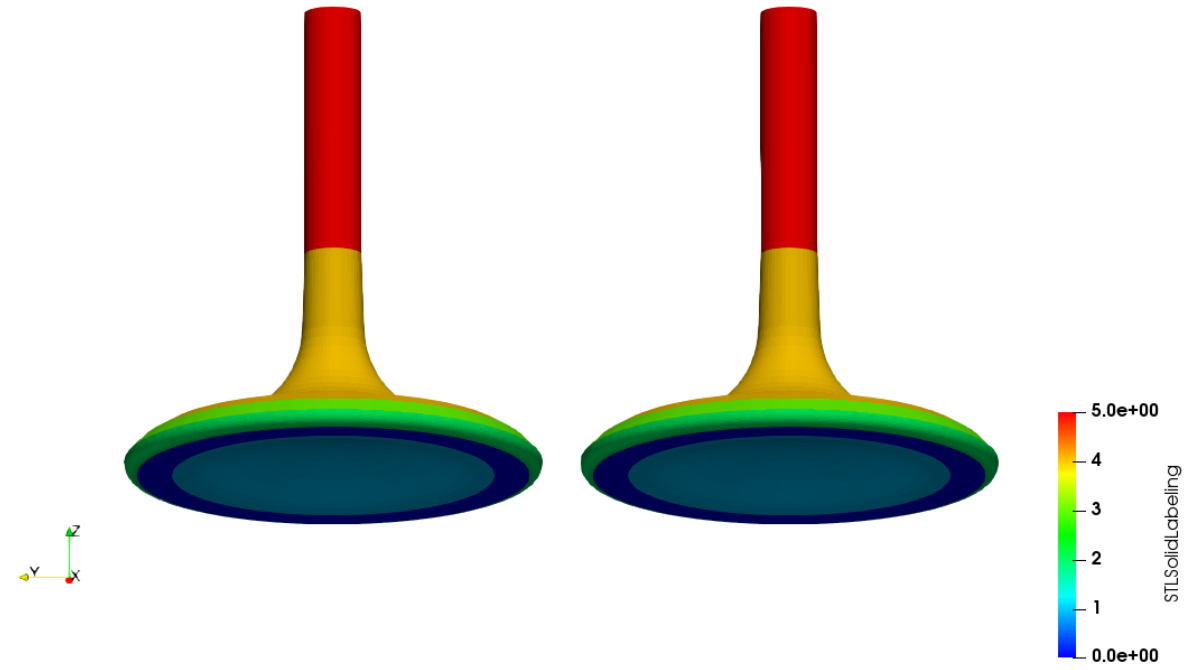

Figure 4.2: Division into patches of the intake valves

4.1.2. Mesh refinements

The mesh is divided into four main phases of the full cycle simulation, which are based on the valve timing and from now on will be referred as:

- Exhaust: when only the exhaust valves are open, thus from Exhaust Valve Opening (EVO) to Intake Valve Opening (IVO).
- Overlap: when both the exhaust and intake valves are open, thus from IVO to Exhaust Valve Closing (EVC).
- Intake: when only the intake valves are open, thus from EVC to Intake Valve Closing (IVC).
- Compression: when all the valves are close, thus for both the compression and expansion strokes of the real engine cycle, going from IVC to the next EVO.

The mesh of each of the above-mentioned phases has its own OpenFOAM dictionary, where all the parameters needed for the mesh generation process of that specific phase are indicated. Moreover, the LibICE library gives the possibility of generating other sub-dictionaries for each of the main phases, in order to have the possibility of modifying the mesh in the most flexible way where and when it is needed, specifying the crank angle from which the desired modifications have to be applied. As an example, in the present thesis work this possibility has been exploited to generate cylindrical refinements of a different height based on the valve lift, thus allowing to correctly reproduce the flow around the valves, but without wasting a high number of cells where the refinement is not anymore needed because the valve is in a position with a lower lift.
The valve timing of the moving mesh in OpenFOAM is not exactly equal to the one of the real engine. Clearly the lift law is the same, but the valves opening timing are delayed and the valves closing timing are anticipated. This is done because a valve is considered open or close by the software only when, according to the original lift law, it goes beyond or below a minimum lift of a value specified by the user. The reason behind this decision is for computational time saving: when the valve lift is very low, the space between the valve and the seat is extremely narrow, therefore a huge number of cells would be required to model the flow through that passage. As a consequence, the solution of imposing a pre-defined minimum lift is adopted in order to have a reasonable number of cells when the valve starts to open or its almost close. For the present thesis work, the minimum lift value below which the valve is considered close is of 0.25 mm.

In each of the dictionaries for the mesh generation procedure it is possible to specify

several parameters. Just to mention a couple of them, it is possible to set a level of surface refinement for all the different patches composing the engine STL file, but the most important feature is probably the possibility of generating some regions inside the mesh with various possible shapes and sizes that can be specified by the user, where a higher level of refinement can be set.
The refinement is intended to be a reduction of the side of the cells with respect to the base size in a specific region of the fluid volume. For the present thesis work, the base size chosen for the cells side is of 2.5 mm, which is a reasonable starting value considering the geometrical dimensions of the engine considered. The base size corresponds to a level of refinement equal to 0. By imposing in a certain region a refinement of level 1 means that the cell side will be halved (i.e. 1.25 mm) in the specified volume or on the specified surface. By increasing even more the refinement level, the cell side is further reduced by dividing each time by two the dimension of the cell of the previous level of refinement. In table 4.1 the size of the cell side for every level of refinement used in the present work is depicted.

	0	**1**	**2**	**3**	**4**
Cell side [mm]	2.5	1.25	0.625	0.313	0.156

Table 4.1: Refinement levels

In this case the mesh was generated for only half of the engine, exploiting the symmetry plane and hence having a mesh with a much lower number of cells, allowing to save a remarkable amount of time for the mesh generation procedure and, in particular, for the following simulations, especially considering the low computational power available.

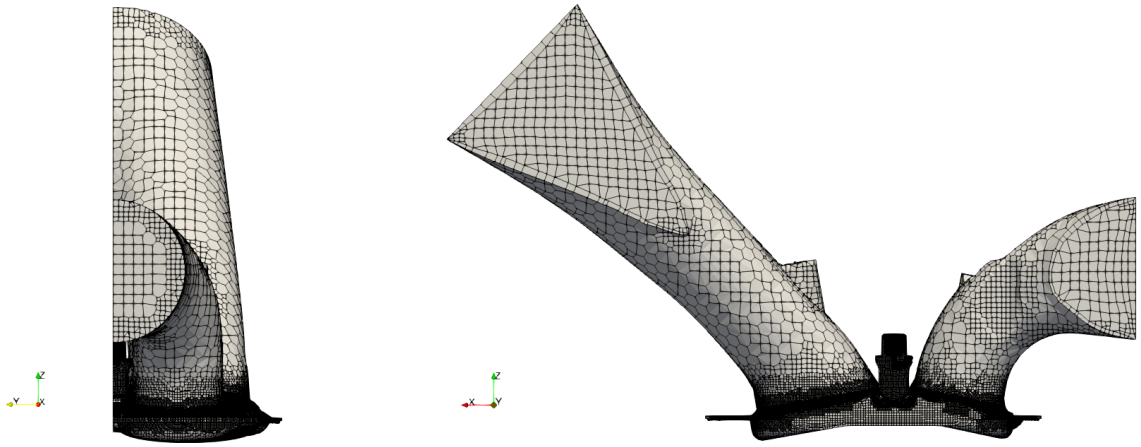

(a) Side view (b) Front view

Figure 4.3: Half engine mesh

The final mesh is characterised by cells with a side measure equal to the the base size only for the intake and exhaust ducts, because all the other regions of the engine are subjected to refinements of different levels, which are going to be discussed in a short while.

Cylinder refinements

The combustion chamber is characterised by a cylindrical refinement with a length greater than the entire piston stroke, in order to refine the cylinder for every position of the piston. The cylinder always has a level of refinement equal to 1, except for the parts of the engine cycle when the piston is close to the TDC, where a refinement of level 2 is applied to guarantee a sufficient number of cells between the surfaces of cylinder head and piston. More specifically, the higher level of refinement is applied for the whole overlap phase and in the range of ±25 CAD with respect to the TDC during the compression stroke.
Furthermore, a ring refinement of level 3 was applied to the annular region close to the edge of the cylinder head, in order to correctly model its geometry in that position. Other refinements are added when the piston is very close to the TDC (±15 CAD) to have a sufficient number of cells in the regions where the distance between piston and cylinder head is minimum.
The described refinements can be seen in Figure 4.4, where the the piston is in a position not far from the TDC (740°), and Figure 4.5.

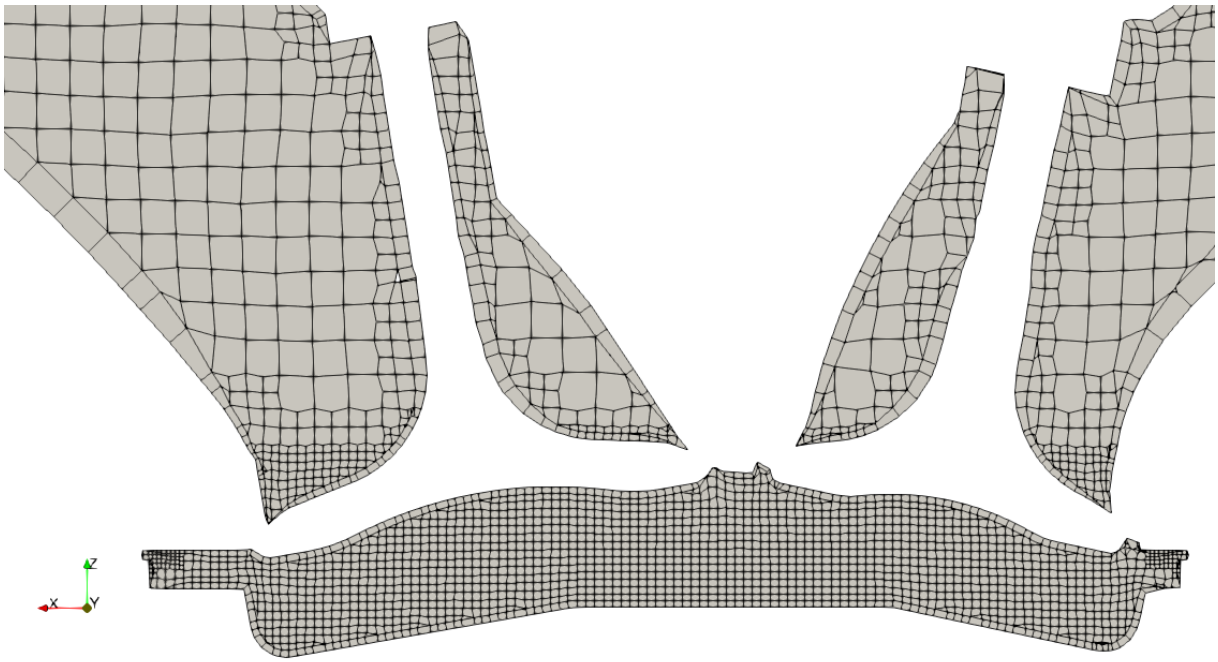

Figure 4.4: Engine section showing cylinder refinements

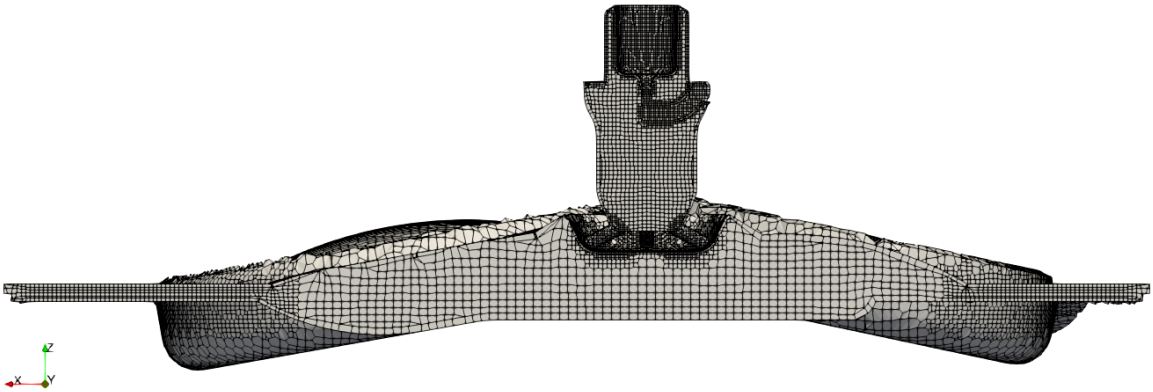

Figure 4.5: Additional refinements for piston at TDC

Valve refinements

Cylindrical refinements were applied to the volume around the valves during their motion, with an axis corresponding to the valve axis, a diameter greater than the valve dimension and a variable length depending on the valve lift.

The main refinement around each of the valves is of level 2, then a further cylindrical refinement of level 3 is applied when the valve is close to its seat (i.e. lift lower than $\simeq$ 3 mm) in order to guarantee a minimum number of cells between the valve and seat

surfaces, to obtain a correct flow modelling and to have a gradual transition of the cells dimension going from the narrow space between valve and seat to the cylinder and ducts mesh.
A specific function was set in the OpenFOAM dictionaries relative to the exhaust, overlap and intake phases to considerably increase the level of refinement in the space between the valve and its seat when the distance between these two surfaces gets below a value that is too low to allow to the local mesh size to correctly reproduce that space.
The result of the application of all the mentioned refinements can be seen in Figure 4.6, displaying a moment nearby the intake valve closing event.

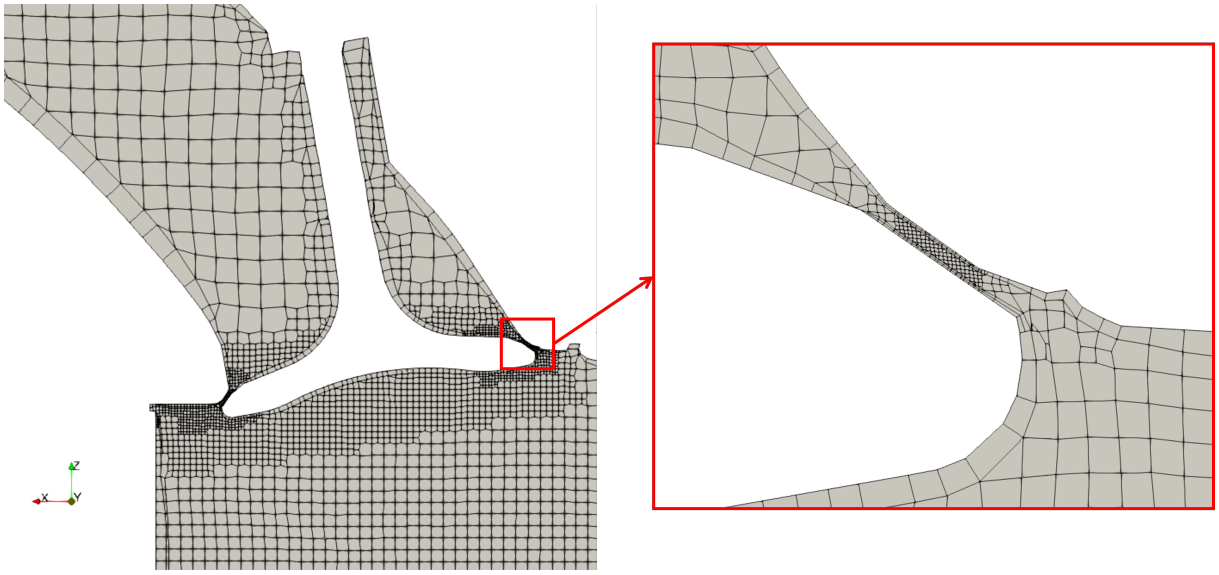

Figure 4.6: Engine section showing valve refinements

Pre-chamber refinements

The pre-chamber is characterized by a very small volume compared to the main combustion chamber (i.e. 2% of the main chamber clearance volume), thus a higher level of refinement is needed to properly reproduce the gas flows inside it. For the present work it was chosen to use a cylindrical refinement of level 3 for the whole pre-chamber volume and a spherical refinement of level 4 enclosing each of the pre-chamber orifices. To guarantee a gradual transition of the cell dimension moving from the pre-chamber orifices to the cylinder, for each of the orifices a further spherical refinement of level 2 with a greater radius was created to surround the smaller higher-level spherical refinements. Lastly, a refinement of level 4 on the spark plug surface was imposed in order to correctly reproduce its shape.

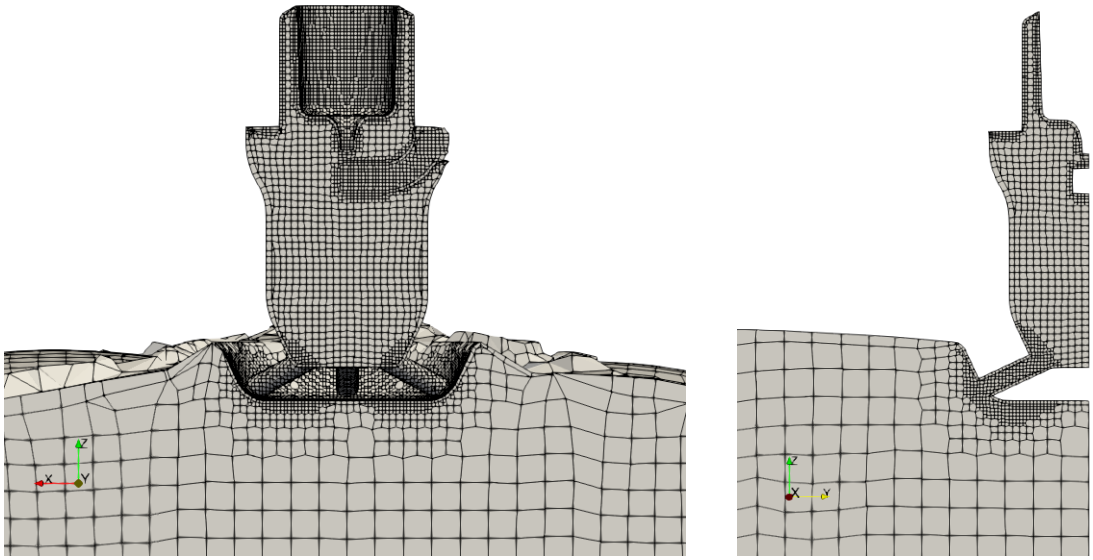

(a) Front view (b) Section

Figure 4.7: Pre-chamber mesh

Other mesh features

Another option offered by the OpenFOAM mesh generation utility is the possibility of adding some layers through an extrusion process on the surface of the various patches. Having a layered mesh in correspondence of the surface means having a very regular mesh which is flow-oriented (since close to the surface the flow will follow the shape of the object), thus helping to reduce the diffusion of the numerical error. The addition of a layer is important also to have the opportunity of better monitoring the value of the non-dimensional wall distance (y^+), which is a relevant parameter to be tuned based on the turbulence model used. For instance, in the case a $k-\varepsilon$ turbulence model is used, the layer thickness has to be chosen in order to guarantee that the y^+ always stays above a certain value (i.e. typically $y^+ > 30$), since this turbulence model does not solve the flow up to the wall, but imposes a wall function which represents a known behaviour of the flow boundary layer. For these reasons a layer was added on all the surfaces of the engine, with a thickness equal to the 80% of the cell size of the region where the layer is extruded. Only for the surfaces of the valve seat and its corresponding part two layers were added, since it was useful to solve some mesh quality issues in that region and guarantee a longer duration of each mesh, especially during the intake valve opening and closing phases.
The layers can be clearly noticed in all the figures presented in the previous paragraphs of this section (figures from 4.4 to 4.7).

Finally, the result produced by the mesh generation process is that the full engine cycle (i.e. 720 CAD) is covered by 123 mesh, with an average duration of each mesh of approximately 5.85 CAD and an average number of cells along the entire cycle of about 275k. For the present work, the maximum duration allowed for each mesh was set at 10 CAD in order to avoid an excessive stretching of the cells, but this duration is achieved only when the minimum mesh quality parameters are satisfied during the whole mesh deformation process, otherwise when the mesh is considered not anymore valid the mesh motion process stops and a new mesh is automatically generated, restarting from the crank angle where the previous one was stopped. In table 4.2 a more detailed description of the mesh characteristics divided by the different engine phases is shown.

	Exhaust	**Overlap**	**Intake**	**Compression**
Average mesh number of cells	215k	410k	306k	158k
Average mesh duration [CAD]	8.73	2.24	5.20	7.72

Table 4.2: Mesh data

Clearly the highest average number of cells is during the overlap phase, since both the valves are open and the piston is in the proximity of the TDC, thus a higher number of mesh refinements is activated compared to the other engine phases. The intake phase has a higher average number of cells in comparison with the exhaust phase because the intake valves have a greater diameter compared to the exhaust ones, thus the refinements occupy a bigger volume. The maximum number of cells is of 759k, achieved for the very first mesh of the overlap phase, where both the intake and exhaust valves are open, with the intake valve being in the minimum lift position and thus requiring a high number of cells for the narrow space between valve and seat. The minimum number of cells is of 105k, achieved for a generic mesh during the compression phase, sufficiently close to the TDC, thus having a small cylinder volume, but also not so close to the TDC so that the higher level of refinement for the cylinder has already been deactivated.
The most critical phases for the mesh deformation procedure are the ones where the valves are in proximity of the minimum lift position and when the piston is close to the TDC, since a higher number of refinements is activated. For these reasons the phase characterised by the shortest average mesh duration is the overlap phase.
In the following figure the trend of the number of cells over the full engine cycle and the duration of each mesh can be seen.

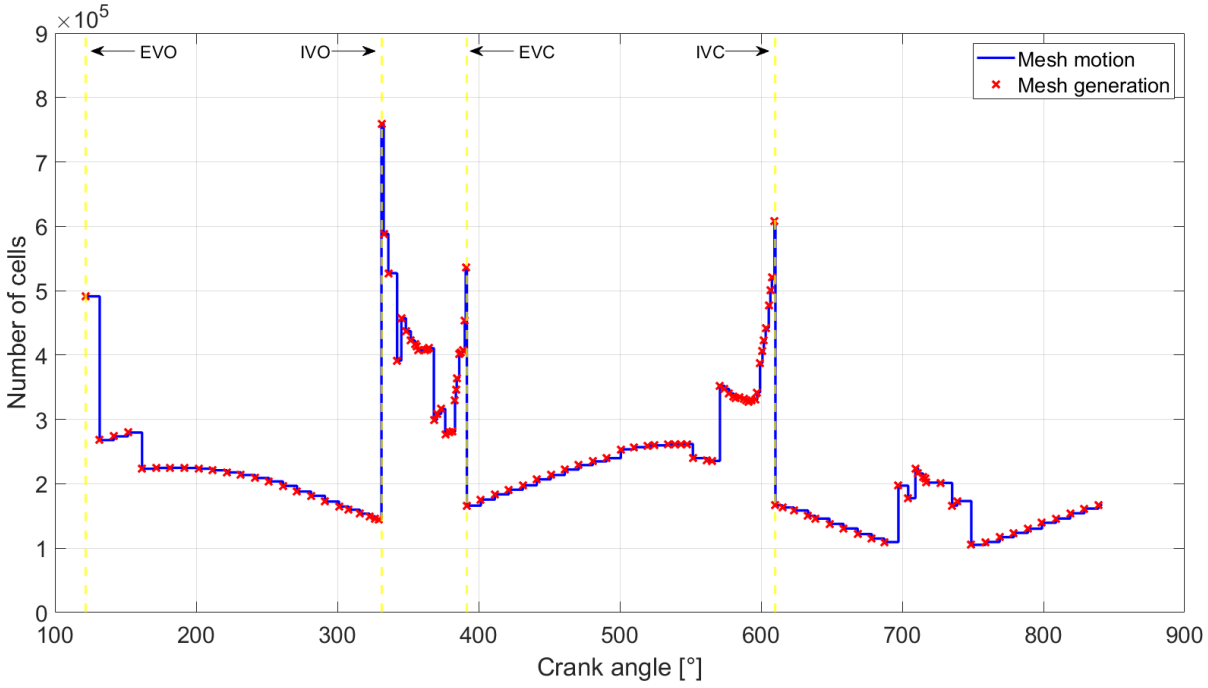

Figure 4.8: Number of cells per mesh over the engine full cycle

As it can be noticed from Figure 4.8, the peaks of number of cells are always in correspondence of the valve openings and closings, due to the OpenFOAM function described some paragraphs ago, that automatically increases the number of cells to properly model the space between seat and valve at minimum lift position. The global ascending or descending trends are caused by the piston motion that varies the cylinder volume, while an increase of the number of cells around the two TDCs is present due to the higher refinement imposed for the cylinder volume.

4.2. Initial and boundary conditions

For the simulation setup, several data have to be specified in the designated OpenFOAM and LibICE dictionaries.

For the mesh motion it is necessary to indicate all the engine geometrical parameters, namely bore, stroke, rod length and pin offset, that then will be automatically translated into the piston motion law by the LibICE code. The engine rotational speed must also be specified to define the piston velocity. In the present work, it was chosen to investigate the operative point corresponding to 10500 rpm at full load, which is the maximum engine power condition. Consequently, also the valve timing related to the chosen operative condition have to be specified for the mesh motion. The valve lift laws supplied by the

engine manufacturer were referred to the piston TDC position (i.e. the TDC corresponds to 0 CAD), but the LibICE routines are implemented having as 0 CAD the position of vertical crank, which in this engine is preceding the TDC position, since it is characterised by a positive pin offset. Therefore, the valve timing were translated of approximately 2.7°, which is the angular offset between the vertical crank position and the TDC.
Finally, as already explained at the beginning of section 4.1.2, the valve timing used in the OpenFOAM simulation is not coincident with the one of the real engine. In the following table are indicated the valve opening and closing timing already shifted of the amount needed to have a correct compatibility with the LibICE rule, and in Figure 4.9 the real lift laws are compared to the ones used in OpenFOAM.

	EVO	**IVO**	**EVC**	**IVC**
Real engine valve timing [CAD]	99.7	304.2	413.7	638.2
Simulation valve timing [CAD]	121.7	331.2	391.7	610.2

Table 4.3: Valve timing

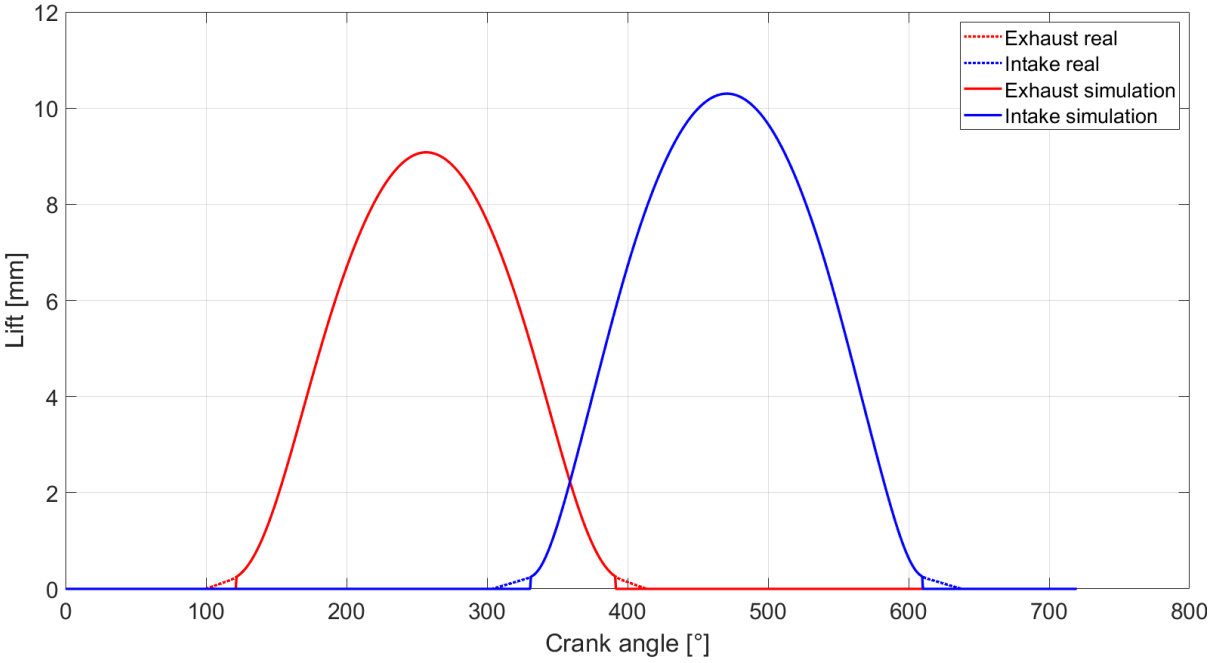

Figure 4.9: Valve lift profiles

The simulation will start from the exhaust valve opening event, therefore the initial conditions corresponding to this crank angle have to be set in the various regions of the engine, supposing that a fired cycle took place before the cold-flow cycle that is going to be simulated. Furthermore, some boundary conditions have to be imposed on the material and immaterial surfaces of the engine.
At the inlet and outlet patches (i.e. the immaterial surfaces where the fluid flows in or out) were imposed two boundary conditions: one for the total pressure and one for the temperature. By specifying the total pressure, also the velocity value is fixed. The choice of imposing these boundary conditions allows to have a well-posed fluid-dynamic problem and guarantees a good stability of the simulation. The boundary conditions applied are time-varying, reproducing the pressure and temperature oscillating traces in the intake and exhaust ducts. Both these curves were obtained from the 1D simulation, where these conditions were needed to obtain a simulated pressure curve in cylinder compatible with the one obtained from the test bench.
For what concerns the material surfaces, usually these do not exactly correspond to the patches in which the original STL file was divided (as described in section 4.1.1), since that first subdivision was mainly aimed at the mesh generation procedure. For the purpose of setting up the boundary conditions, the numerous patches can be gathered into main groups that will share the same boundary conditions. For example, all the patches relative to the intake duct are gathered under the same category and just one boundary condition for each physical quantity will be assigned.
For each of the solid walls a fixed temperature was imposed based on rough typical values for this kind of engine, since it is not easy to measure or to precisely estimate the temperature of the material surfaces. The surface temperature boundary conditions imposed for each of the engine components are listed in the following table:

	Temperature [°C]
Liner	120
Piston	135
Cylinder head	130
Pre-chamber walls	275
Pre-chamber orifices	375
Intake duct and valve walls	70
Exhaust duct and valve walls	160

Table 4.4: Wall temperatures

It can be noticed from table 4.4 that the temperature assigned to the liner is lower compared to the cylinder head and piston temperatures: this assumption comes from practical experience and is due to the fact that the liner can exchange a greater amount of heat thanks to the more favourable position of the cooling channels around it compared to other components. The pre-chamber wall temperature was set higher compared to the temperatures of the main combustion chamber walls, since it was supposed that it keeps a higher average temperature over the engine full cycle compared to the one of the cylinder walls, because of its higher thermal conductivity and hence greater heat absorption from the hot gas after combustion (i.e. the pre-chamber is made of a more conductive material compared to the cylinder head). In the engine considered for the present work, the cooling circuit was modified to let the coolant flow also around the pre-chamber, however the channels cannot pass nearby the pre-chamber orifices; moreover, also the very high velocity reached by the burnt gases flowing through the orifices after combustion contributes to a greater convective heat exchange in this area, therefore the surface temperature of the pre-chamber orifices was set higher compared to the rest of the pre-chamber. It has to be kept in mind that for all the surfaces a fixed value of temperature was imposed, assuming it as an average value over the full cycle. Actually, the wall temperature of all the surfaces varies over the cycle and, in addition, the temperature is not perfectly uniform on a surface, but it has a certain spatial distribution. However, it is very complicated to give an estimate about these aspects, therefore they will be both neglected.
Regarding the mesh motion, the boundary conditions are imposed such that the piston and all the valve surfaces are rigidly moving, except for the valve stem, which is deforming to guarantee the movement of the rest of the valve surfaces. The other surface that undergoes a deformation is the liner, that has to extend or compress to accommodate the piston motion. The rest of the surfaces are considered as fixed walls.
For what concerns the turbulence modelling, wall functions are imposed on every material surface according to the chosen $k - \varepsilon$ turbulence model.

For the enforcement of the initial conditions for the simulation start at EVO, four different volumes were defined: intake duct, exhaust duct, cylinder and pre-chamber. In each of these regions were imposed: static pressure, temperature and mass fractions of the molecular species. Pressure in cylinder and pre-chamber were imposed equal to the values found from experimental tests at the crank angle corresponding to the simulation EVO, whereas all the other values of pressure in the ducts and temperature everywhere were available as results of the 1D simulation. The mass fractions were imposed by assuming an ideal combustion between air and fuel at the indicated λ ratio, considering air composed only by oxygen and nitrogen (volumetric fractions of $79\%N_2$ and $21\%O_2$)

and octane as fuel. Inside the intake duct were imposed the mass fractions corresponding to the reactants, while in the exhaust duct, cylinder and pre-chamber were imposed the mass fractions corresponding to the the products of the ideal combustion reaction of a rich air-fuel mixture, according to the following formula:

$$C_8H_{18} + \lambda \cdot \alpha_{O_2,st} \cdot \left(O_2 + \frac{79}{21} N_2 \right) \quad \longrightarrow \quad n_{CO_2} \cdot CO_2 + n_{H_2O} \cdot H_2O + n_{N_2} \cdot N_2 + n_{fuel} \cdot C_8H_{18}$$

As an example, Figure 4.10 shows the temperature in the different regions of the internal mesh after imposing the initial conditions for the start of the simulation.

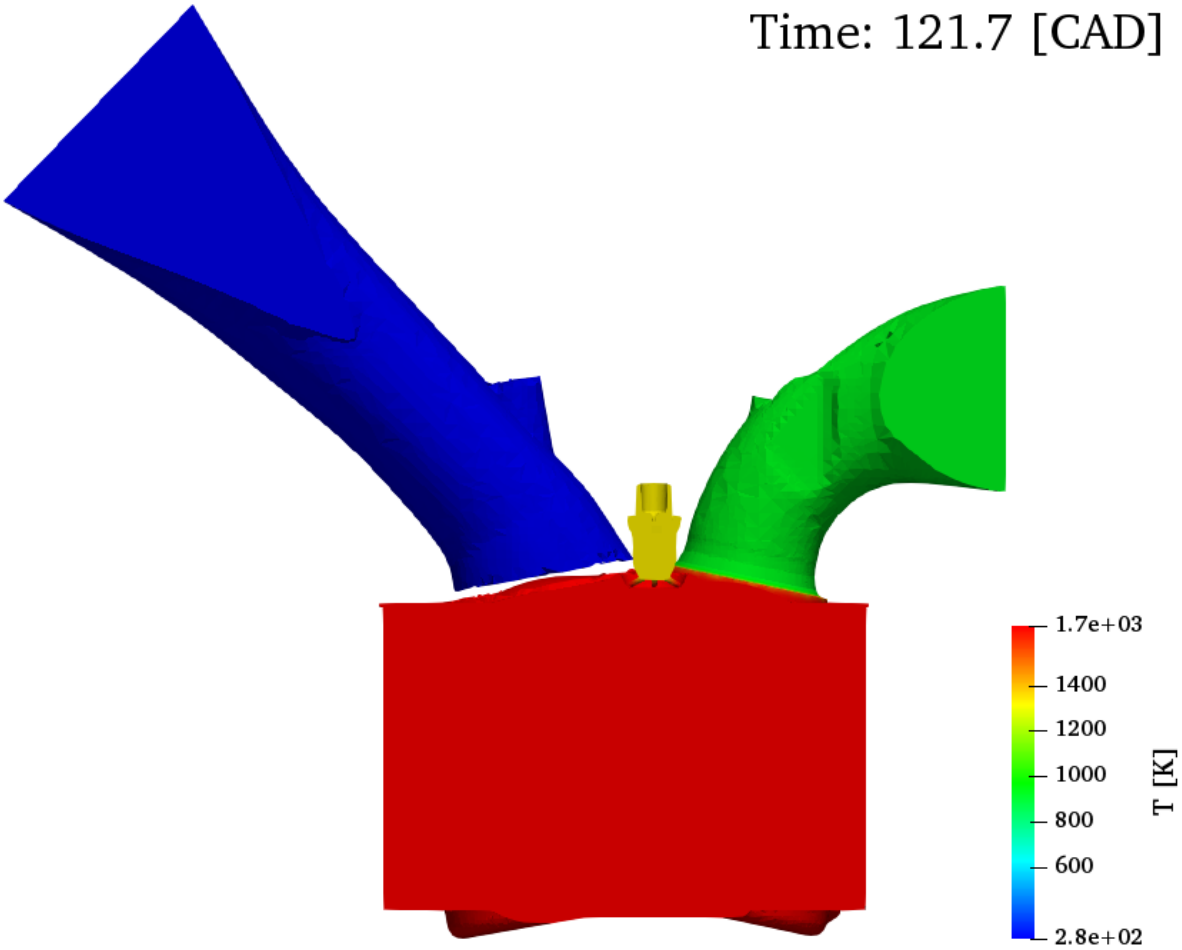

Figure 4.10: Initial conditions: temperature

It can be noticed from Figure 4.10 that the initial gas temperature in the pre-chamber is lower than the temperature in the main chamber. The reasons of this difference are mainly two: the surface-to-volume ratio of the pre-chamber is higher compared to the one of the cylinder and the pre-chamber is made of a material with a much higher thermal

conductivity compared to the material of the cylinder walls. Moreover, for the engine subject of this thesis work, also the pre-chamber is surrounded by a cooling circuit. Eventually, the result is that after combustion the gas temperature reduces more quickly inside the pre-chamber compared to the gas temperature inside the cylinder.

Time step definition

Another important parameter to choose is the time step of the simulation, which has to be specified for each mesh composing the full engine cycle, so in this case a vector of 123 time step values had to be specified, since the full cycle is divided into 123 mesh. Thanks to the LibICE library, the time step can be set in CAD, then the code will automatically convert it in seconds, since OpenFOAM needs inputs according to the international system of units. Initially, the time step was chosen sufficiently low to guarantee the stability of the simulation: in this work it was set at 0.002 CAD. Then, after the first simulation, the values of the maximum Courant number during the time duration of each mesh were analyzed and the time step modified accordingly in order to obtain a Courant number around 1, that is needed to guarantee the reliability of the simulation results.
The Courant number, also known as Courant–Friedrichs–Lewy condition, is an indicator for choosing the most appropriate time step, once the mesh size is defined for each phase of the simulation. It is defined as:

$$C = \frac{U \cdot \Delta t}{\Delta x} = \frac{U}{U_{lim}}$$

As it can be seen from the above equation, the Courant number correlates the propagation velocity of the pressure wave U with a limit velocity that depends on the mesh spacing Δx and on the time step Δt. Therefore, to be sure to correctly reproduce the fluid behaviour, the time step has to be chosen so that the flow travels less than one cell in one time step. For most of the mesh composing the full cycle simulation, the Courant number was low, because of the low initial time step. As a consequence, it was increased where applicable, leading to a considerable reduction of the computational time needed for the simulation, without impacting on the reliability of the results. After some iterations (i.e. more than one simulation), needed to precisely tune the time step for each mesh to obtain a Courant number as close as possible to 1, the minimum value of the time step was still 0.002 CAD in some phases of the full cycle, namely most of the overlap phase and, in general, when the valves are close to the minimum lift position. Indeed, in those situations the very small size of the cells needed to model the space between valve and seat requires a small time step to satisfy the CFL condition (i.e. $C \leqslant 1$).
On the other hand, for the most part of the exhaust, intake and compression phases it

was possible to use a much higher time step, which was usually in the range of 0.01-0.02 CAD.

4.3. Numerical setup

The initial setup for the discretization schemes of the various terms composing the fluid flow governing equations was based on some standard choices to ensure the simulation stability, according to the discretization schemes available in OpenFOAM.
The time derivatives are always discretized with an *Euler* scheme, thus relying on the value of the calculated quantity at the previous time step.
The gradient terms are discretized with the scheme *cellLimited Gauss linear 1.0*, since a purely second order *Gauss linear* scheme cannot guarantee a bounded solution, hence leading to instabilities that in turn cause the crash of the simulation. With the *cellLimited* option, the cell gradient is limited to ensure that the face values obtained by extrapolating the cell value to the cell faces using the gradient are bounded by the neighbouring cells minimum and maximum limits.
For the Laplacian terms a standard *Gauss linear limited 0.33* scheme is always used.
The schemes where there is a greater freedom for modifications are the ones for the discretization of the divergence terms, which are fundamental for the stability of the simulation and the accuracy of the final results, as seen in section 2.2.1. The very first simulations were performed by imposing first order discretization schemes (i.e. *upwind*) for the most important divergence terms, like pressure, velocity and mass fractions, with the aim of enforcing a sufficient stability of the simulation to obtain preliminary results. Later on, several attempts were performed to gradually enhance the accuracy of the results by moving towards second order schemes, without losing the already achieved simulation stability.
The various tests on the divergence discretization schemes will be discussed more in detail in the following section.

For what concerns the iterative process for the solution of the linear systems seen in section 2.2.2, it was used a solver implemented in the LibICE library specifically designed for the cold flow simulation of internal combustion engines. The solver is based on the well known PIMPLE algorithm that determines the sequence of operations that the software follows to solve each of the RANS equations combined with the turbulence model equations. This algorithm is generally used for unsteady problems when the time step cannot be too small in order to reduce the computational time needed for completing the simulation, therefore the PIMPLE loop was considered to be the best choice.

The relaxation factors were all set equal to 1, which corresponds to no relaxation, therefore giving as output the value of the quantity calculated by the equation without any modification and speeding up the iterative process.
For the calculation of all the flow quantities, the same linear solver was used to solve the matrix problem, which was a stabilized pre-conditioned bi-conjugate gradient solver (i.e. PBiCGStab), with a diagonal incomplete-LU (i.e. DILU) pre-conditioner. This is a quite standard choice for solving linear problems involving non-symmetric matrices. An absolute tolerance and a relative tolerance must be specified for all the quantities to be calculated in order to determine when convergence is considered to be reached, based on the value of the residual. The iterative solver stops when one of these two specified tolerance values for the residual is reached.
In the present work, several tests on the absolute tolerance were performed, by gradually decreasing its value to be sure that the final results were sufficiently accurate. The final setup is characterised by an absolute tolerance value of 10^{-20} for most of the calculated quantities, which, considering the results of the previous tests, was considered as sufficiently low to obtain reliable results, without an excessive increase of computational time.

4.3.1. Discretization schemes: results comparison

As previously described, some tests were performed to try to obtain the most accurate simulation results, by comparing the results obtained using a first order discretization scheme for the divergence terms to the ones obtained using schemes with an accuracy much more close to second order.
The first step consisted in switching to a near second order setup using some standard schemes for the most important flow quantities, moving from *upwind* scheme to *limitedLinear 1.0* scheme for all the quantities except for the divergence of the velocity, which was discretized with a *linearUpwind* scheme. The *limitedLinear* is a second order scheme with a flux limiter that limits the solution towards the one obtained by an *upwind* scheme where strong gradients are detected, with a limitation that is the bigger the higher is the limiting factor specified, while *linearUpwind* is a scheme that blends the advantages of the *linear* and *upwind* schemes, having a higher accuracy compared to the first order scheme and a higher stability compared to the second order scheme. The list of the discretization schemes for the divergence terms in the designated OpenFOAM dictionary for the initial and the enhanced configurations looked like the following:

```
divSchemes
{

    default none;

    div(phiU,p)                         Gauss upwind;
    div(phi,U)                          Gauss upwind;
    div(phi,Yi_h)                       Gauss upwind;
    div(phid,p)                         Gauss upwind;

    div(phi,k)                          Gauss upwind;
    div(phi,epsilon)                    Gauss upwind;

    div(phi,K)                          Gauss upwind;
    div(meshPhi,p)                      Gauss upwind;

    div(((rho*nuEff)*dev2(T(grad(U)))))  Gauss linear;
    div(U)                              Gauss linear;
    div(facMeshPhi,oneSolve)            Gauss linear;

}
```

(a) 1st order

```
divSchemes
{

    default none;

    div(phiU,p)                         Gauss limitedLinear 1.0;
    div(phi,U)                          Gauss linearUpwind grad(U);
    div(phi,Yi_h)                       Gauss limitedLinear 1.0;
    div(phid,p)                         Gauss limitedLinear 1.0;

    div(phi,k)                          Gauss limitedLinear 1.0;
    div(phi,epsilon)                    Gauss limitedLinear 1.0;

    div(phi,K)                          Gauss limitedLinear 1.0;
    div(meshPhi,p)                      Gauss limitedLinear 1.0;

    div(((rho*nuEff)*dev2(T(grad(U)))))  Gauss linear;
    div(U)                              Gauss linear;
    div(facMeshPhi,oneSolve)            Gauss linear;

}
```

(b) 2nd order

Figure 4.11: Divergence schemes setup

As it can be seen from the following graphs of pressure, temperature and mass trapped inside the cylinder, some differences can be noticed, but no dramatic changes can be detected and the general trends are quite similar. The difference of trapped mass at IVC visible in Figure 4.14 is around 1.5%, which is not so significant, but also not negligible. These results lead to the conclusion that the error produced by the use of a less accurate scheme is not so big, probably thanks to the good mesh quality.

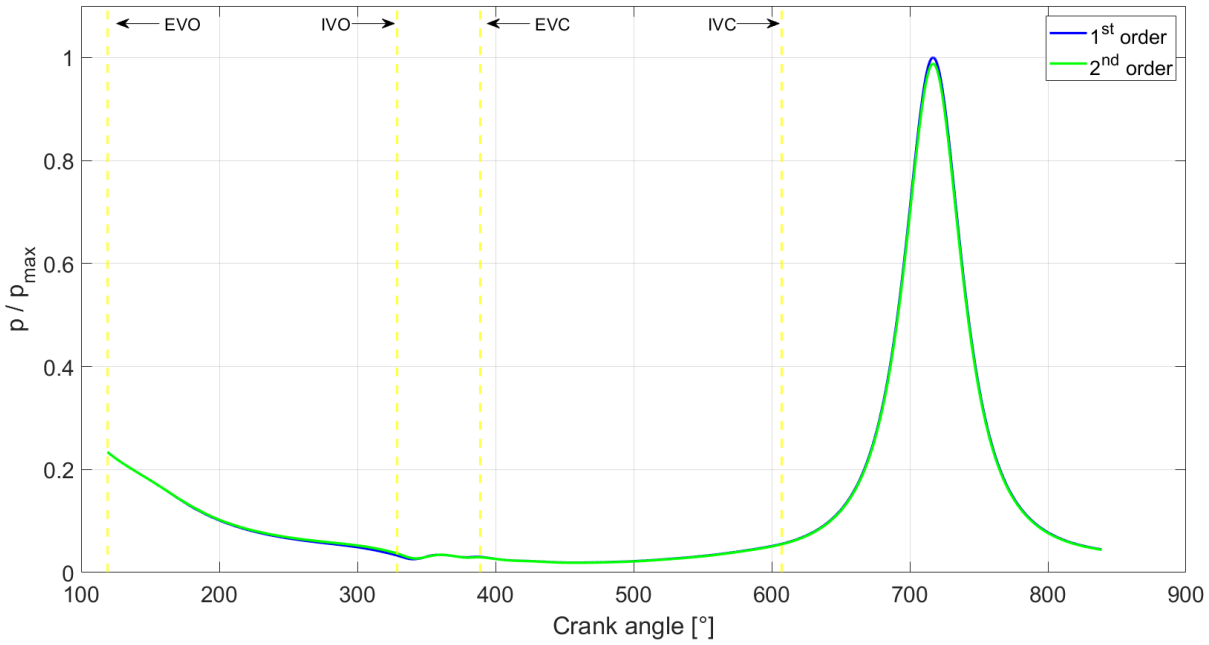

Figure 4.12: Pressure in cylinder: 1st and 2nd order schemes

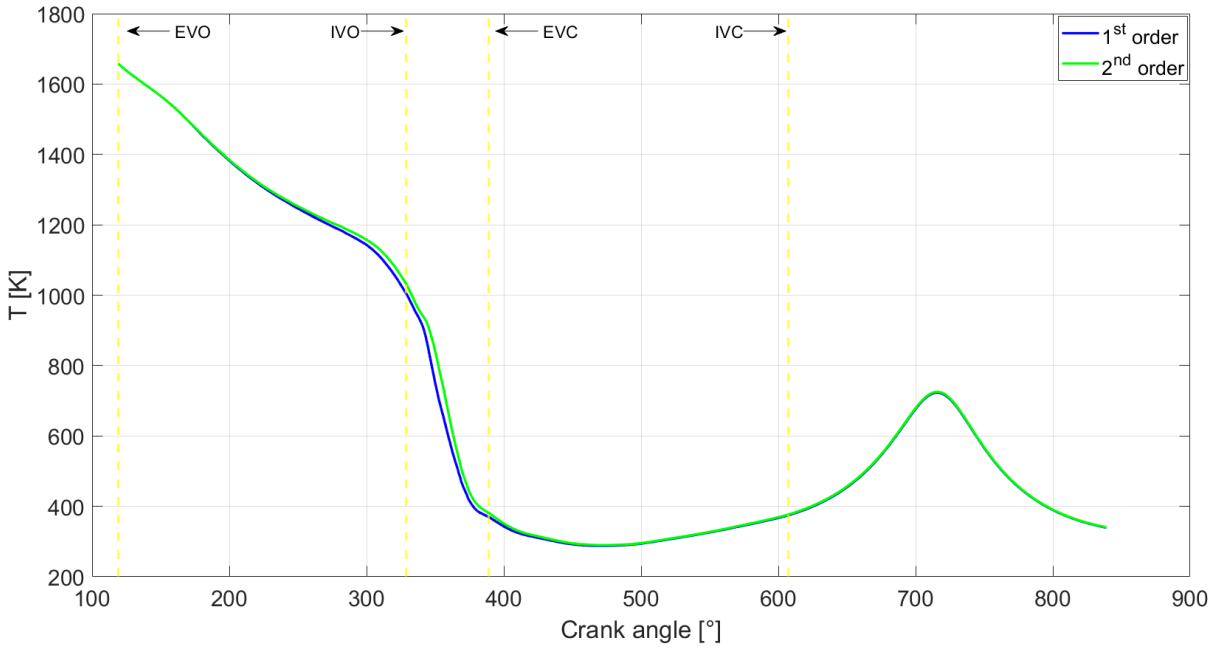

Figure 4.13: Temperature in cylinder: 1st and 2nd order schemes

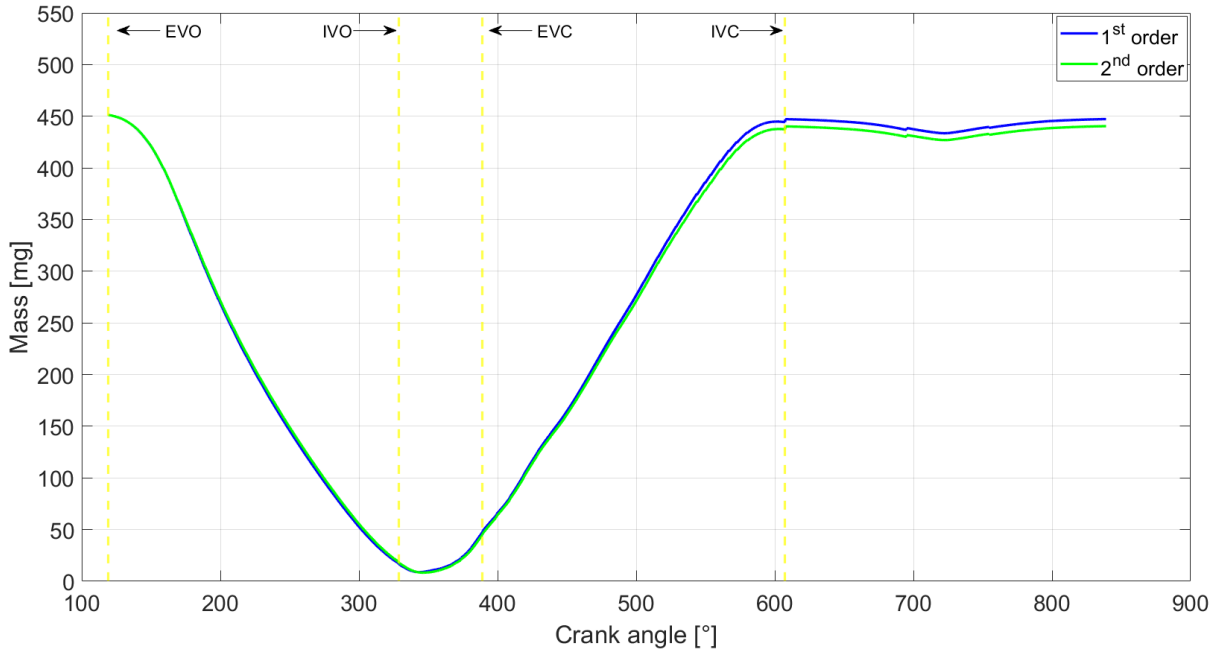

Figure 4.14: Mass trapped in cylinder: 1st and 2nd order schemes

The second step consisted in modifying the value of the limiter from 1.0 to 0.1 for all the divergence terms, with the aim of tending as much as possible towards a purely second

order accurate scheme. This modification did not produce any significant change and therefore the curves of the main flow quantities were almost perfectly overlapped for the two configurations.

At this point, also the scheme for the divergence of the velocity was modified, moving from *linearUpwind* to *limitedLinear 0.1*. This action produced a relevant variation of the main flow quantities, as shown in Figures 4.15, 4.16 and 4.17, resulting in a different behaviour of the pressure and temperature curves, with a lower temperature during the whole full cycle and a pressure which is lower during the exhaust phase and higher during the intake and compression phases, leading to an increase of 10 mg of trapped mass in cylinder at IVC.

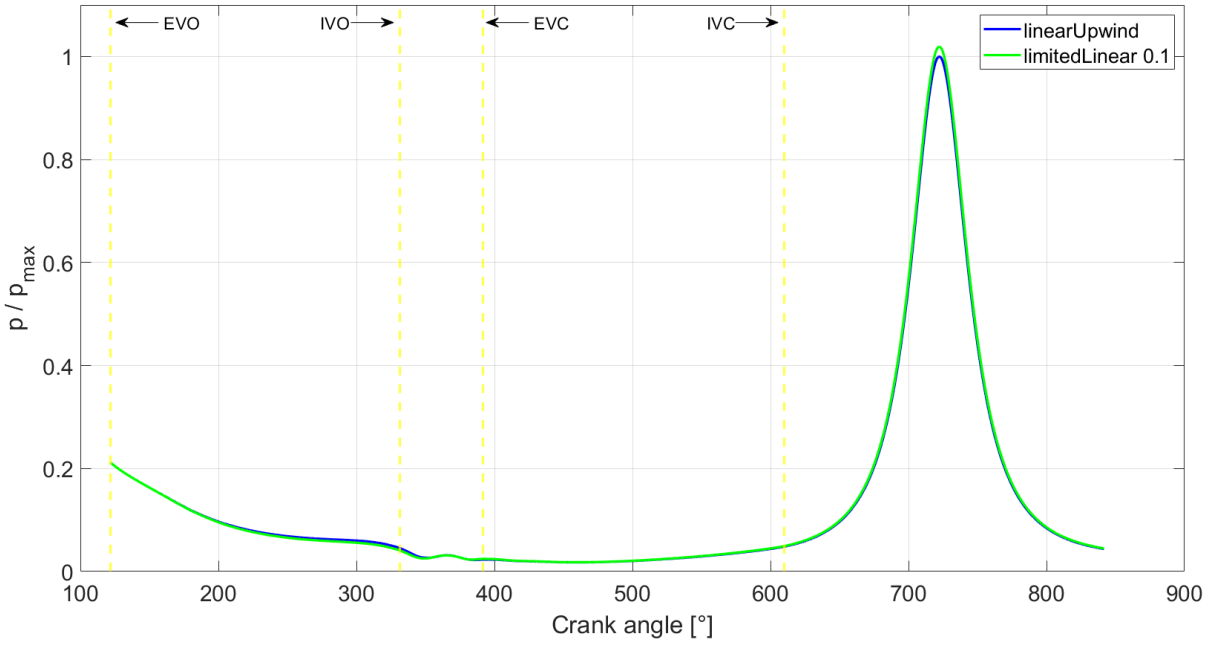

Figure 4.15: Pressure in cylinder: schemes comparison for div(phi,U)

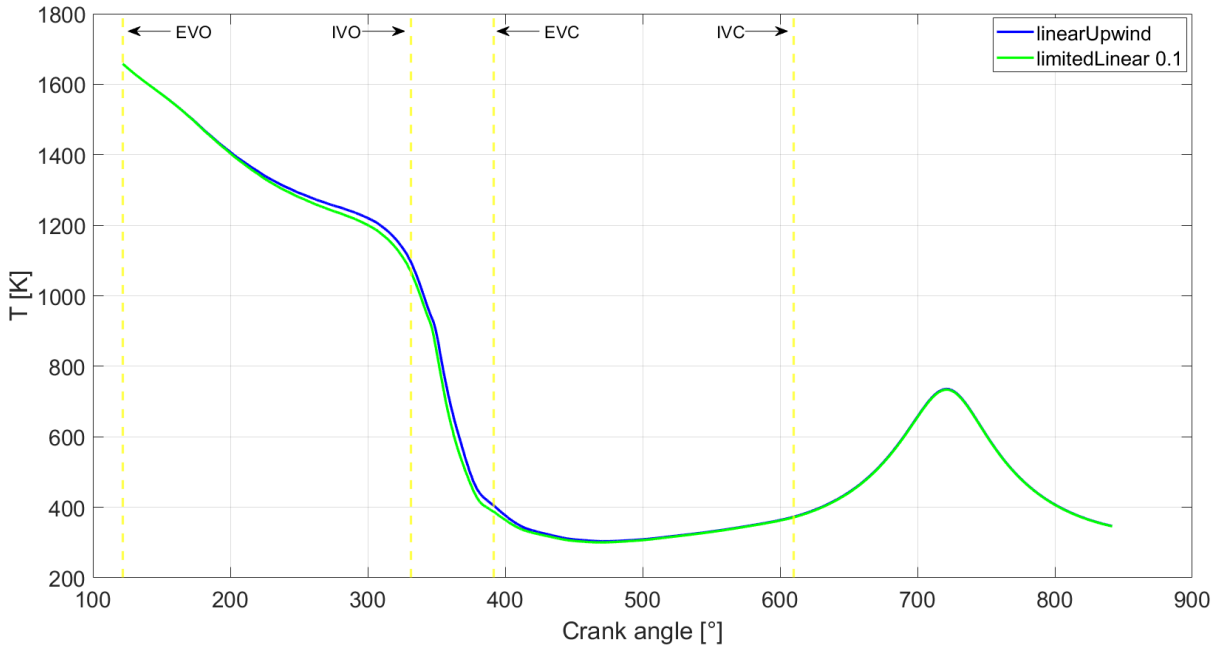

Figure 4.16: Temperature in cylinder: schemes comparison for div(phi,U)

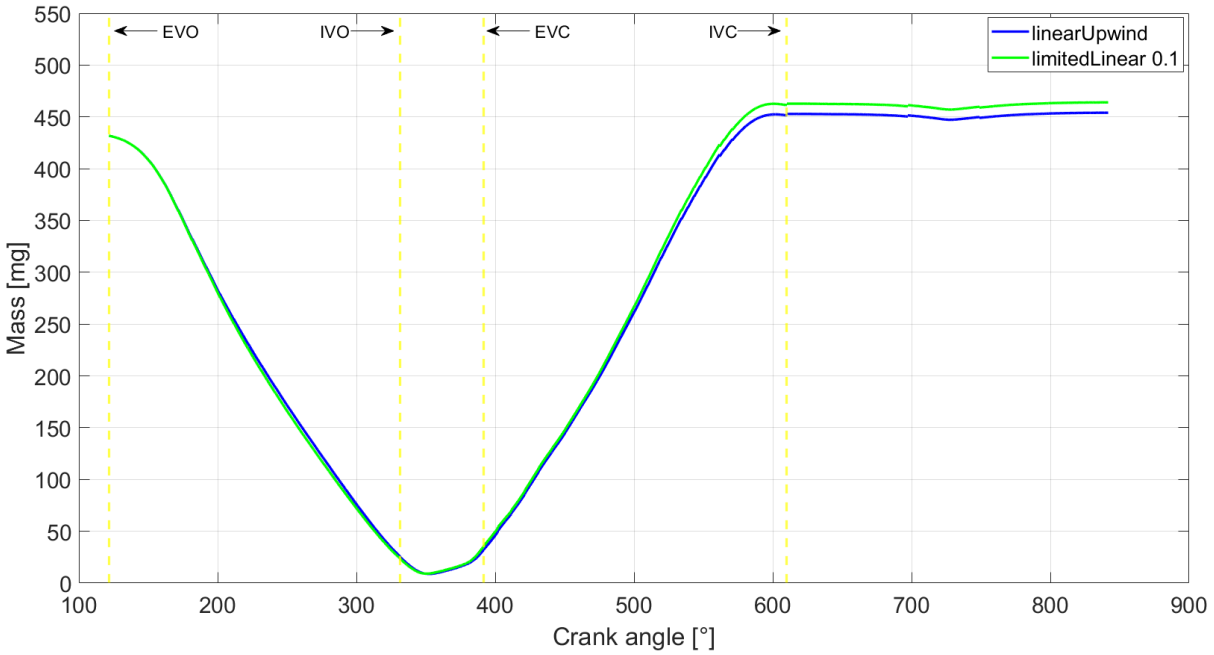

Figure 4.17: Mass trapped in cylinder: schemes comparison for div(phi,U)

Some other attempts were done by trying to use a fully second order accurate *Gauss linear* discretization scheme for the various divergence terms, but this option always led

to unbounded results that caused the simulation crash.

While for the usual flow physical quantities, like pressure and velocity, it is straightforward to prefer second order schemes in spite of first order schemes thanks to their greater accuracy as a consequence of the smaller truncation error, for the turbulence quantities different considerations must be done. In the present work, both *upwind* and *limitedLinear 0.1* schemes were tested for the discretization of the convective terms in the turbulence model equations: the results showed that the choice of the scheme has a very limited influence on the main flow quantities (i.e. the curves of pressure, temperature and trapped mass were almost perfectly overlapped for the two cases), however, a big difference was noticed in the value of k and ε themselves when switching to a second order scheme, as shown from Figures 4.18 and 4.19.

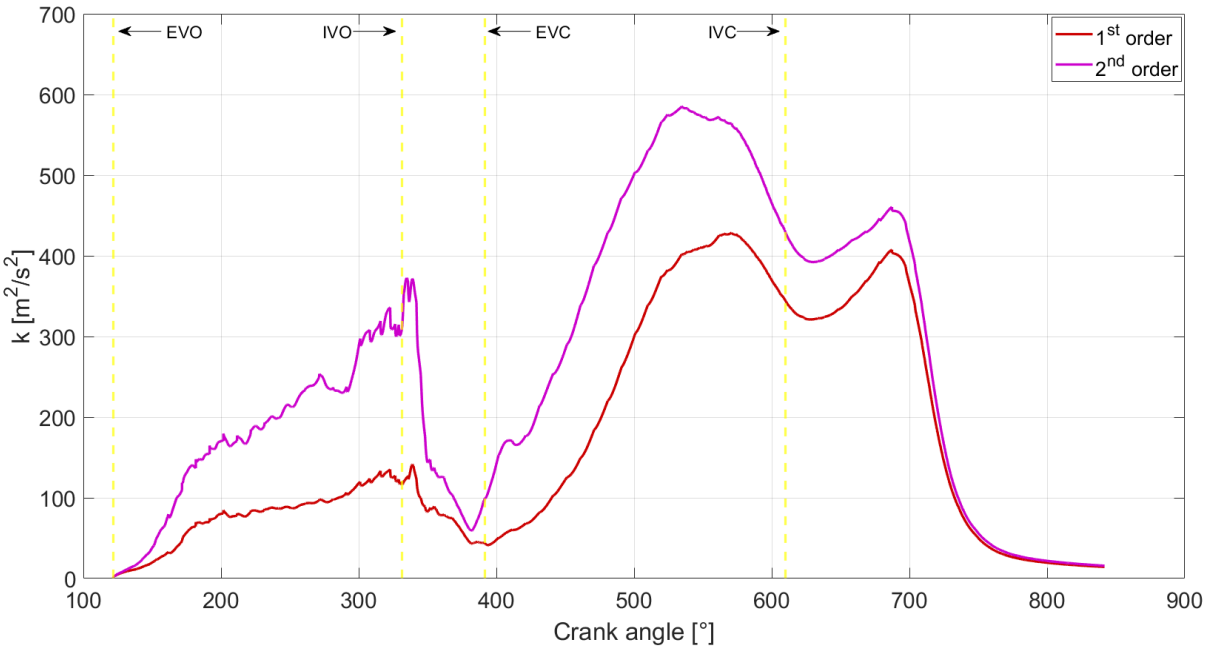

Figure 4.18: Turbulent kinetic energy in cylinder: 1st and 2nd order schemes

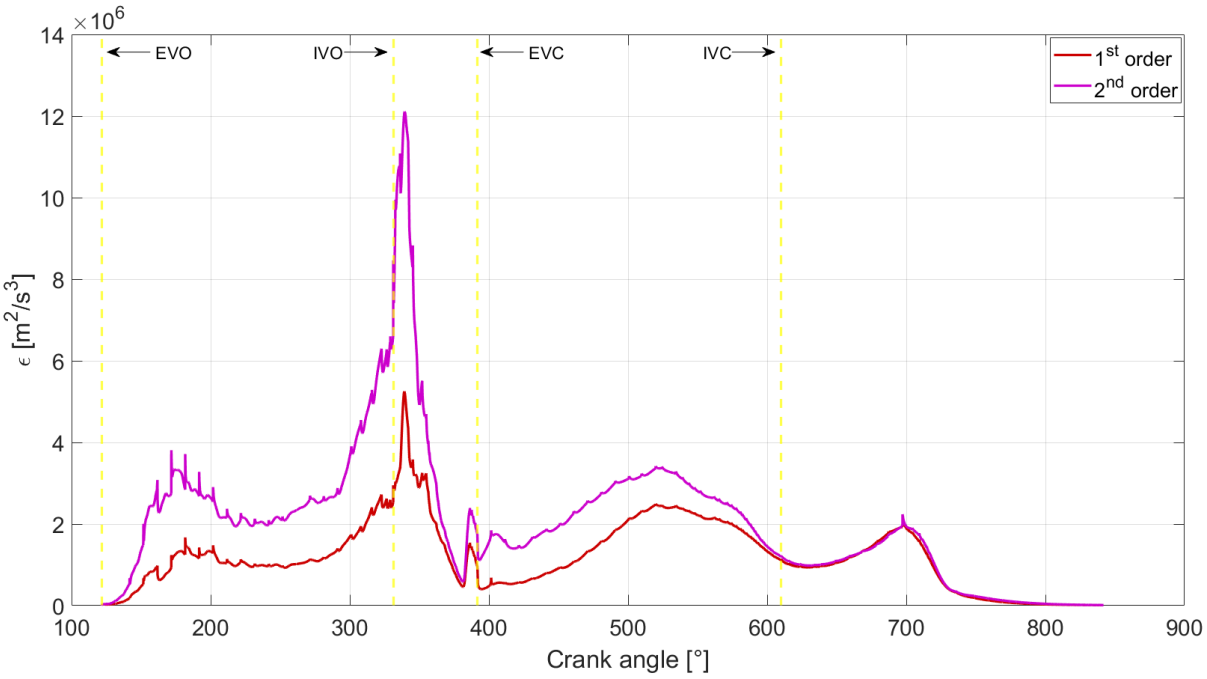

Figure 4.19: Turbulent dissipation rate in cylinder: 1st and 2nd order schemes

To establish which of the two schemes produces results closer to the real flow behaviour, an investigation based on semi-empirical rules was done. The analysis was based on the consideration that the equivalent fluctuating component of the velocity U' is usually in the range of 5-15% of the average velocity $\overline{U}$ in a certain section considering a highly turbulent flow (Re » 4000). By means of the correlation between the equivalent fluctuating component of the velocity and the turbulent kinetic energy, a rough estimation of U' can be obtained. To understand which of the two schemes produces the most realistic results, the turbulence characteristics were analyzed in two points, close to the peaks of the turbulent kinetic energy value during the exhaust and intake phases. The procedure is illustrated by the following formulas, starting from the estimation of U' through the value of k coming from the simulations and then calculating the corresponding turbulence intensity based on an approximated value of average velocity in cylinder. Finally, the calculated value of I is compared to $I_{reference}$, to have a first understanding of the reliability of the results.

$$U' = \sqrt{\frac{2}{3}k} \qquad \Longrightarrow \qquad I = \frac{U'}{\overline{U}}\,; \qquad I_{reference} \approx 0.05 - 0.15$$

At a crank angle equal to 300°, the value of k coming from the simulation with a first order scheme for the discretization of the divergence terms of the turbulence quantities is approximately 115 m^2/s^2, whereas it is approximately 300 m^2/s^2 for the case with a

second order scheme, as can be noticed from Figure 4.18. Analyzing the flow velocity in cylinder by visualizing the simulation results by means of the ParaView software, an estimated mean velocity of around 60 m/s can be considered. Replacing the previously mentioned data in the above formulas, those lead to a value of turbulence intensity of 14.5% for the first order scheme and 23.5% for the second order scheme, thus already giving a clear indication about the overestimation of k produced by the use of a second order scheme. Another point was analyzed, at 550°, leading to the same conclusion: $I = 16.5\%$ for first order scheme and $I = 19.5\%$ for second order scheme, considering a mean velocity of 100 m/s.
Therefore, it was decided to keep using a first order scheme for the discretization of the divergence terms in the k and ε equations, since the second order scheme proved to be physically unsuitable to compute the value of the turbulent kinetic energy, showing a clear overestimation.

In light of the results previously described and based on the highest level of accuracy achievable without losing simulation stability, the final chosen numerical setup for the discretization of the divergence terms was the following:

```
divSchemes
{

    default none;

    div(phiU,p)                             Gauss limitedLinear 0.1;
    div(phi,U)                              Gauss limitedLinear 0.1;
    div(phi,Yi_h)                           Gauss limitedLinear 0.1;
    div(phid,p)                             Gauss limitedLinear 0.1;

    div(phi,k)                              Gauss upwind;
    div(phi,epsilon)                        Gauss upwind;

    div(phi,K)                              Gauss limitedLinear 0.1;
    div(meshPhi,p)                          Gauss limitedLinear 0.1;

    div(((rho*nuEff)*dev2(T(grad(U)))))     Gauss linear;
    div(U)                                  Gauss linear;
    div(facMeshPhi,oneSolve)                Gauss linear;

}
```

Figure 4.20: Divergence schemes final setup

5 | Cold-flow simulation results: cylinder and pre-chamber analysis

In this chapter will be presented in detail the cold-flow simulation results obtained with the best numerical setup, compared to the curves made available by Marmotors s.r.l. coming from experimental tests and 1D simulations of a fired cycle. The reference pressure traces in cylinder and pre-chamber were found by means of sensors placed in the engine on the test bench, whereas the curves of temperature in cylinder and pre-chamber were obtained from 1D simulations performed with the GT-Power software. The value of mass trapped in the engine refers to the mixture of air and fuel and was found during the experimental tests, based on the value of fuel mass injected according to the engine ECU (Electronic Control Unit) and the value of λ.
As it will be seen shortly, the initial results showed a value of simulated mass trapped different from the experimental value. Since it was decided to consider the value of mass trapped as the target parameter, some modifications to the initial and boundary conditions were applied to produce a different simulation outcome, to ensure a good matching between the simulated and the experimental value of mass trapped.

This thesis work was mainly focused on the cold-flow simulation, in order to clarify all the uncertainties emerged by looking at the preliminary simulation results, critically analyzing the data coming from the various sources (i.e. experiments, 1D and 3D simulations). This is important to be sure about the robustness of the numerical setup, allowing to obtain reliable results which are the foundations for the following CFD simulation also including combustion. By starting from trustworthy outcomes of the gas exchange analysis, also the results obtained from the power-cycle simulation can be considered as sufficiently reliable and predictive of the real flow behaviour, keeping in mind that they will be affected also by the combustion modelling strategy.

Thanks to some modifications to the original code of the LibICE library it was possible to plot the desired quantities inside both the main chamber and the pre-chamber, as will be seen in the following sections.

Tuning of initial and boundary conditions

After a proper tuning of all the simulation setup parameters, the first results showed a value of mass trapped calculated by the simulation which was underestimating the experimental value at the EVO and overestimating it at the IVC. This fact can be seen in Figure 5.1, where the curve of the total mass trapped (i.e. sum of mass in cylinder and mass in pre-chamber) is depicted.

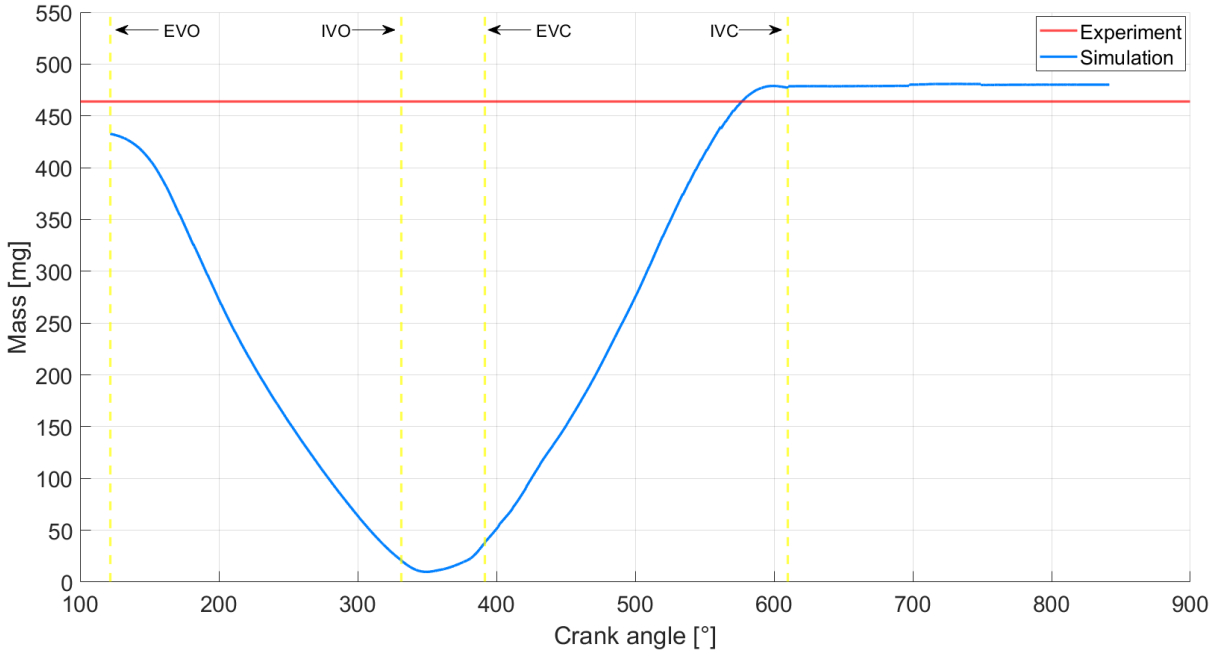

Figure 5.1: Total mass trapped in the engine

The simulated value of mass trapped differs from the experimental value of -6.7% at EVO and +3.2% at IVC, which is not acceptable, therefore some corrections must be applied. The idea behind the modifications introduced is based on the assumption that the experimental data are the most reliable ones, whereas the data coming from the 1D simulation are considered to be more susceptible to errors. For this reason, the value of mass trapped found experimentally is assumed to be correct and taken as a reference to be matched by the simulation. Moreover, the initial conditions in cylinder and pre-chamber for the simulation start at EVO were set by imposing the pressure values found experimentally and

the temperature values found by the 1D simulation. According to the previous assumption, the pressure values are considered as reasonably reliable, hence only the temperature values at EVO were modified.
The initial temperature value in cylinder was reduced of 6.7% to obtain the desired match of the mass trapped value calculated by the simulation with the experimental value. For consistency, also the initial temperature value in pre-chamber was reduced of the same percentage, even if it has a negligible effect on the total mass trapped, being the value of mass trapped in pre-chamber at EVO two orders of magnitude lower compared to the mass trapped in cylinder.
After the reduction of the initial temperature, the mass trapped curve became the following:

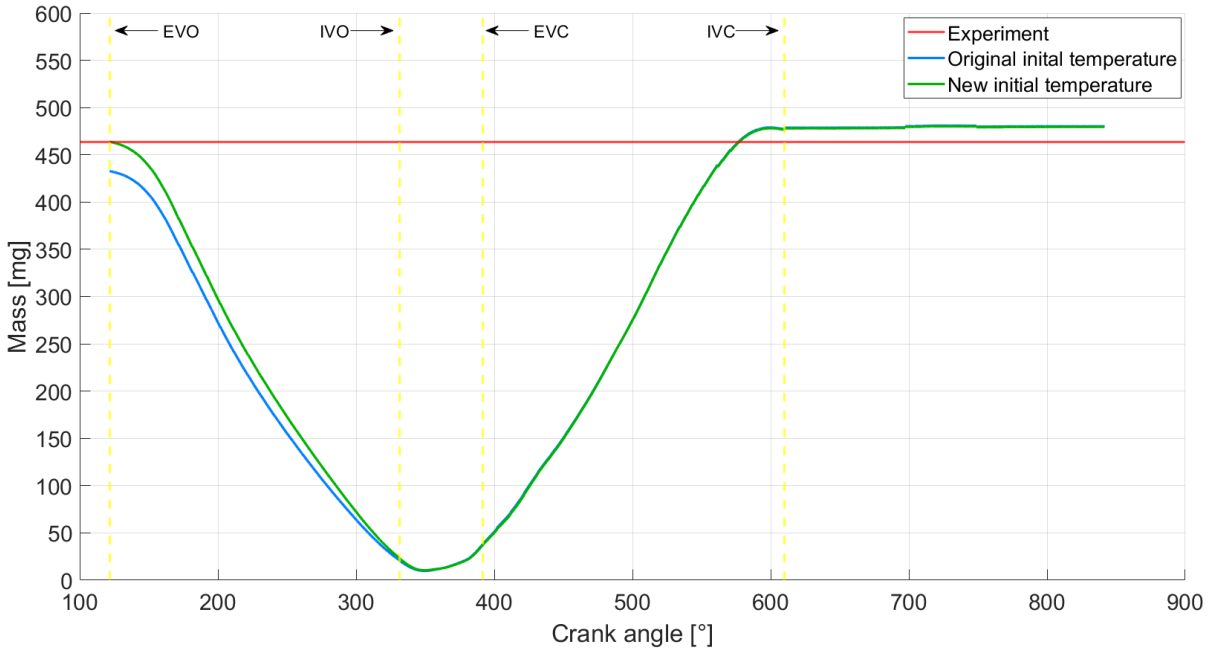

Figure 5.2: Total mass trapped in the engine: new initial temperature

As it can be noticed from Figure 5.2, the variation of the initial value of mass trapped does not significantly affect the exhaust phase, resulting in almost the same values of minimum mass during the overlap phase and mass trapped at IVC (i.e. difference « 1%). At this point, the simulated value of mass trapped at EVO is correct, but there still is not a good matching at IVC. It was noticed that the values of the temperature curve used as boundary condition on the inlet patch of the intake duct, which were also coming from the 1D simulation, were quite low compared to the usual temperature of the air in the intake duct close to the cylinder head, based on common experience. For this reason

it was decided to shift the temperature curve imposed on the inlet patch of the required amount (i.e. +15K) such to obtain the desired value of simulated mass trapped at IVC. Finally, the curve of mass trapped assumes the following shape:

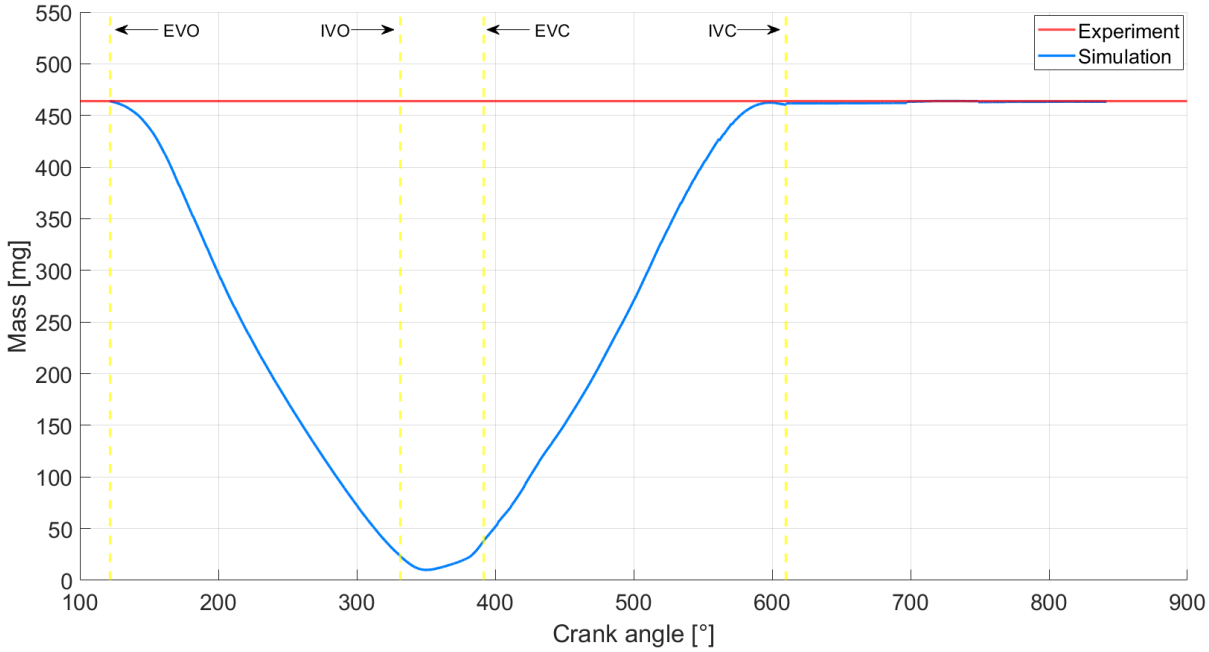

Figure 5.3: Total mass trapped in the engine: new temperature boundary condition

The difference between experimental and simulated mass trapped value at IVC is now less than 1%, therefore considered as acceptable. The initial and boundary conditions are now defined and all the graphs that will be shown in the following sections were obtained by using this modified setup.

5.1. Pressure

Main chamber

The pressure curve in cylinder obtained by the simulation is shown in Figure 5.4 for the full cycle and in Figure 5.5 where a zoom for each relevant phase is depicted.

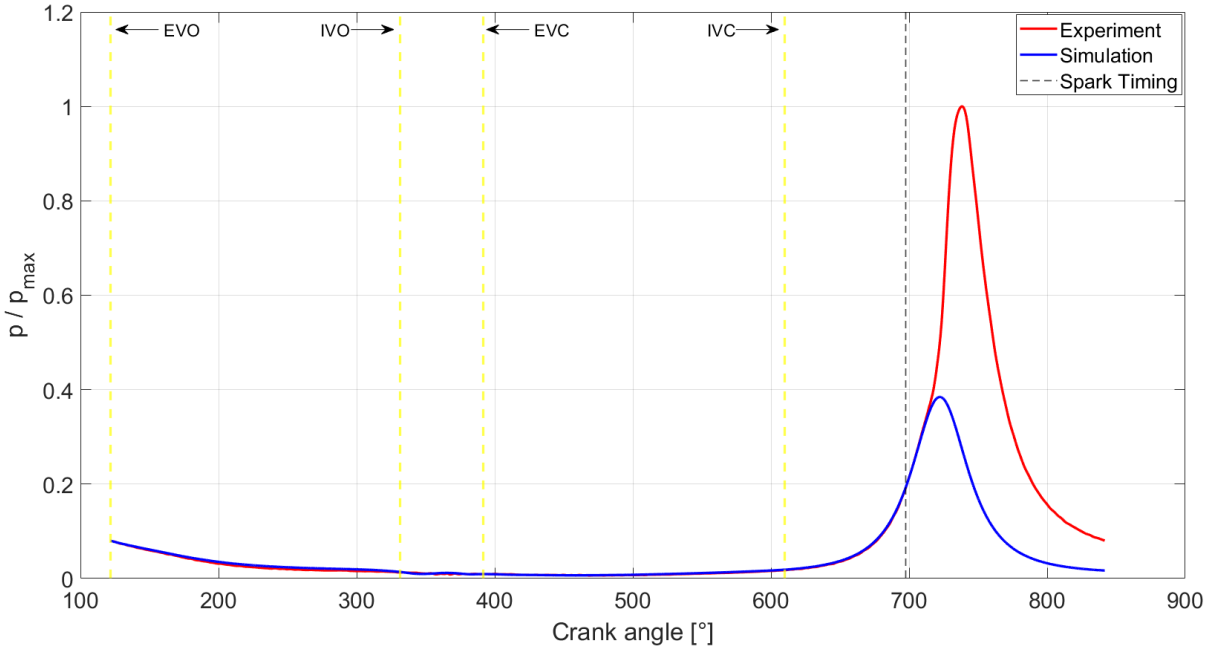

Figure 5.4: Pressure in cylinder

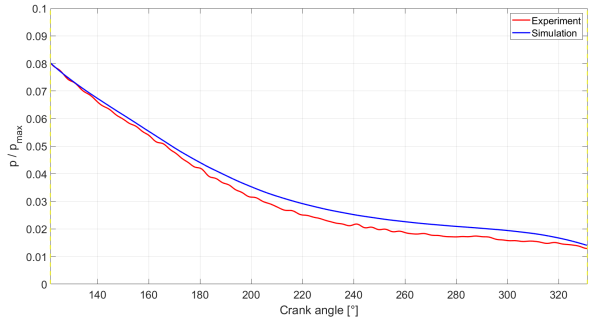

(a) Exhaust

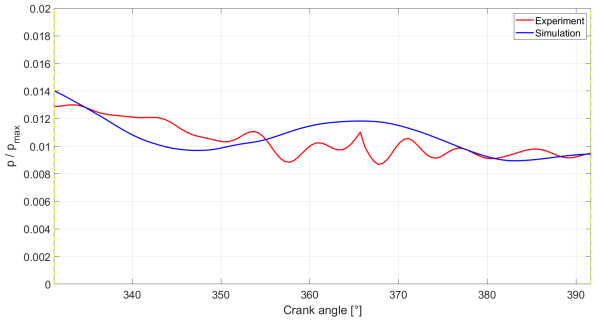

(b) Overlap

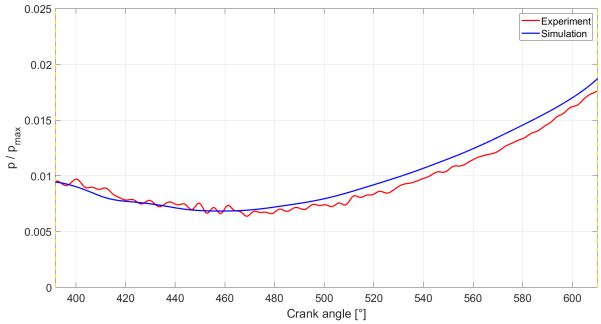

(c) Intake

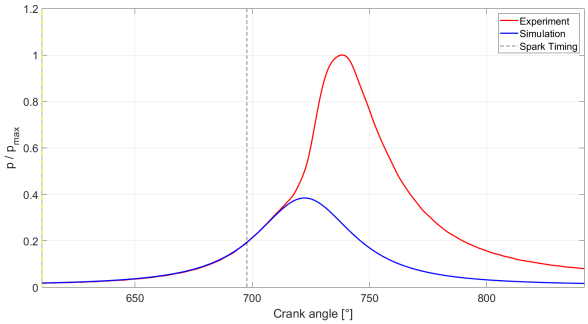

(d) Compression and expansion

Figure 5.5: Pressure in cylinder: engine phases

The results are satisfactory, since the simulated pressure curve in cylinder follows a trend very similar to the experimental pressure trace, with some slight over-estimations during the exhaust and intake phases. These differences might be caused by the boundary conditions imposed at the inlet and outlet patches that are coming from the 1D simulation, so they might not exactly correspond to the real conditions inside the ducts of the engine on the test bench. There are uncertainties also about the wall temperatures imposed for the simulation, since the data about the temperature of each solid surface in the real engine are not known.

5.1.1. Polytropic index investigation

A deeper analysis of the compression stroke on the p-V chart was carried out, to compare the results obtained by the simulation with the compression curve resulting from the in-cylinder pressure measurements of the actual engine.
In the following figures the p-V chart of the simulated and experimental cycles are superimposed in their standard and logarithmic versions.

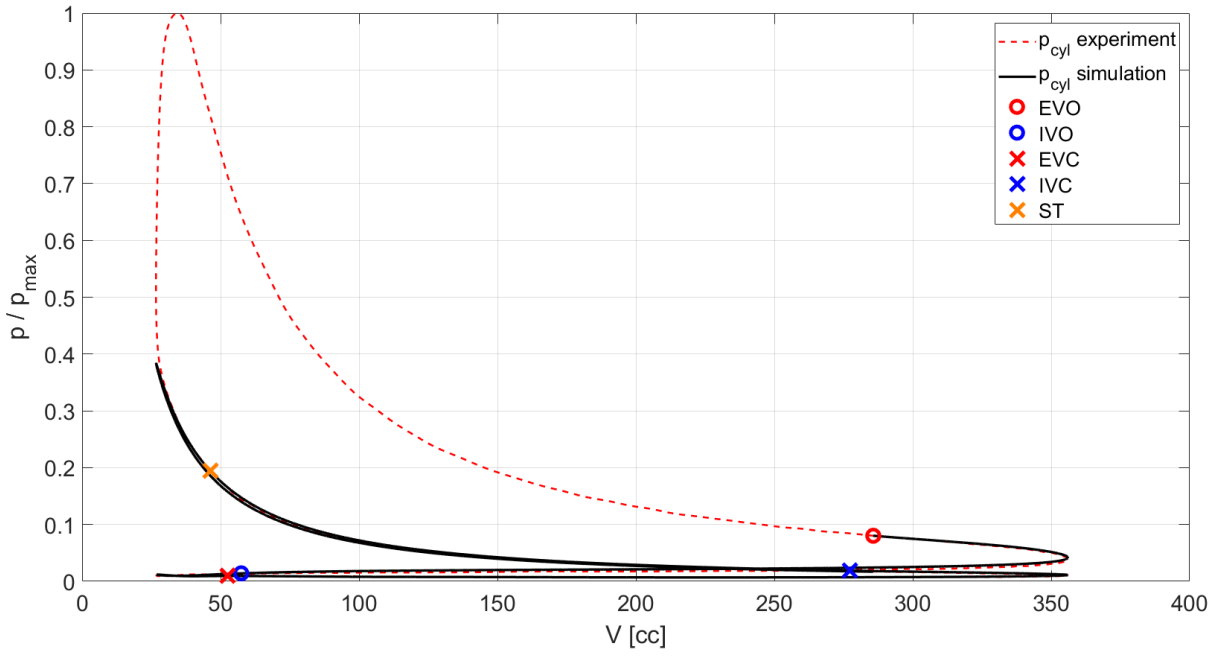

Figure 5.6: p-V chart

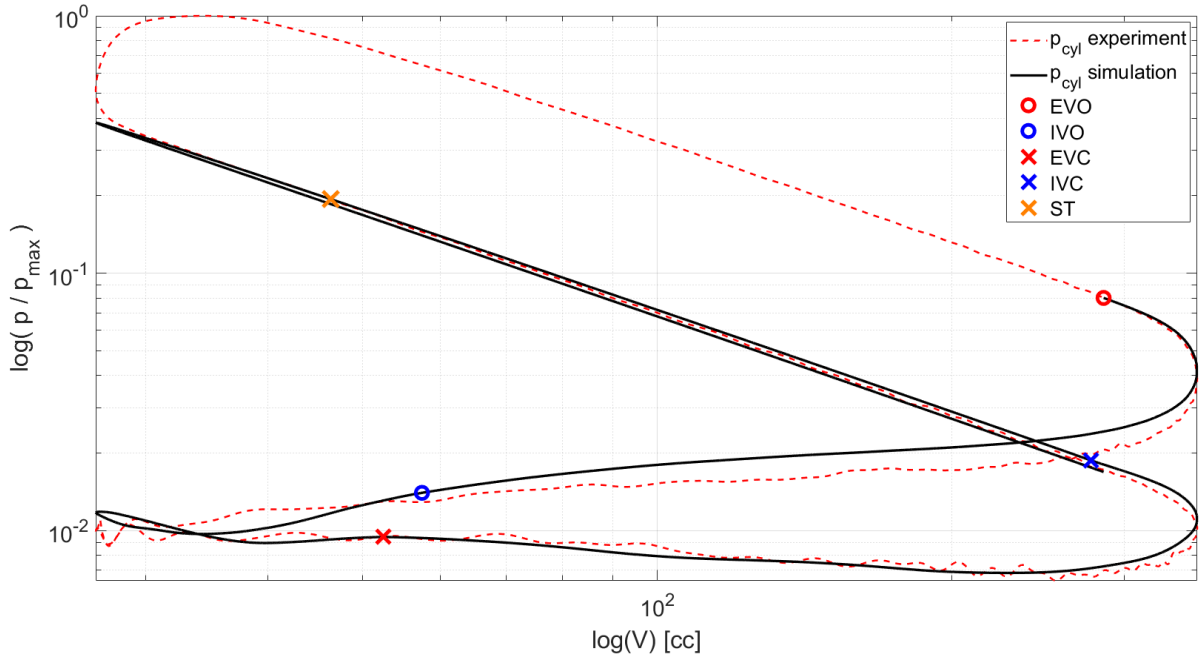

Figure 5.7: Logarithmic p-V chart

It can be noticed from Figure 5.7 that the simulated pressure curve during the compression stroke does not have exactly the same slope of the experimental curve. While it is normal to see a separation between the simulated and the experimental curves after the spark triggering, since for the experimental curve the combustion development causes a rapid temperature increase which in turn leads to a considerable pressure increase, on the other hand the compression curves from IVC to the spark triggering should be overlapped. Therefore, it was decided to perform a deeper investigation on the compression phase of the simulated pressure curve to be sure about the reliability of the simulation results, by analyzing the polytropic index of the gas compression transformation, considering as usual the assumption of ideal gas.

In order to better understand the behaviour of the polytropic index of the simulated compression, the initial step of the polytropic index analysis consisted in plotting the p-V chart together with the compression curves obtained by imposing different polytropic indexes, according to the following formula representing a generic polytropic transformation:

$$pV^n = const \qquad \Longrightarrow \qquad p(CAD) = p_{IVC} \cdot \left(\frac{V_{IVC}}{V(CAD)} \right)^n \tag{5.1}$$

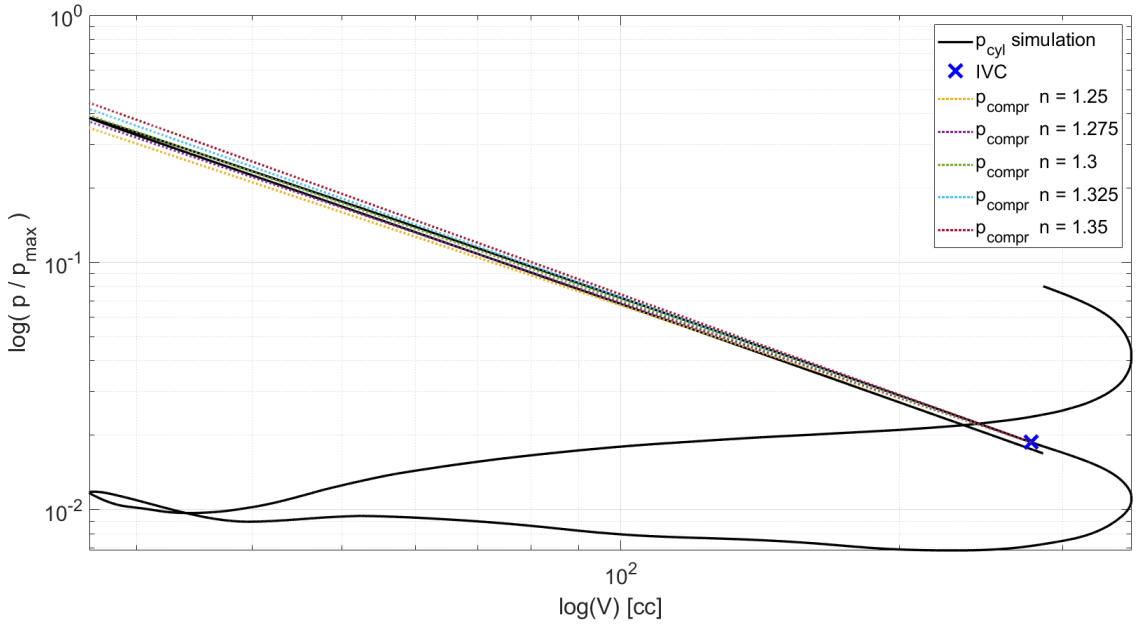

(a) Full engine cycle

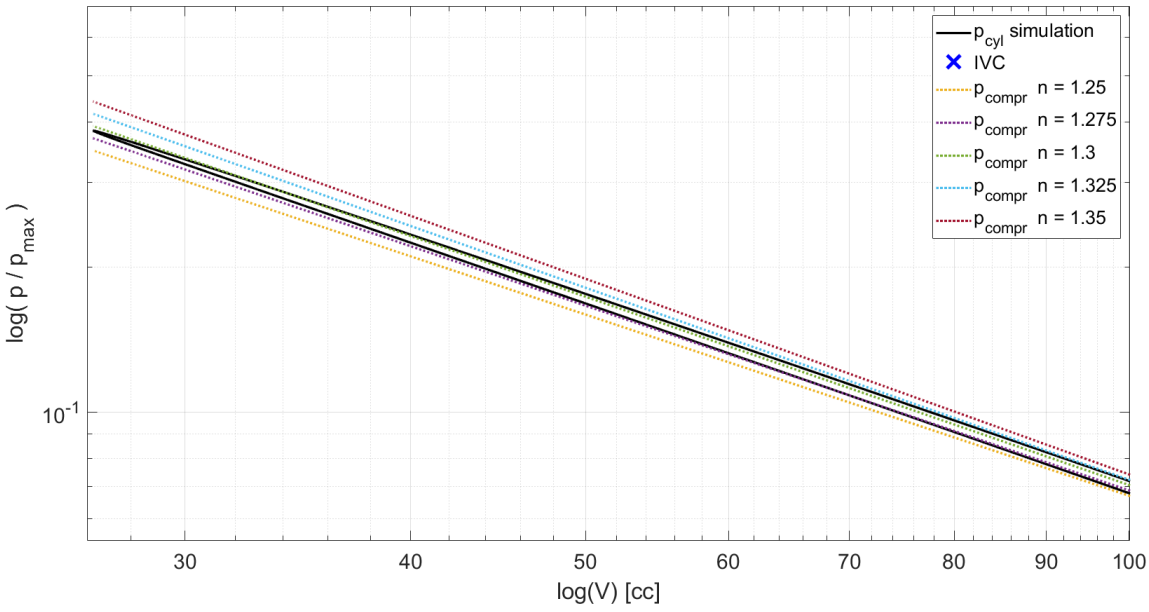

(b) Zoom on the final part of compression stroke

Figure 5.8: Logarithmic p-V chart: polytropic index comparison

From Figure 5.8 it can be clearly seen that the simulated curve has a descending trend, starting from a polytropic index between 1.325 and 1.35 and decreasing to a value lower than 1.3 while the piston moves towards the TDC.
This decline is caused by two contributions:

- Ratio of specific heats: the polytropic index n is usually slightly lower compared to the index of an isoentropic transformation ($\gamma = \frac{c_p}{c_v}$), due to the entropy generation that characterises a real transformation. For an ideal gas, the specific heats only depend on the gas temperature ($c_p = c_p(T), c_v = c_v(T)$), and the ratio of specific heats γ tends to decrease when the gas temperature increases. As a consequence, the polytropic index n undergoes the same behaviour. Since during the compression stroke the gas temperature increases because of the higher gas pressure caused by the volume reduction, it is normal for the polytropic index to decrease when the piston moves towards the TDC compressing the gas.
- Heat transfer through cylinder walls: it can be deduced from equation 5.1 and from the ideal gas law that the polytropic index n is equal to 1 in the case of isothermal transformation. For a compression, where the gas temperature naturally increases, the isothermal transformation would be achieved by subtracting from the gas the exact amount of heat introduced by the compression. In more general terms, a real compression tends to an isothermal transformation the more heat is rejected by the gas towards an external source. Since the temperature of the cylinder walls is imposed as fixed and is lower than the gas temperature for most of the compression stroke, the more the temperature of the gas increases during the compression phase, the greater is the heat transfer between the gas and the colder cylinder walls, thus causing a further decrease of the polytropic index (i.e. the gas transformation is tending more towards an isothermal transformation, thus the polytropic index is tending more towards 1).

To prove the above sentences, a simulation of the only compression phase was performed, by imposing for all the surfaces in contact with the main chamber and the pre-chamber to be adiabatic, thus nullifying the heat transfer between gas and cylinder walls.
The results can be seen from the following graphs, from which it can be noticed that there still is a descending trend for the polytropic index of the compression caused by the gas temperature increase, but this index reduction is less sharp especially in the final part of the compression stroke, since the cylinder walls in this simulation were adiabatic and therefore the second contribution related to heat transfer, that for a real transformation causes a further decrease of the polytropic index, is not present.

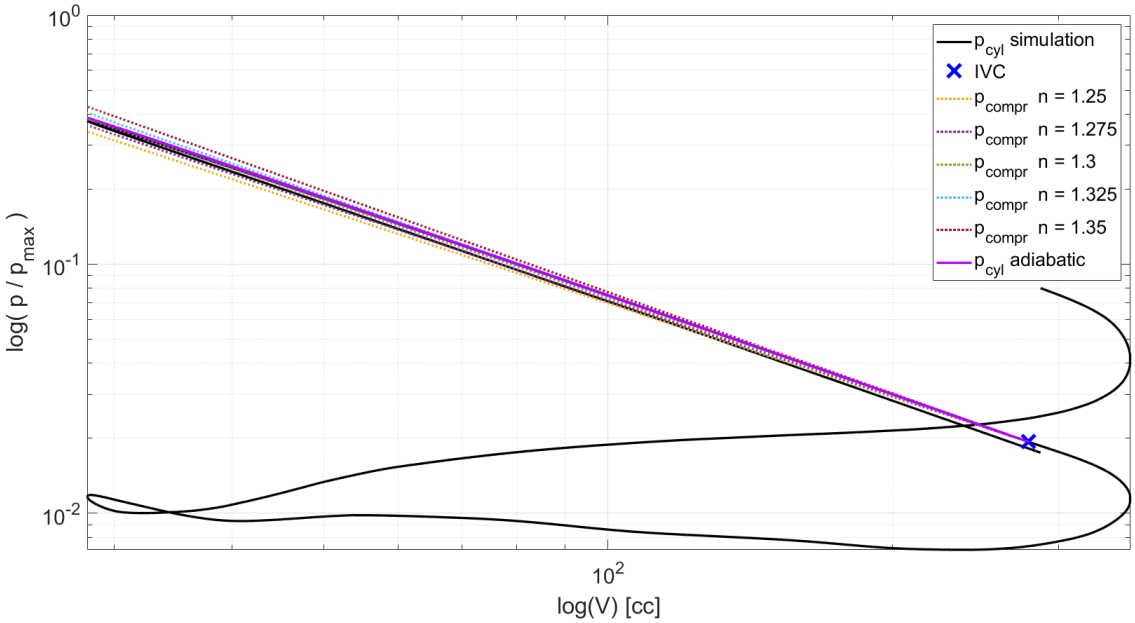

(a) Full engine cycle

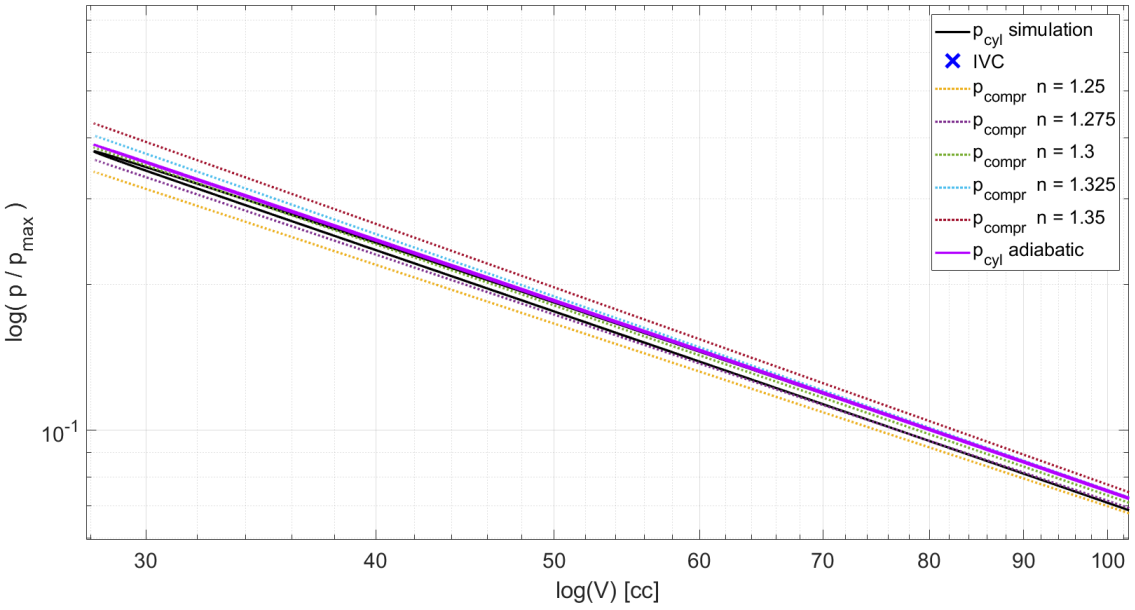

(b) Zoom on the final part of compression stroke

Figure 5.9: Logarithmic p-V chart: comparison with adiabatic compression

The adiabatic walls cause a higher average value of the polytropic index, as it can be clearly seen from the final part of compression illustrated in Figure 5.9b, which is the part of the compression phase where the heat transfer usually has the greatest influence because of the higher temperature difference between gas and cylinder walls. It can be also

noticed that, since no heat rejection is present, a slightly higher pressure peak is reached at TDC because of the higher gas temperature. For the same reason, the pressure curve of the compression and expansion phases are perfectly overlapped for the adiabatic case, while in the real condition the pressure curve during the expansion stroke is always slightly lower than during the compression stroke.

As already mentioned, since a slight difference of the slope of the compression curves on the p-V chart in Figure 5.7 was noticed, the same analysis on the polytropic index evolution was performed also on the experimental pressure curve, which showed an average value of the polytropic index constantly slightly higher compared to the simulation results.
Eventually, it was concluded that the simulation results show a physically realistic behaviour, therefore the differences of the polytropic index trend between simulated and experimental pressure curves were attributed to the small difference of gas pressure at IVC between the two curves and to the uncertainties affecting the experimental pressure trace, such as the sensor tolerance, the post-processing of the signal performed to find a unique curve to be taken as a reference, neglecting the inherent cyclic variability between each engine cycle, and also the uncertainty about the exact compression ratio of the tested engine, which in the worst case scenario might be even 0.5 points different from the simulated engine.

Pre-chamber

The pressure curve in pre-chamber obtained by the simulation is shown in Figure 5.10 for the full cycle and in Figure 5.11 where a zoom for each relevant phase is depicted.

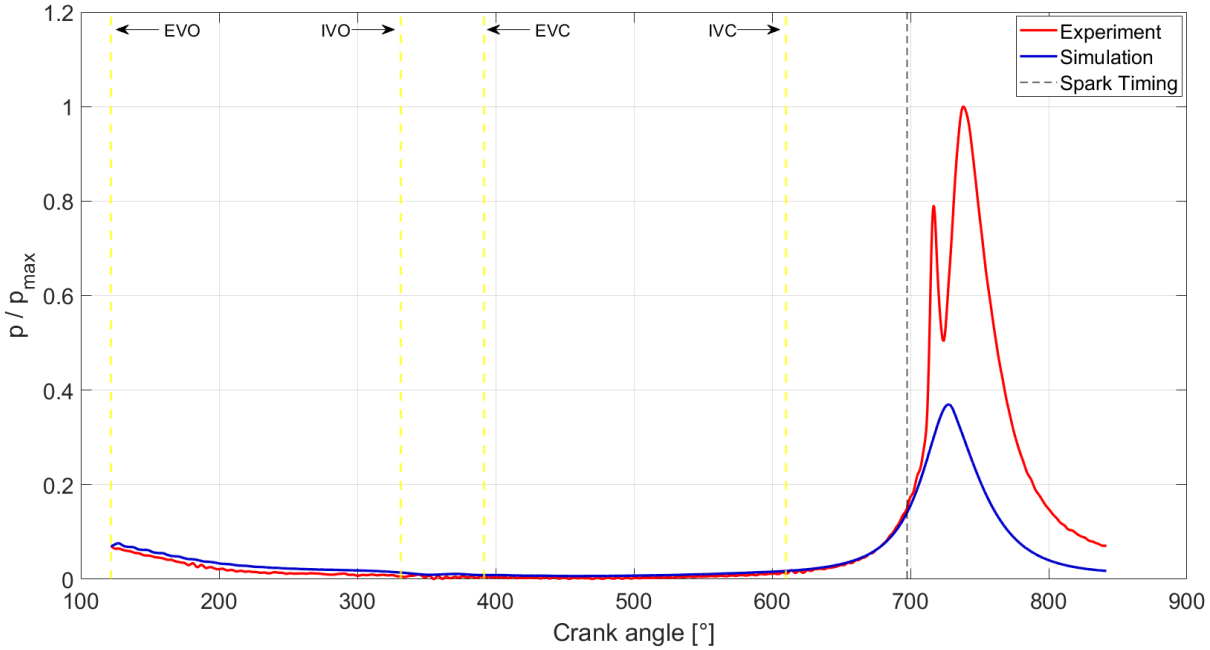

Figure 5.10: Pressure in pre-chamber

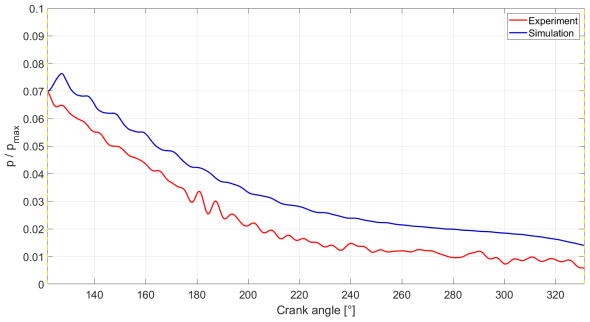

(a) Exhaust

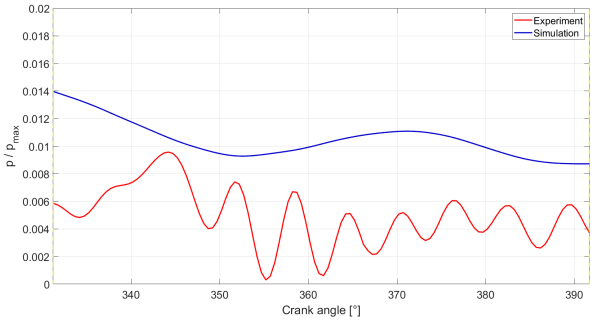

(b) Overlap

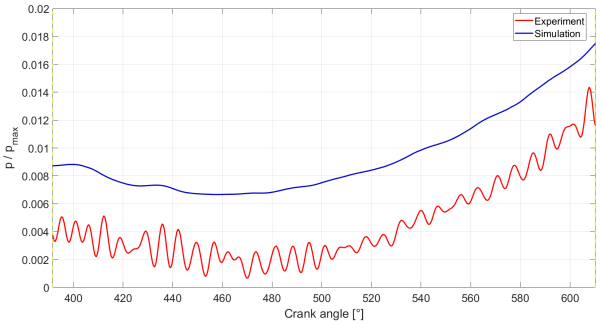

(c) Intake

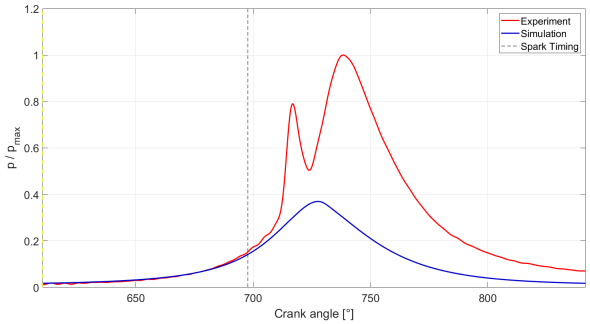

(d) Compression and expansion

Figure 5.11: Pressure in pre-chamber: engine phases

The simulation results generally show a pressure in pre-chamber constantly higher compared to the experimental results, as it can be seen from the exhaust, overlap and intake phases in Figure 5.11.
This issue was attributed to a measurement error of the pressure sensor integrated in the spark plug, which had different characteristics compared to the in-cylinder pressure sensor and returned pressure values which were usually too low to be realistic, in particular when the value of pressure to be measured was much lower compared to the maximum limit value of pressure that can be measured by the sensor, as it is in the above mentioned engine phases.

To be thorough, below is reported an additional figure where the experimental and simulated curves of both main chamber and pre-chamber are plotted together during the compression and expansion strokes.

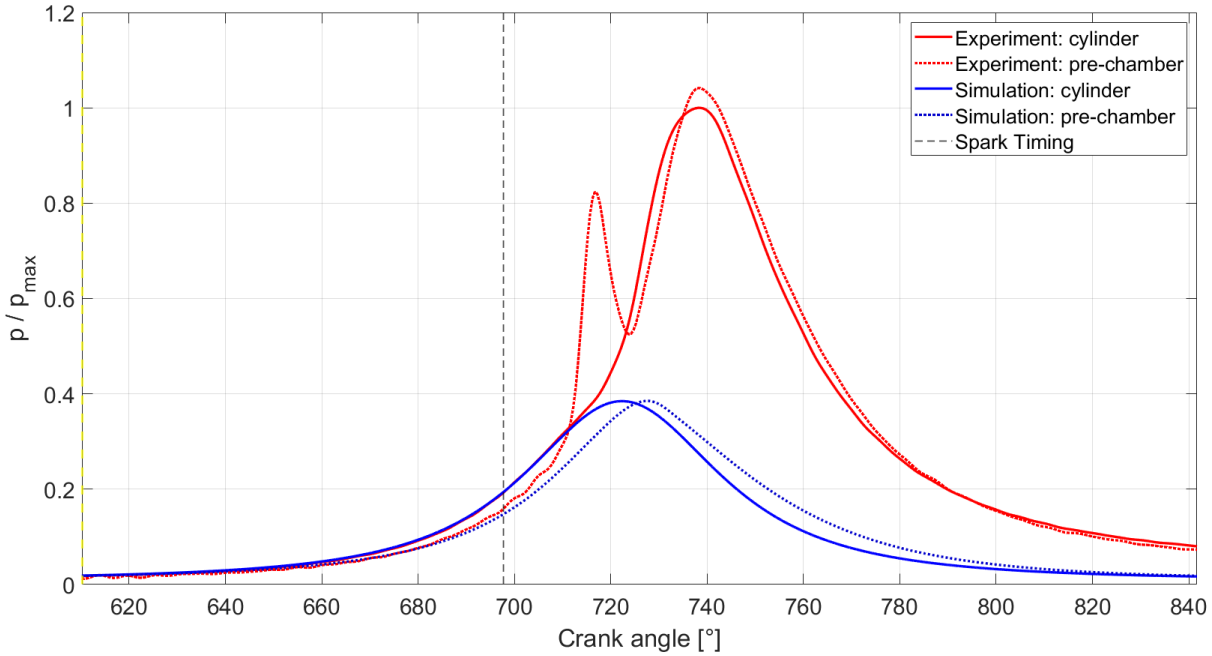

Figure 5.12: Pressure in cylinder and pre-chamber

From Figure 5.12 it can be noticed that the pressure peak in cylinder is reached few CAD after 720°. This is caused by the fact the engine is characterised by a certain pin offset, therefore the TDC is achieved after the position of vertical crank.
The pressure peak values in cylinder and pre-chamber of the simulated engine motoring cycle are very similar, with a delay in time caused by the fact that the pre-chamber is at a greater height on the cylinder head and by the pressure drop to which the gas is subjected

when flowing from cylinder to pre-chamber through the orifices. Actually, by looking more in detail, the pre-chamber pressure peak is slightly higher than the in-cylinder pressure peak. This aspect is not of immediate understanding, since one would expect the pressure peak in pre-chamber to be lower than the pressure peak in cylinder, considering the previously mentioned pressure drop to which the flow is subjected. However, it has to be considered that the average gas temperature in pre-chamber is higher compared to the gas temperature in cylinder (as will be shown in the following section), because of the higher temperature of the pre-chamber walls (see table 4.4 in section 4.2), which tend to keep the gas more heated during the whole engine cycle. This means that during the compression stroke the gas inside the pre-chamber is at a higher temperature compared to the gas inside the cylinder, hence its compression leads to a higher pressure peak. In conclusion, to understand the difference of the pressure peak value between main chamber and pre-chamber during a motoring cycle, two conflicting aspects must be considered: the higher gas temperature inside the pre-chamber that would lead to a higher pressure peak and the pressure drop caused by the flow passage through the pre-chamber orifices that would lead to a lower pressure peak. Based on which on these two facts is prevailing, the pressure peak in pre-chamber will be higher or lower compared to the pressure peak in cylinder, but always delayed. In this particular case it seems that the two physical phenomena are balancing each other, with a slight prevalence of the higher pre-chamber gas temperature effect.

Another issue was detected looking at Figure 5.12: the experimental pressure curve in pre-chamber coming from a fired cycle detaches from the simulated pressure curve in pre-chamber of the motoring cycle before the spark triggering. This should not happen, since the curves of the fired and motoring cycles must be identical up to the spark timing, and separate only after it due to the pressure increase caused by combustion happening in the fired cycle.
This difference was justified by considering the fact that the pressure curve coming from the simulation is the result of an average of the pressure value over all the cells composing the pre-chamber volume, while the experimental trace comes from a measurement in a specific point of the pre-chamber, which in this case was a point in the top part of it, since the pressure sensor was integrated in the spark plug. Therefore, it might be assumed that in the specific position of the pre-chamber where the sensor was located the pressure is higher compared to the average value. This hypothesis is confirmed by visualizing the results, which show a slightly higher pressure in the upper part of the pre-chamber caused by the lower velocities in that region during the compression phase, as it can be seen from Figure 5.13, where it is shown the pressure field inside the pre-chamber at a crank angle

very close to the spark timing (697.7 CAD). Moreover, the experimental curve is the result of a filtering and averaging procedure over several engine cycles to neglect the effect of the cycle-to-cycle variability characterising every internal combustion engine. However, it can be be noticed from the previous graphs that the experimental pressure trace is characterised by evident oscillations, which are probably caused by a disturbance which was not filtered, thus affecting the quality of the signal.

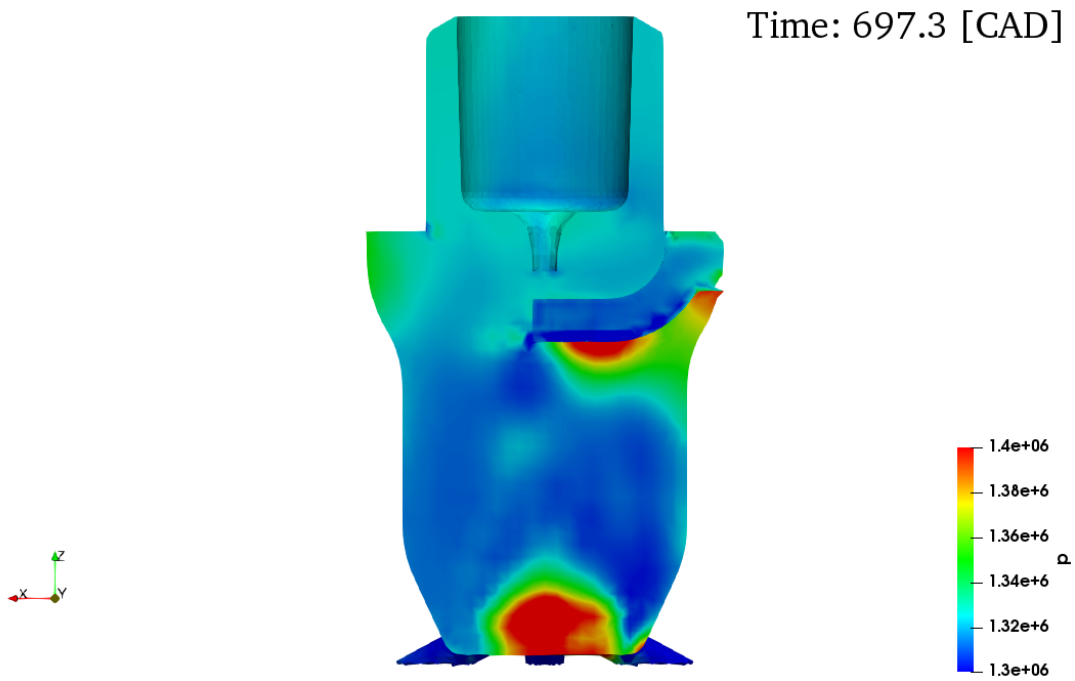

Figure 5.13: Pressure field inside the pre-chamber at 697.3 CAD

5.2. Temperature

Main chamber

The temperature curve in pre-chamber obtained by the simulation is shown in Figure 5.14 for the full cycle and in Figure 5.15 where a zoom for each relevant phase is depicted.

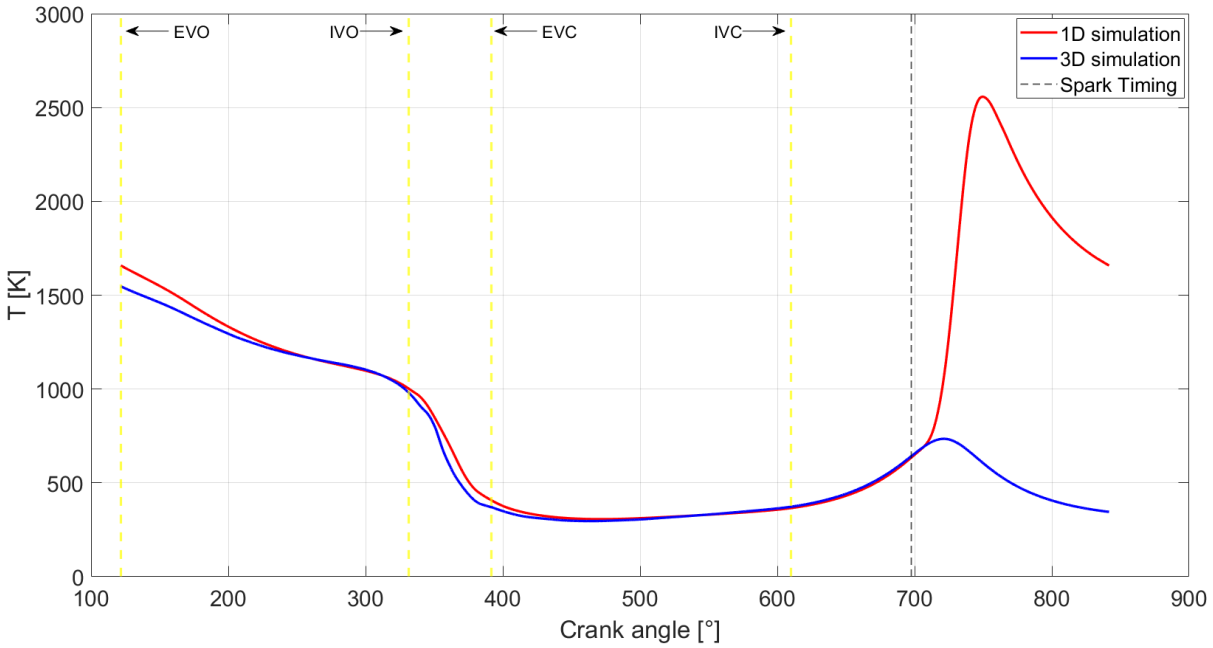

Figure 5.14: Temperature in cylinder

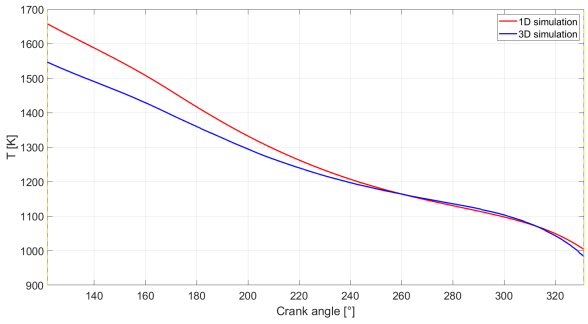

(a) Exhaust

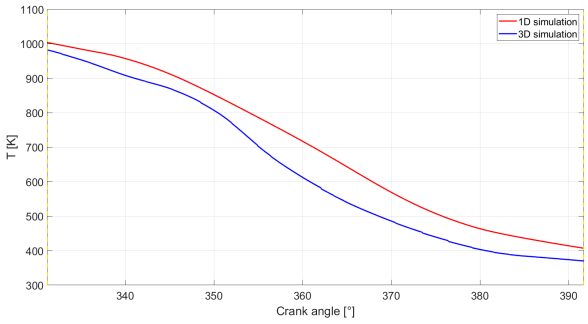

(b) Overlap

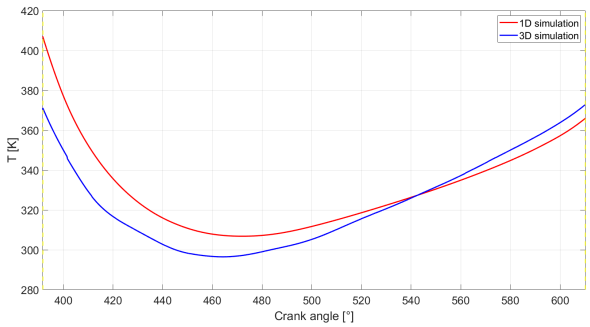

(c) Intake

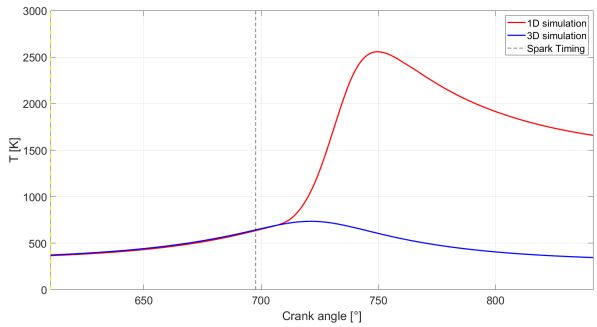

(d) Compression and expansion

Figure 5.15: Temperature in cylinder: engine phases

The simulation results show a temperature trend quite coherent with the reference curve obtained from the 1D simulation, always keeping in mind that the 1D simulation results are affected by more uncertainties compared to the 3D simulation results.
The difference between the starting temperature at EVO of the two simulations is caused by the modification of the initial conditions described at the beginning of this chapter, necessary to have a value of mass trapped at the simulation start equal to the value measured experimentally.

Pre-chamber

The temperature curve in pre-chamber obtained by the simulation is shown in Figure 5.16 for the full cycle and in Figure 5.17 where a zoom for each relevant phase is depicted.

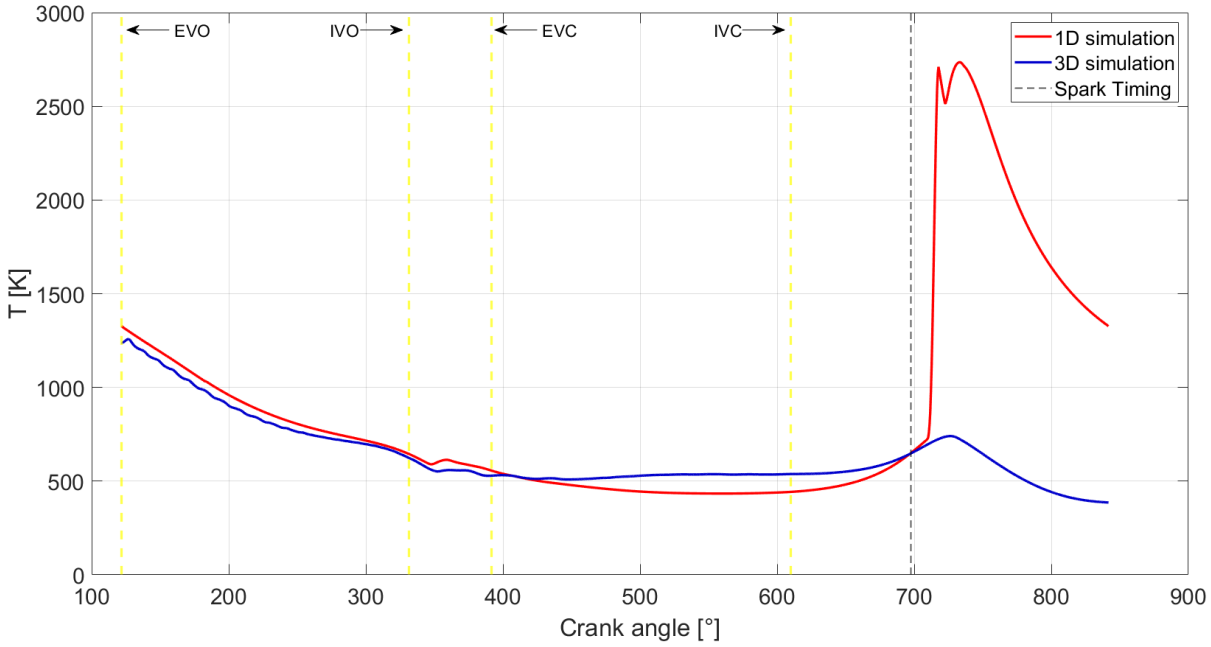

Figure 5.16: Temperature in pre-chamber

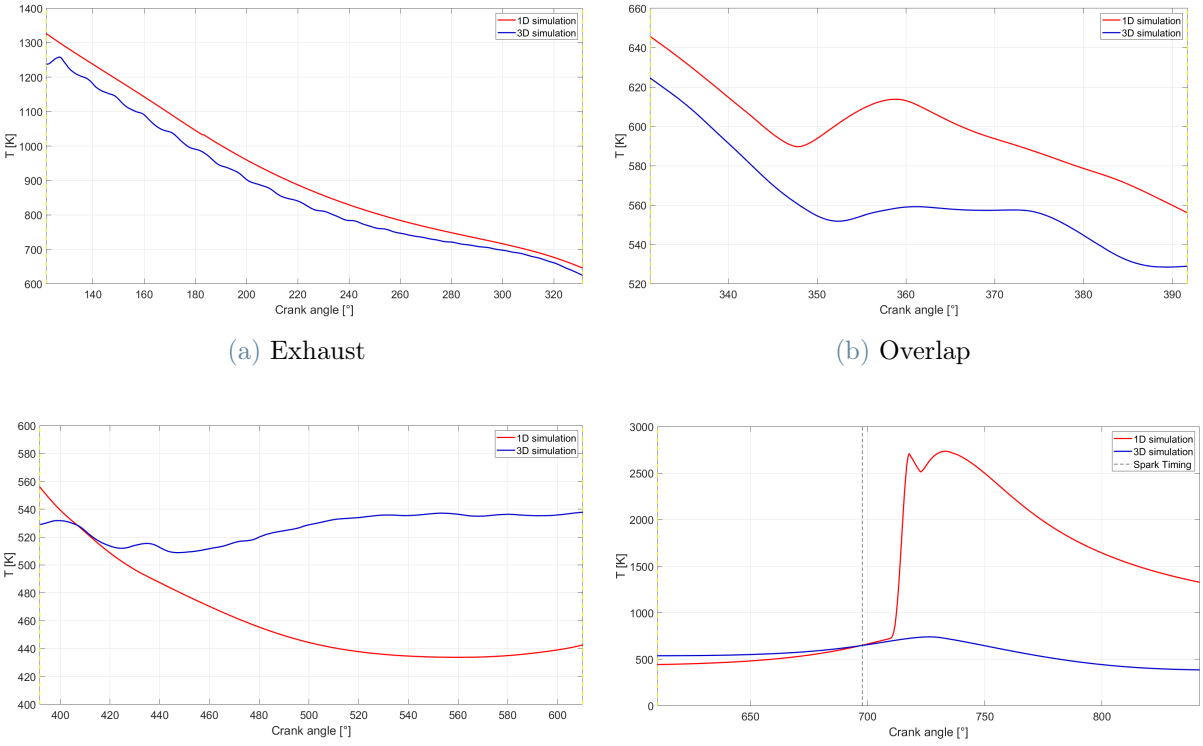

(a) Exhaust

(b) Overlap

(c) Intake

(d) Compression and expansion

Figure 5.17: Temperature in pre-chamber: engine phases

The same considerations done for the temperature curves in the main chamber are valid also for the simulation results in the pre-chamber.
In addition, a noteworthy difference in the temperature trend inside the pre-chamber between the 1D and the 3D curves can be seen during the intake phase illustrated in Figure 5.17c. This diversity is caused by the fact that the pre-chamber walls temperature imposed in the two simulations was not the same. For the 1D simulation the pre-chamber walls temperature was set equal to the cylinder head temperature, whereas for the 3D simulation performed in the present thesis work it was considered to be more reasonable to set a pre-chamber wall temperature higher compared to the cylinder head temperature, being aware of the different material of which these two parts of the engine are made (i.e. the pre-chamber is made of a metal alloy with a much higher thermal conductivity, thus it is subjected to a greater heat rejection causing a higher wall temperature, as already discussed in section 4.2).
In particular, the pre-chamber walls temperature is higher compared to the gas temperature during the intake phase, hence causing the introduction of some heat from the solid surface to the gas, leading to a small temperature increase.

In the following figure, the temperature curves of both main chamber and pre-chamber are plotted together, to give a clearer view about the general trends in these two regions.

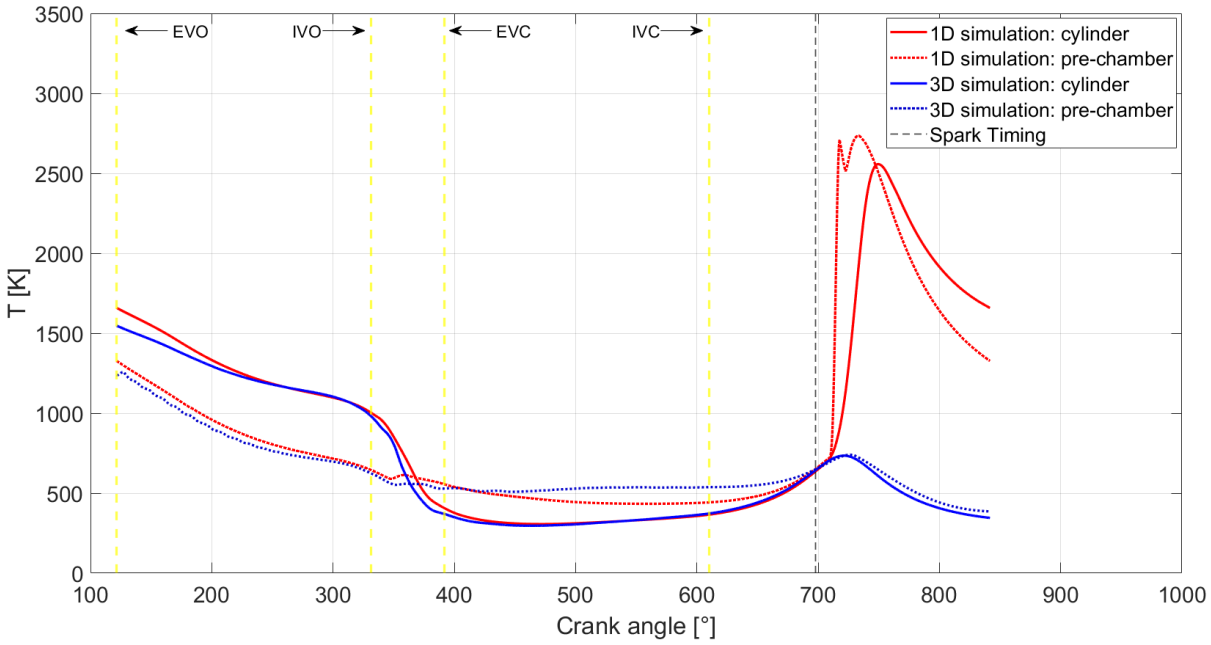

Figure 5.18: Temperature in cylinder and pre-chamber

By looking at Figure 5.18 and comparing the temperature trends during the overlap phase in cylinder and pre-chamber, it can be noticed that a much greater temperature reduction happens inside the main chamber during this phase thanks to the scavenging effect promoted by the burned gas flowing out from the exhaust valve and at the same time dragging in fresh charge from the intake valve, whereas the pre-chamber is much less affected by this gas exchange process because of its inconvenient position up over the cylinder head.

Moreover, during the overlap phase a slope change can be clearly noticed from Figure 5.17b for the pre-chamber temperature curve close to the TDC position. This is probably caused by the piston that while moving upwards pushes a very small amount of mixture at higher temperature from the cylinder to the pre-chamber and compresses the gas already trapped inside the pre-chamber and unable during this phase to easily come out from it and leave space to the fresh mixture.

5.3. Trapped mass

Main chamber

The curve of mass trapped inside the cylinder obtained by the simulation is shown in the following figure.

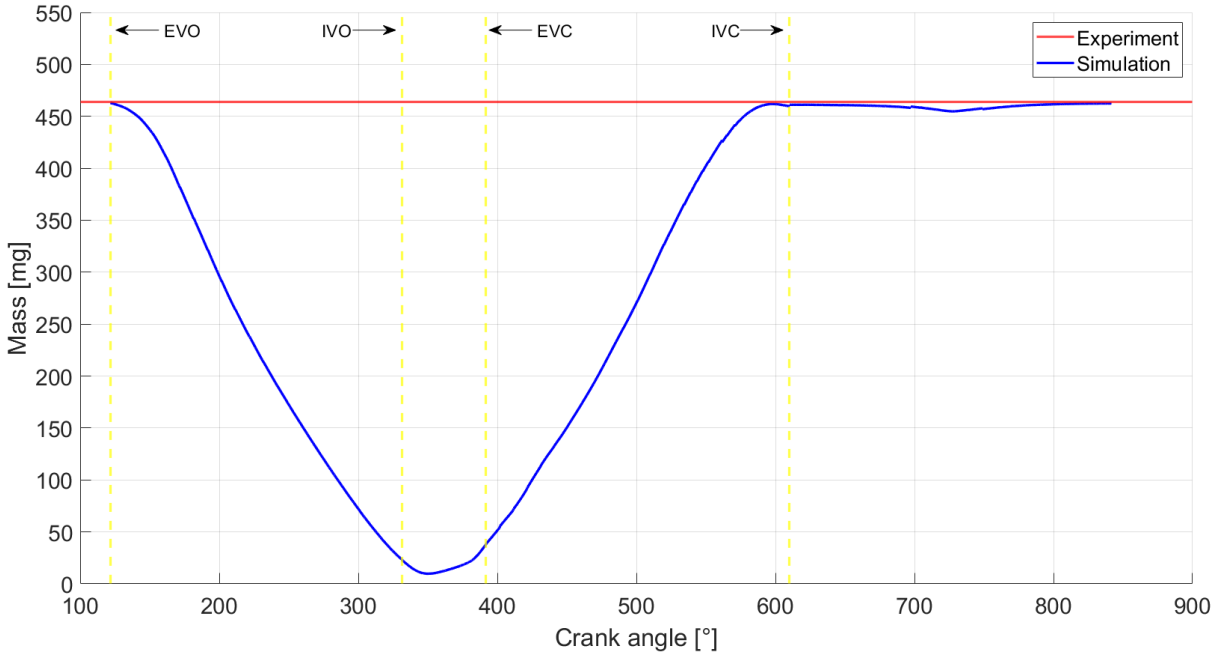

Figure 5.19: Mass trapped in cylinder

A decrease of mass trapped inside the cylinder can be noticed from Figure 5.19 during the compression phase before the TDC, that then increases again after the TDC. This variation is caused by the gas exchange between main chamber and pre-chamber: during the compression stroke part of the gas mass is pushed inside the pre-chamber by the piston motion, then during the expansion stroke the pressure inside the main chamber decreases again, thus generating a pressure gradient pushing back some mass from the pre-chamber to the main chamber.
Before the IVC, a very little backflow of mass from the cylinder to the intake duct can be noticed, indicating that the valve timing was probably optimized for the operative point simulated or a condition very close to it, thus for high engine speed and high load.

Pre-chamber

The curve of mass trapped inside the pre-chamber obtained by the simulation is shown in the following figure.

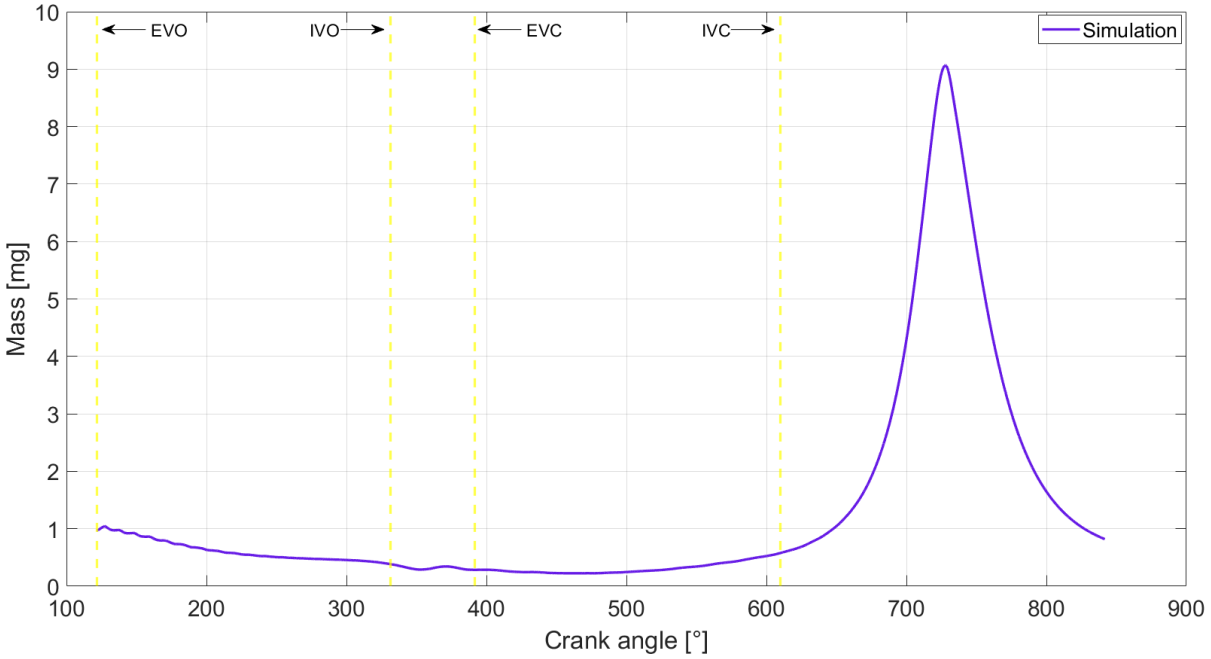

Figure 5.20: Mass trapped in pre-chamber

Figure 5.20 proves that the pre-chamber filling takes place almost only during the compression stroke, thanks to the piston motion pushing fresh mixture inside it. The TDC for this engine is at 722.7 CAD, but the peak of mass trapped is reached at approximately 728 CAD. This happens because of the inertial effect of the gas, that keeps flowing into the pre-chamber even when the piston has already stopped and it is starting to move backwards.
Nevertheless, the value of mass trapped inside the pre-chamber of greatest interest for practical engine operation (i.e. in a fired cycle) is the one reached at the spark timing (i.e. 697.7 CAD), which in this case is less than half the maximum potential value of mass trapped inside the pre-chamber achieved by this simulation of an engine motoring cycle.

In the following picture the curves of mass trapped in cylinder and pre-chamber are plotted together with the curve resulting from their sum, demonstrating that when the valves are close the mass trapped inside the engine remains constant.

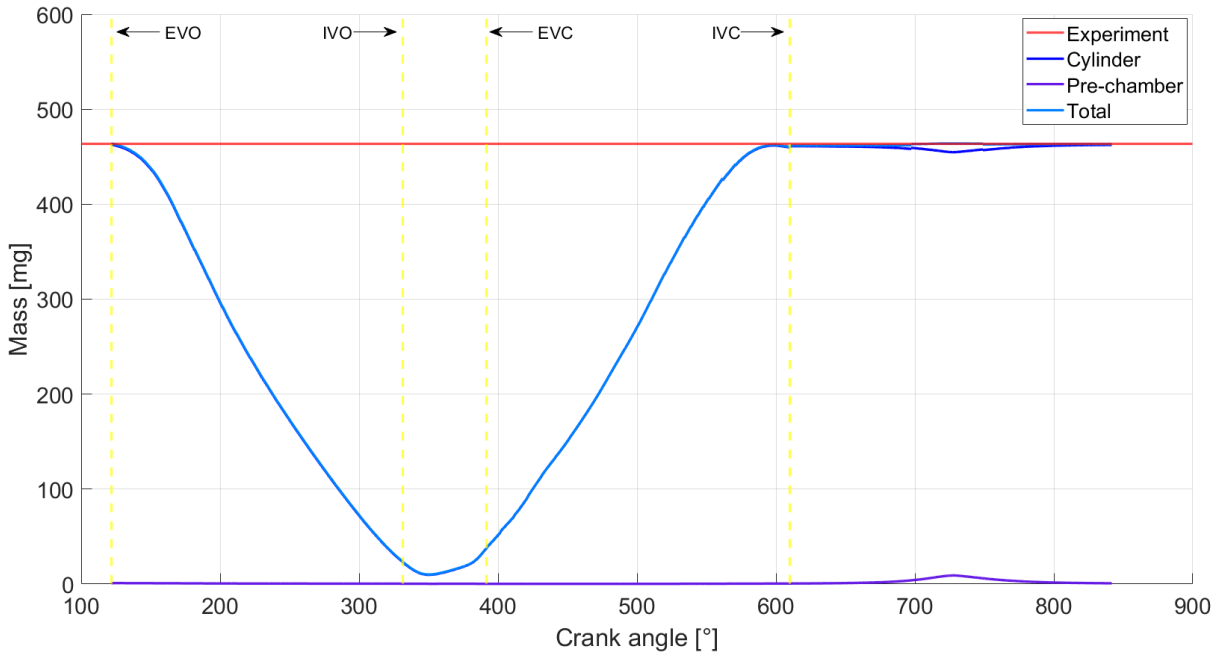

Figure 5.21: Mass trapped inside the engine: cylinder and pre-chamber

5.3.1. Mass fractions and residual gas

The molecular species mass fractions are initialized in the different regions of the engine according to the assumption that an ideal combustion between octane and air composed only by oxygen and nitrogen took place in the engine cycle before the one to be simulated, as already explained in section 4.2.
Burned gas are initialised in exhaust duct, cylinder and pre-chamber with the same concentrations of N_2, CO_2, H_2O and the excess of C_8H_{18}, since for the operative condition simulated the air-fuel ratio is rich. In the intake duct an homogeneous mixture of air and fuel (i.e. N_2, O_2 and C_8H_{18}) is initialised, since the port fuel injection was not simulated.

The following figure shows the trend of the oxygen mass fraction in cylinder and pre-chamber during the full cycle.

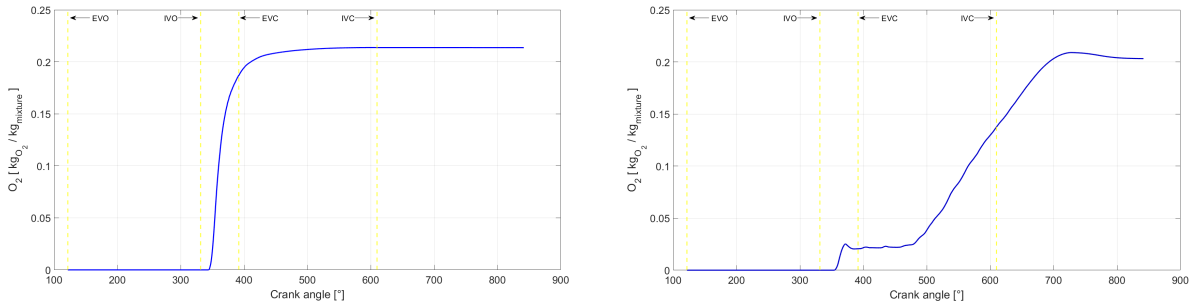

(a) Cylinder (b) Pre-chamber

Figure 5.22: Oxygen mass fractions

As it can be seen from Figure 5.22, the gas exchange process inside the cylinder takes place mainly during the overlap phase, where the burned gases are almost totally replaced by the fresh charge, that then continues to fill the cylinder during the intake stroke. On the other hand, the overlap phase has a negligible influence on the gas exchange process inside the pre-chamber, which begins during the final part of the intake phase (i.e. mainly when the piston starts its upward motion from the BDC) and completes during the compression stroke. However, it is interesting to notice that, even if the burned gas inside the pre-chamber start to be replaced by the fresh mixture during the final part of the intake phase, the mass trapped is still very low until the IVC, when the pre-chamber filling effectively begins. This issue can be clearly seen in the following figure, where the charts of oxygen mass fraction in pre-chamber (Figure 5.22b) and total mass in pre-chamber (Figure 5.20) are plotted together.

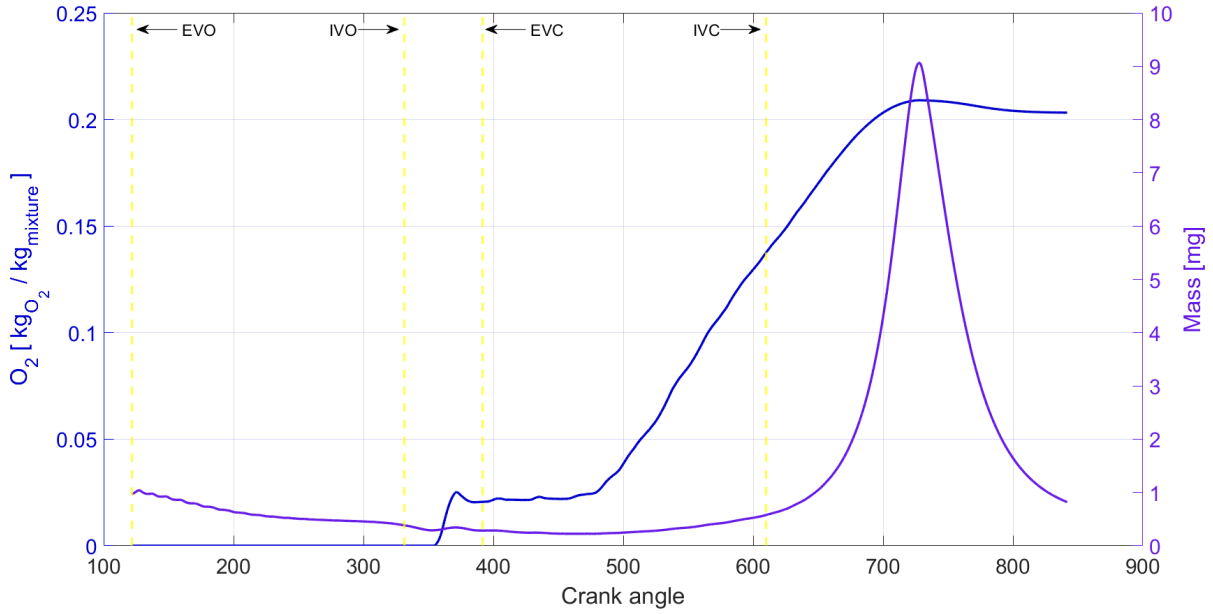

Figure 5.23: Oxygen mass fraction vs mass trapped in pre-chamber

Obviously, the trends of the mass fractions contained in the burned gas are specular compared to the trend of the oxygen mass fraction. As an example, the following figure where the mass fractions of oxygen and carbon dioxide in cylinder and pre-chamber are plotted together, proves the previous sentence.

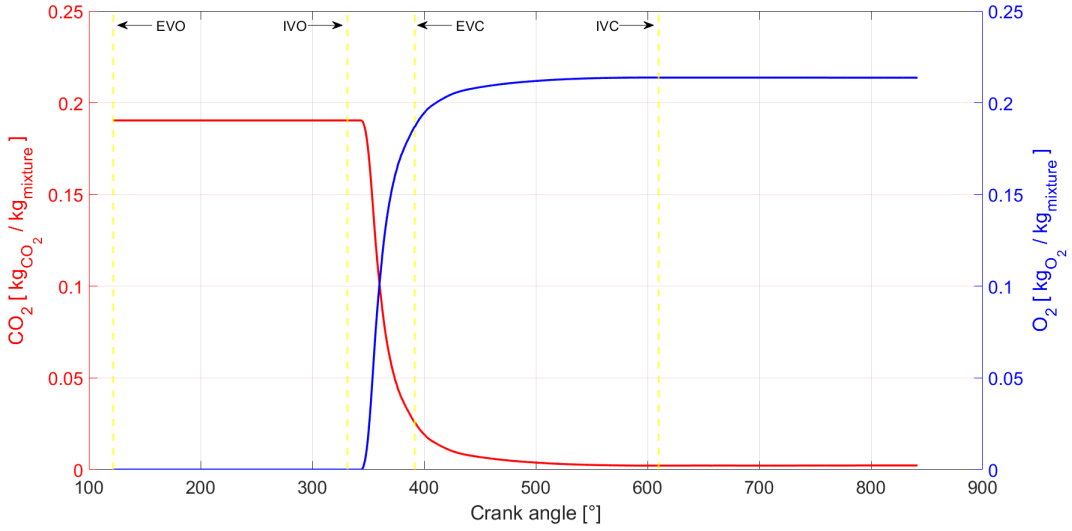

(a) Cylinder

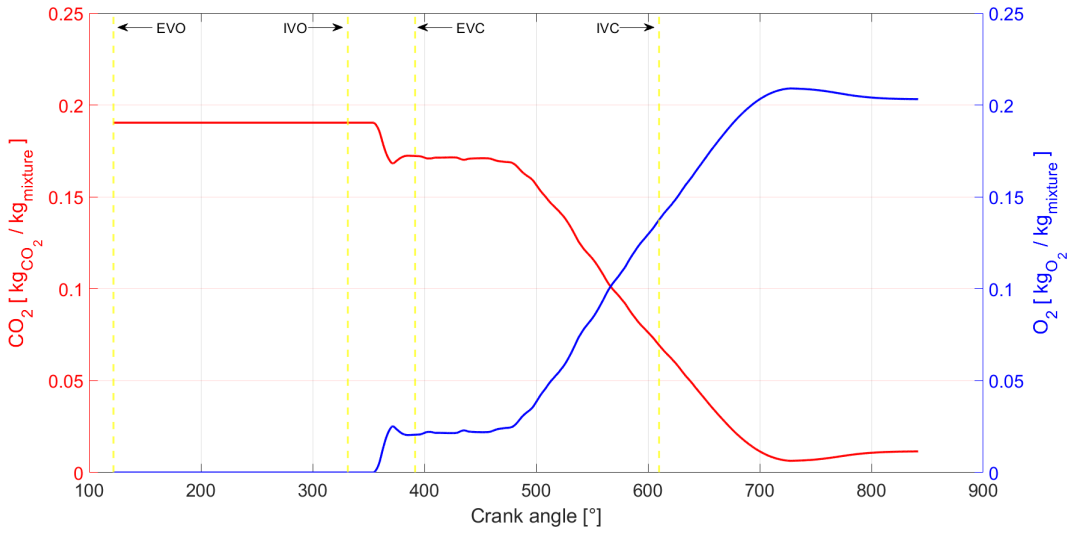

(b) Pre-chamber

Figure 5.24: Oxygen and carbon dioxide mass fractions

The curves of water and fuel mass fraction have exactly the same shape as the ones of the carbon dioxide, but with different concentrations.

Looking at Figure 5.24a, it can be noticed that the oxygen mass fraction increase (and corresponding carbon dioxide mass fraction decrease) does not begin exactly in correspondence of the IVO (i.e. 331.2 CAD), but the gas exchange process in the main chamber actually starts around 345 CAD, hence with a certain delay. This delay is caused by a backflow of the burned gas, since in the initial part of the overlap phase the pressure inside the cylinder is still higher than the pressure in the intake duct, thus the burned gas

tend to push the fresh charge back into the duct. The inversion of the pressure gradient between intake duct and cylinder can be noticed from the following picture.

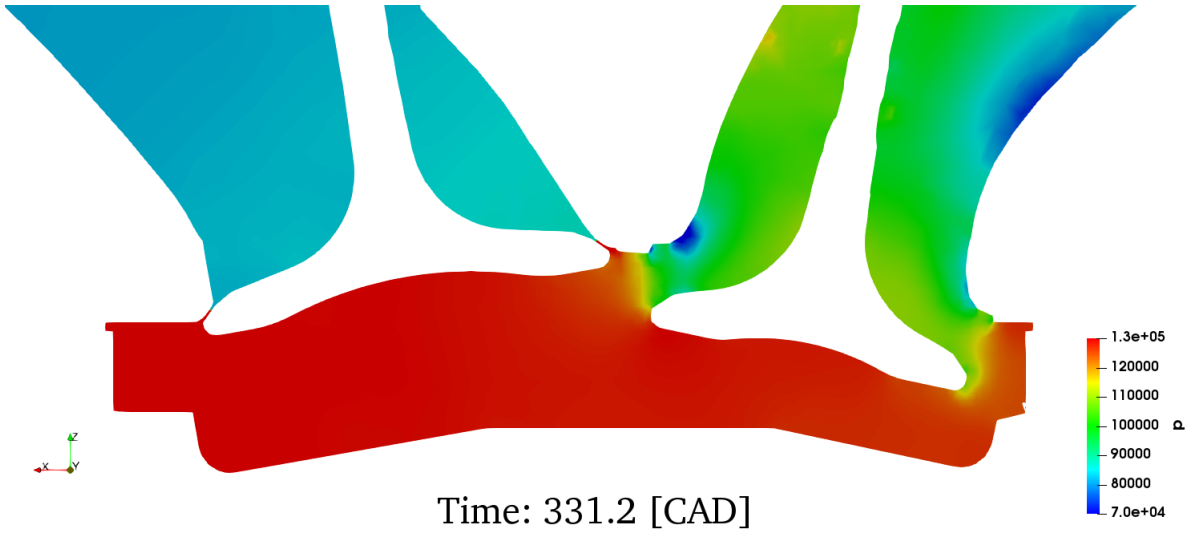

(a) IVO: start of backflow

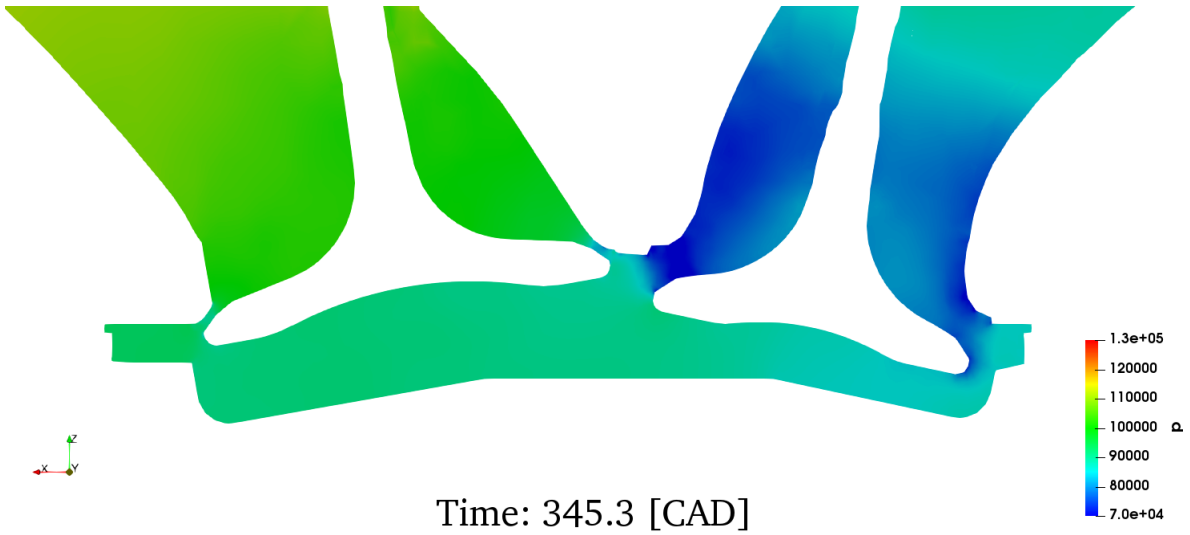

(b) End of backflow

Figure 5.25: Pressure field at the beginning of the overlap phase

The backflow at the beginning of the overlap phase can be easily seen also from Figure 5.26, where the oxygen mass fraction field is depicted inside the engine and it can be noticed that its concentration close to the gaps opening between the valve and the seat is lower compared to the rest of the intake duct because there the fresh mixture is diluted with the burned gases pushing from the cylinder.

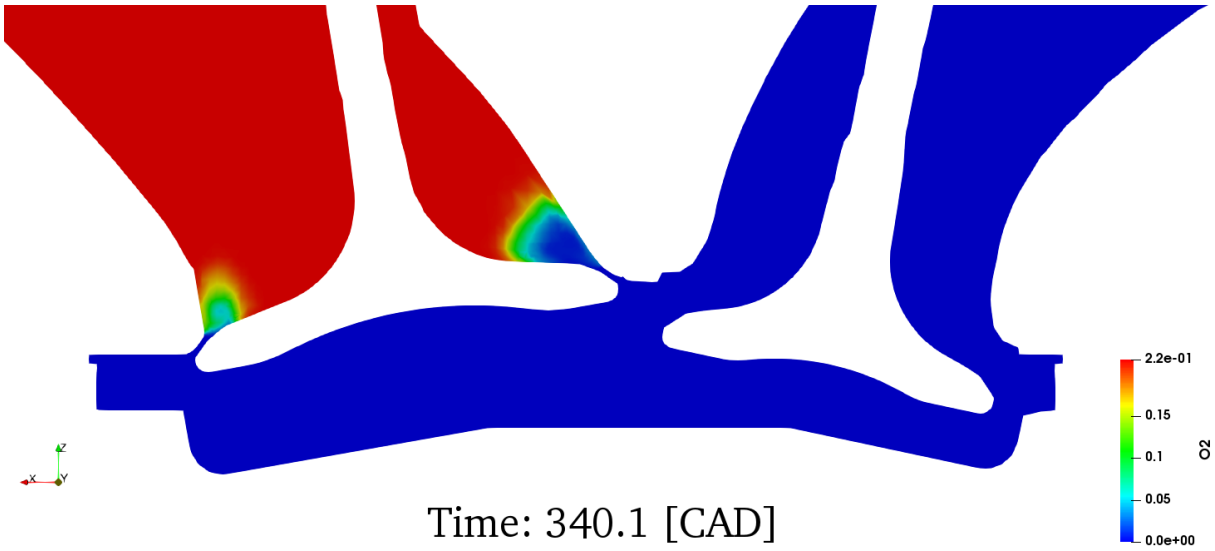

Figure 5.26: Oxygen mass fraction field during backflow

It is of great interest to known the exact amount of residual gas remaining inside the engine after the IVC, especially inside the pre-chamber, since a too high concentration of residual gas close to the spark plug may slow down the combustion development, or even cause misfires which would inevitably deteriorate the engine efficiency and performance. The following figure gives a first overview about the difference between the oxygen concentration inside cylinder and pre-chamber and the ideal concentration that it would be likely to achieve at the IVC, which is the oxygen concentration of the fresh charge in the intake duct, after the fuel injection.

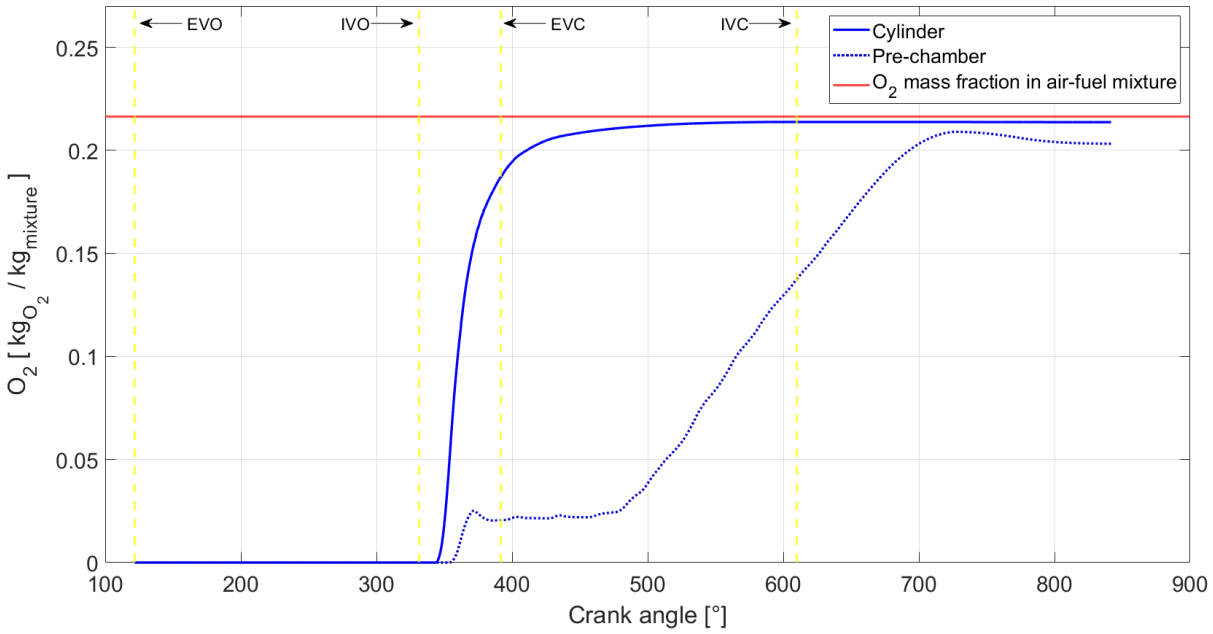

Figure 5.27: Oxygen mass fraction in cylinder and pre-chamber

From Figure 5.27 it can be noticed that the maximum oxygen concentration reached inside the pre-chamber is lower compared to the one of the main chamber, which in turn is lower than the ideal value, but not too far, highlighting the good gas exchange process taking place inside the cylinder at this engine operative point. The distance between the ideal and the actual oxygen concentrations is caused by the residual gas remaining after a non-optimal scavenging process in the cylinder and the pre-chamber.
In more detail, the residual gas concentration at IVC (i.e. 610.2 CAD) is of 1.2% in the main chamber and 36.3% in the pre-chamber. However, for the pre-chamber it is more important to known the amount of residual gas at the spark timing, since it is the moment in which combustion should start and considering the fact that the pre-chamber filling takes place during the compression stroke. In this case the concentration of residual gas in the pre-chamber at 697.7 CAD is of 6.5%. This value is definitely bigger compared to the amount of residual gas in the cylinder, proving once again the complexity of the pre-chamber scavenging process. As a consequence, the spark timing has to be carefully tuned to obtain the optimal combustion development in the two chambers, leading to the highest engine efficiency. It has to be considered that, for engines characterised by a TJI system, a shorter spark advance does not necessarily correspond to a delayed and lower pressure peak in-cylinder (as it would happen in a standard SI engine), because by delaying the ignition the mass trapped inside the pre-chamber is higher and also the residual gas concentration is lower, thus leading to a faster combustion inside the pre-chamber

and to more powerful jets going out from the orifices to the main chamber.
The concentration of residual gas was calculated by taking the value of oxygen concentration at IVC resulting from the simulation and considering as residual everything that is not oxygen with the correspondent amount of nitrogen and fuel to form a fresh mixture having the desired λ. Therefore the residual gas are composed by the total amount of CO_2 and H_2O, the amount of N_2 in excess compared to the standard mass fraction ratio in air and the amount of fuel in excess compared to the required concentration to obtain the target air-fuel ratio.

Pre-chamber filling

The following series of images starting from the IVO and ending slightly before the CAD corresponding to the spark timing shows the pre-chamber filling process, illustrating the oxygen mass fraction field for various instants of the overlap, intake and compression phases.

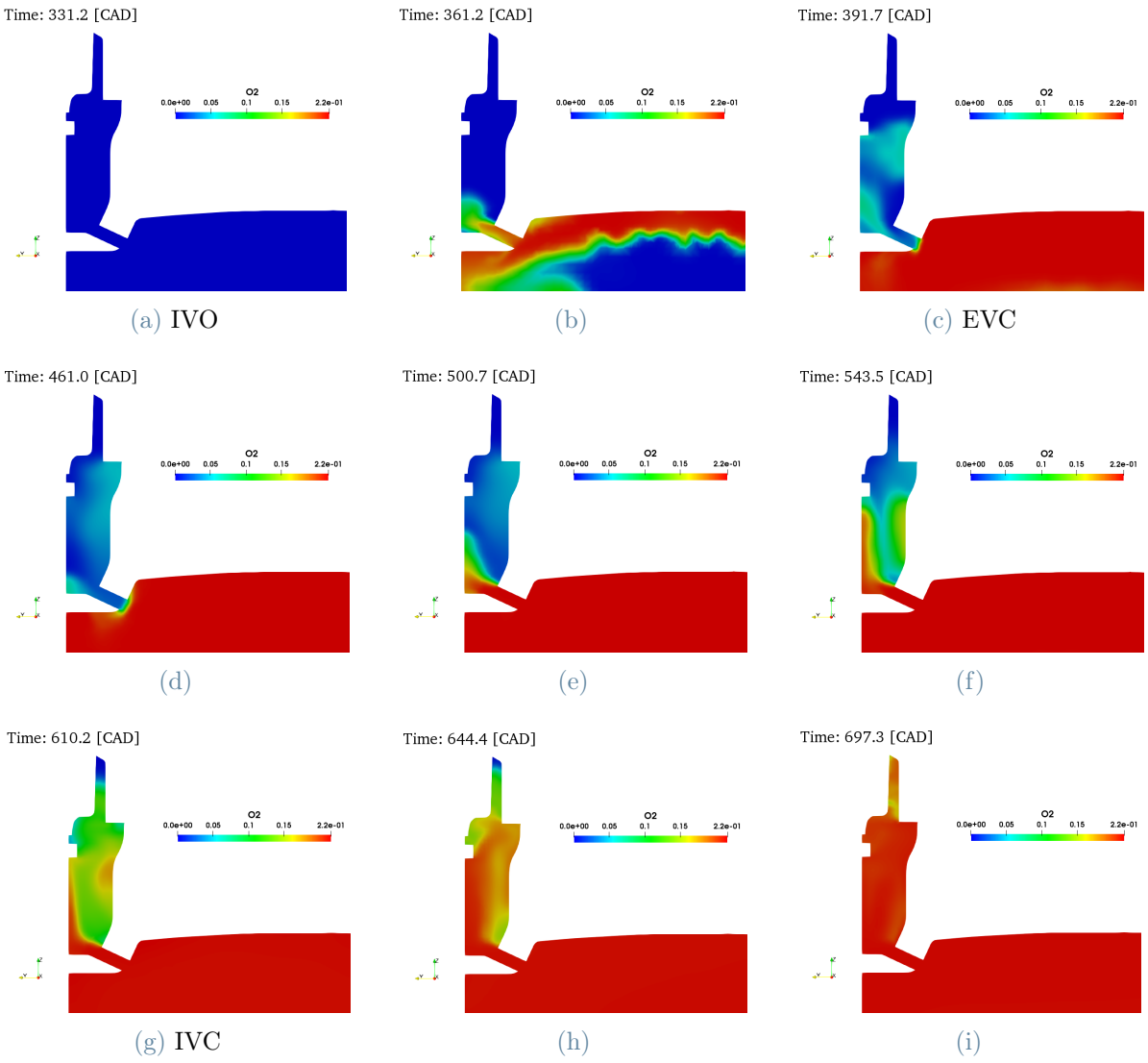

(a) IVO (b) (c) EVC

(d) (e) (f)

(g) IVC (h) (i)

Figure 5.28: Oxygen mass fraction field in pre-chamber

Looking at Figures 5.23 and 5.28 clarifies the different steps of the pre-chamber gas exchange and filling processes: some CAD after the beginning of the overlap phase, the combination of the scavenging process taking place inside the main chamber and the small volume consequence of the piston being close to the TDC causes a weak motion of fresh mixture towards the pre-chamber (Figure 5.28b); during the intake phase the suction effect caused by the piston moving towards the BDC prevents a continuation of the pre-chamber gas exchange process (Figures 5.28c, 5.28d). Finally, the actual pre-chamber filling process weakly begins when the piston starts its stroke back towards the TDC (Figure 5.28f), becoming much more vigorous after the IVC (from Figure 5.28g).

As demonstrated by Figures 5.28i and 5.27, at the spark timing a decent oxygen mass fraction is present inside the pre-chamber. However, as already stated in this section, a not negligible amount of residual gas is still trapped inside it.
The following figures show the distribution of the residual gas inside the pre-chamber, few instants before the spark timing.

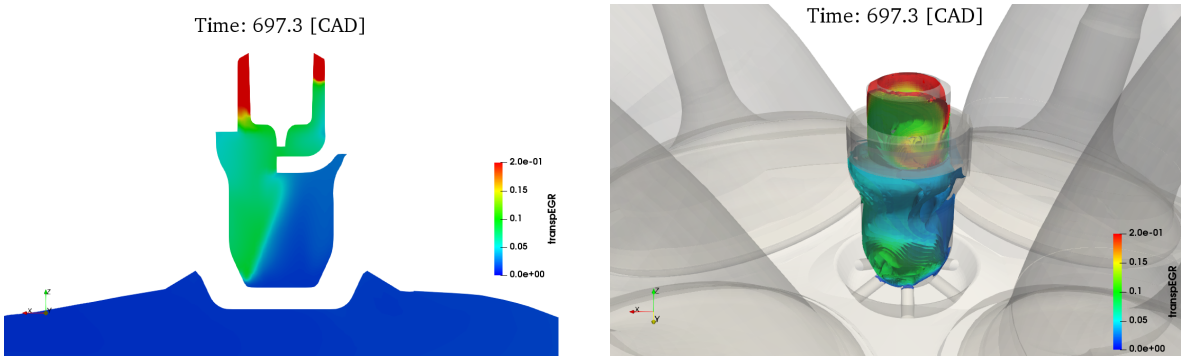

(a) Section on symmetry plane (b) 3D view

Figure 5.29: Residual gas inside the pre-chamber

Figure 5.29a shows the residual gas mass fraction field, whereas Figure 5.29b is a contour plot of the residual gas mass fraction, showing just the surfaces separating regions of the pre-chamber characterised by different concentrations. It can be noticed that most of the residual gas are trapped in the upper part of the pre-chamber volume, reaching a mass fraction over the total even higher than 20%, but also an amount around 10% is clearly visible in Figure 5.29a in the left part of the pre-chamber. This asymmetric distribution is a consequence of the filling process that is more favourable for the orifices on the left part of the pre-chamber, which is the side where the intake duct is located.
The following figure demonstrates what has been just stated, showing the velocity field for two sections dividing in equal parts the pre-chamber with respect to the symmetry plane and to the plane orthogonal to it. The second section was mirrored to have a better view of the motion inside the entire pre-chamber.

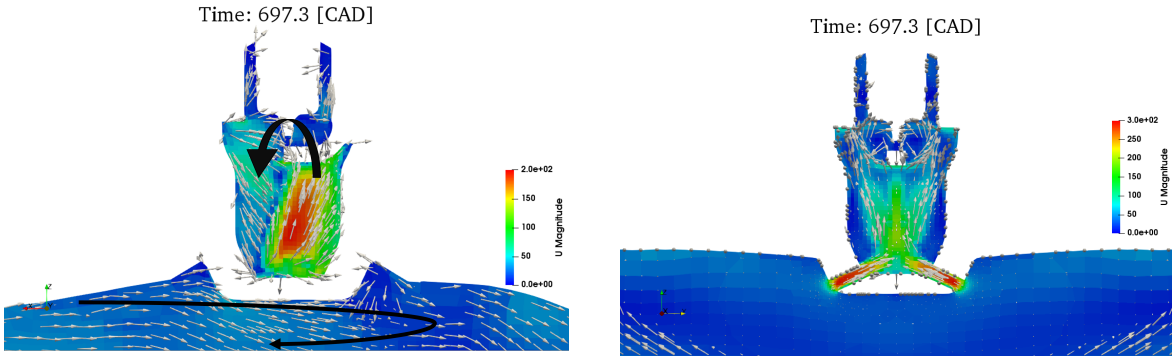

(a) Section on y-plane (b) Section on x-plane

Figure 5.30: Velocity field in pre-chamber

It is clearly visible from Figure 5.30a that the flow field in the pre-chamber on the y-plane is not symmetric. This is caused by the fact the pre-chamber filling is more facilitated on the side where the intake valve is located, because the velocity direction in cylinder given to the flow by the tumble motion developed during the intake stroke is more favourable to force the flow through the two orifices on that side of the pre-chamber. Since more mass enters from the left side of the pre-chamber, the flow inside it travels following an oblique direction. After impinging against the spark plug electrode and the pre-chamber top, a recirculating flow is generated, leading to a sort of tumble motion inside the pre-chamber, with a direction of rotation opposite with respect to the tumble motion in the cylinder. The black arrows in Figure 5.30a indicate the macroscopic flow motions inside cylinder and pre-chamber.

5.4. Other results

5.4.1. Turbulence quantities

From the simulation outputs it is possible to plot also the turbulence quantities, which in this case are k and ε. In the following figure the trend of these variables is depicted for both the main chamber and the pre-chamber.

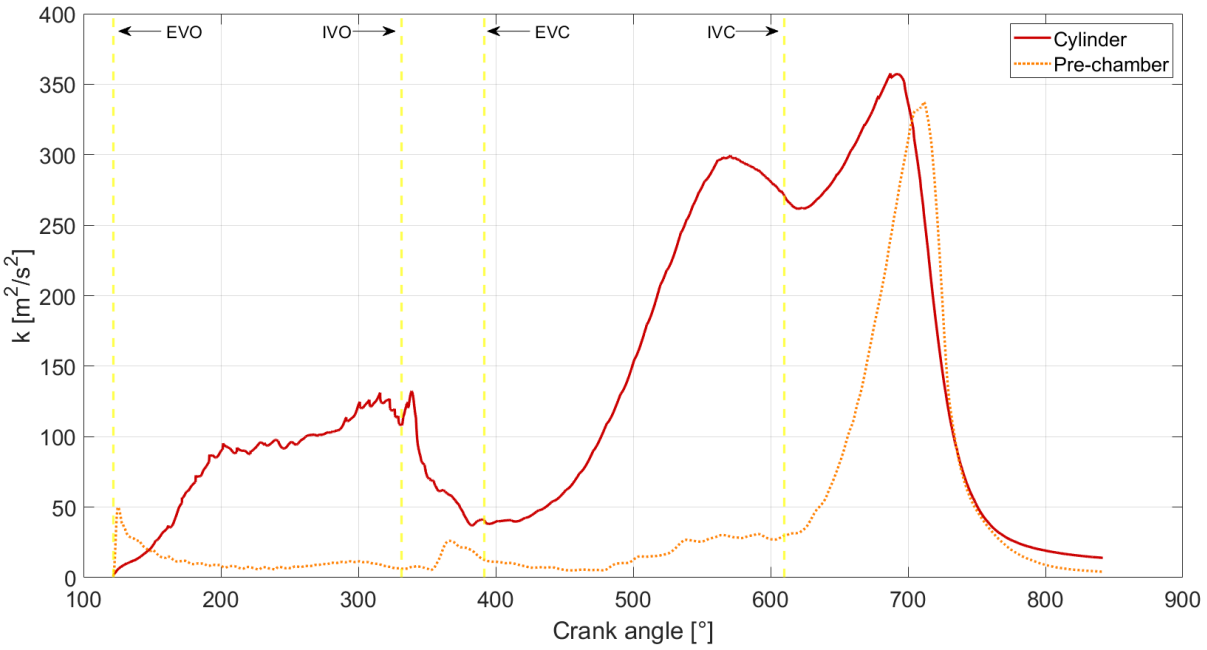

Figure 5.31: Turbulent kinetic energy in cylinder and pre-chamber

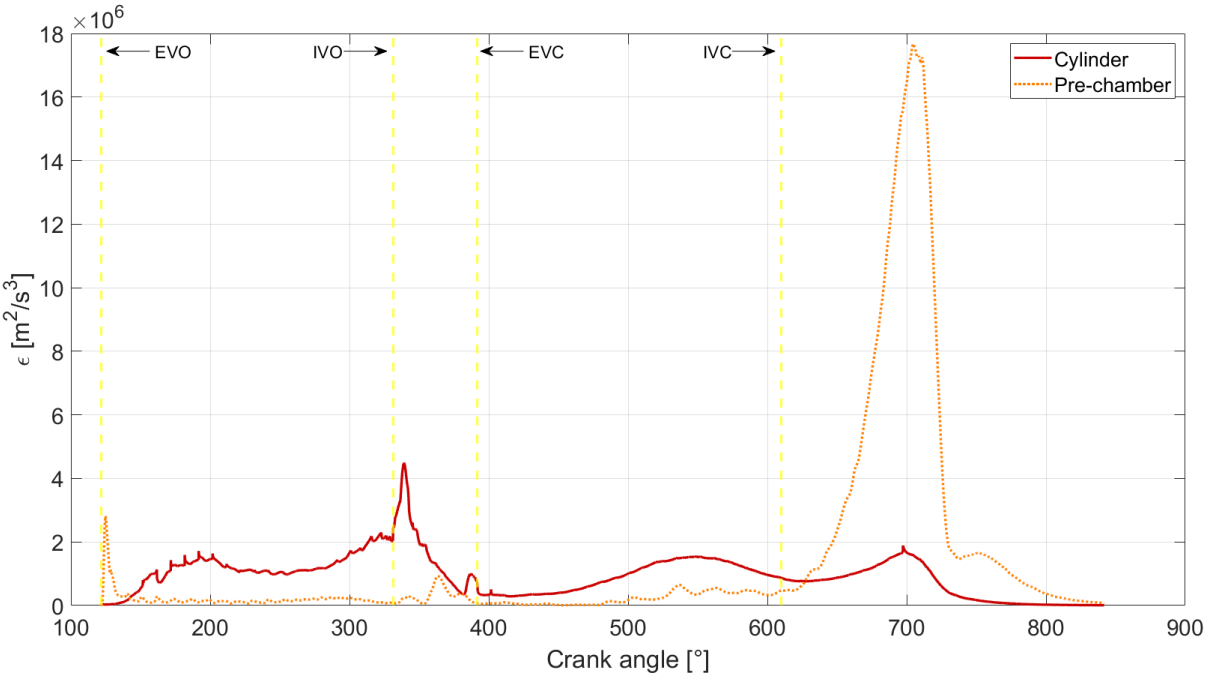

Figure 5.32: Turbulent dissipation rate in cylinder and pre-chamber

The turbulent kinetic energy is of particular interest, since the level of turbulence in the crank angles after the spark triggering has a very important effect on the combustion

propagation velocity. Indeed, one of the key parameters evaluated when designing a pre-chamber is the turbulent kinetic energy inside it at the start of combustion.
Figure 5.31 shows an almost steady level of k inside the main chamber during the exhaust phase, due to the gas velocity flowing out from the exhaust valve, and an increasing trend during the intake phase, caused by the tumble motion that develops during the intake stroke, as it will be better illustrated in the following section. The turbulent kinetic energy remains high for the initial part of the compression stroke, but then rapidly decreases when the piston approaches the TDC, thus extinguishing the existing charge motions and causing a remarkable reduction of the gas velocity inside the main chamber.
For the pre-chamber the trend of k is quite different, since the gas motion inside it is not influenced by the gas exchange process occurring in the main chamber. The only animated period in the pre-chamber is during the compression stroke, because the piston pushes the gas towards the cylinder head, forcing it to flow through the orifices. Due to the strong section reduction the flow velocity considerably increases and the gas enters inside the pre-chamber at high speed.

5.4.2. Charge motions

For what concerns the analysis of the charge motions, it must be taken into consideration the fact that the simulation was ran on a mesh of only half of the engine.
The swirl and tumble numbers are computed by referring to the center of the cylinder. However, since the other half of the engine is not present, there may be some motions composed by just a single eddy, thus leading to a swirl or tumble number different than 0, whereas in the entire engine the eddy may actually be balanced by a counter-rotating vortex, which would make the total contribution for a motion referred to a certain axis null.
Therefore, to have a clear view about which charge motions are present in the engine, an additional simulation on the entire engine mesh was performed.
In the following charts the comparison between the charge motion numbers computed in the simulations with half engine and entire engine are illustrated.

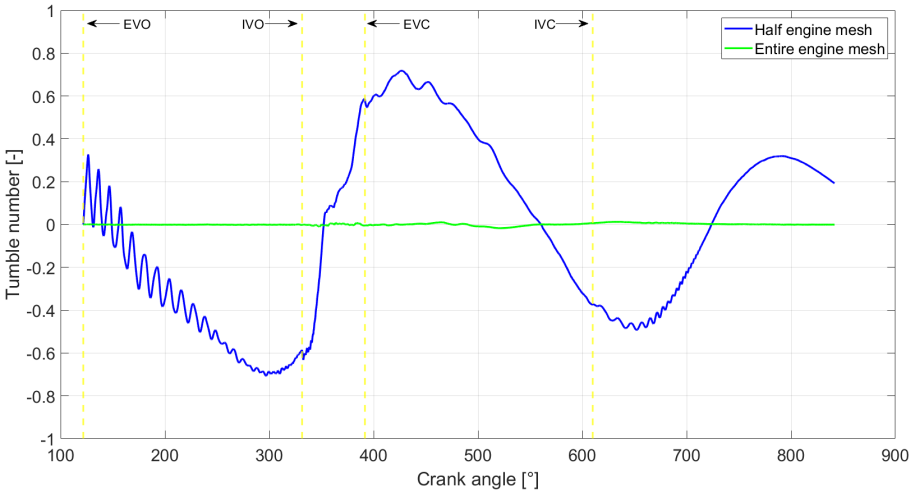

(a) Tumble motion around x-axis

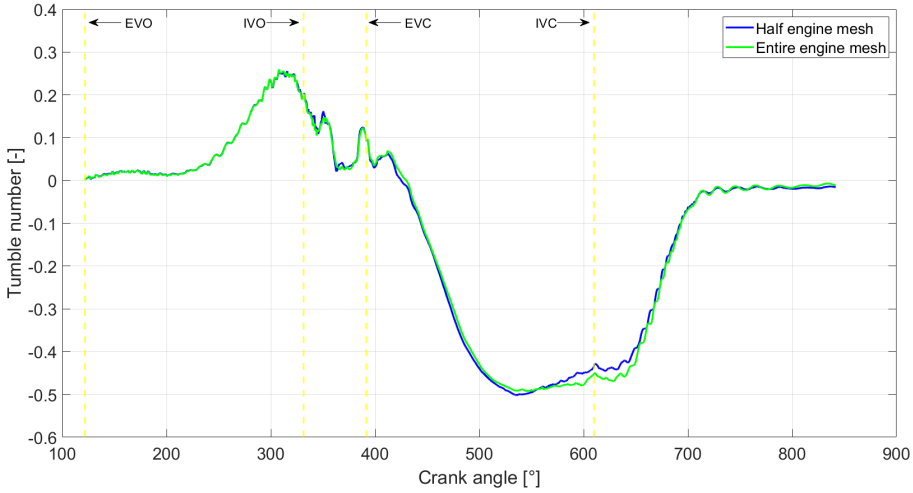

(b) Tumble motion around y-axis

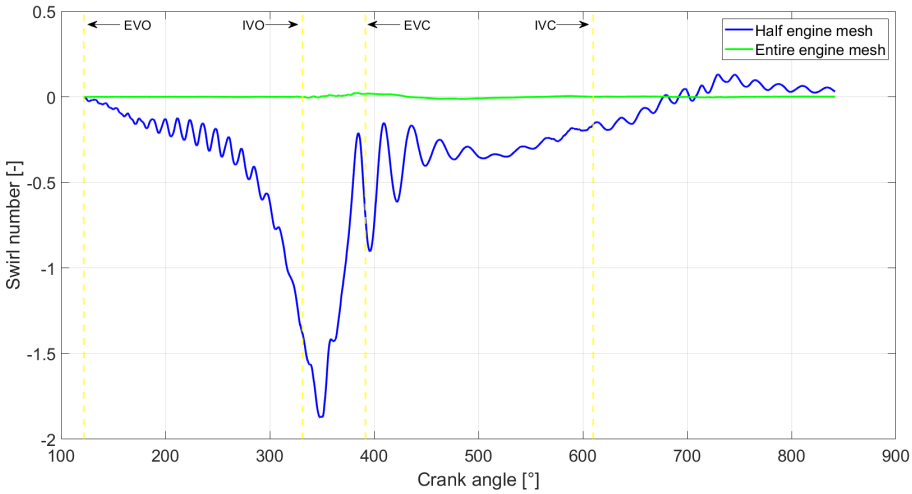

(c) Swirl motion

Figure 5.33: Charge motions

It is evident from Figure 5.33 that by simulating only half of the engine, a swirl motion and a tumble motion around the x-axis are detected, even if they are not actually present in the real engine.
The only charge motion that develops is the tumble around the y-axis, which is the axis directed as the normal of the symmetry plane, hence the tumble number in this situation is not influenced by the symmetry plane and it is correctly detected even by the simulation of only half of the engine, as it can be clearly seen from Figure 5.33b.
It can be also noticed that the motion intensity increases more and more during the intake phase, since it is generated by the fresh charge entering from the intake duct which is specifically designed to impress to the flow a direction such that when it impacts against the top of the valve it is then deviated towards the cylinder liner, passing below the exhaust valve. The tumble motion decreases its intensity during the compression stroke, up to an almost stationary condition when the piston reaches the TDC.
The figure below shows the velocity field in the engine at a CAD during the intake stroke, where the tumble motion is clearly visible.

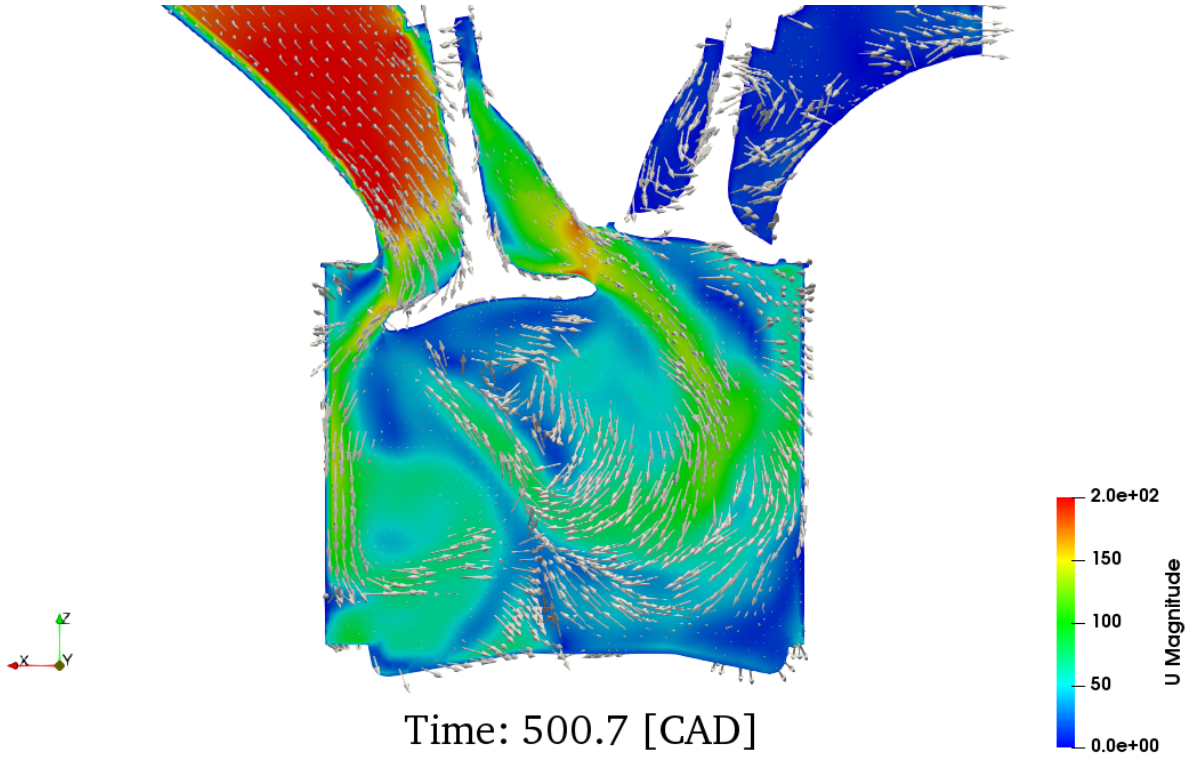

Figure 5.34: Velocity field: tumble motion in cylinder

After impacting against the liner, the flow assumes a cylindrical motion around the z-axis. If the mesh reproduces only half of the engine, then the flow keeps the cylindrical motion imposed by the liner and the symmetry plane, thus leading to a certain swirl number,

particularly marked at the beginning of the overlap phase, when the intake valve is gradually opening, as it can be seen from Figure 5.33c. However, in the real engine there are two intake valves, therefore there are also two cylindrical motions around the z-axis that will meet in the center of the cylinder. These two counter-rotating vortexes nullify each other, thus leading to a swirl number equal to 0.
A similar reasoning can be done also for the tumble motion around the x-axis, which is a motion once again caused by the flow impinging on the valve top during the intake phase, but this time is referred to the flow direction towards the other intake valve. Like for the swirl motion, in the case of the entire engine, the eddies develop symmetrically on the two valves, thus nullifying each other and leading to a tumble number around the x-axis equal to 0.

In conclusion, to be aware about which are the charge motions actually present in an engine (i.e. those generated because the engine was specifically designed) it is necessary to simulate the entire engine domain, otherwise it must be remembered that by exploiting the engine symmetry the trends of the charge motions that are influenced by the presence of the symmetry plane are not the real ones.
It is also of fundamental importance to visualize the results on the 3D model to see which is the velocity direction during each phase of the full cycle, thus to understand which flow motions are developing in the cylinder (e.g. a swirl number equal to 0 in a certain phase of the full cycle can be caused by the non-presence of a swirl motion or by the presence of two counter-rotating vortexes around a direction parallel to the z-axis).

5.5. Sensitivity checks

Due to the limited computational power and time available, it was not possible to carry out a thorough mesh sensitivity analysis, which would have required several increments of the mesh refinement level, causing an exponential increase of the computational time needed to create the mesh and to run the simulation.
However, some faster tests were performed anyway to have a rough idea about the influence of the mesh and of the time step on the simulation results.
The following tests were done:

- Comparison of the simulation results between the entire engine mesh and the half mesh.
- Comparison of the simulation results with a more refined mesh, featuring an average number of cells during the full cycle approximately three times higher than the

reference mesh, obtained by reducing the base size of the cells.

- Comparison of the simulation results with a higher time step over the full cycle, thus not complying anymore to the stringent condition on the maximum Courant number

5.5.1. Entire engine mesh

During this thesis work, the simulations were always performed by exploiting the engine symmetry, hence on a mesh of only half of the engine, that allowed to save a considerable amount of computational time.
Nevertheless, as already discussed in section 5.4.2, a simulation on a mesh of the entire engine was carried out to better analyze the charge motions in the cylinder. Being the results of this simulation already available, it was interesting to compare also the other flow quantities for the two cases, to be absolutely sure that exploiting the symmetry plane is a convenient choice that produces acceptable results.
As an example, below are illustrated the graphs of pressure and mass trapped in cylinder and pre-chamber for the two simulations.

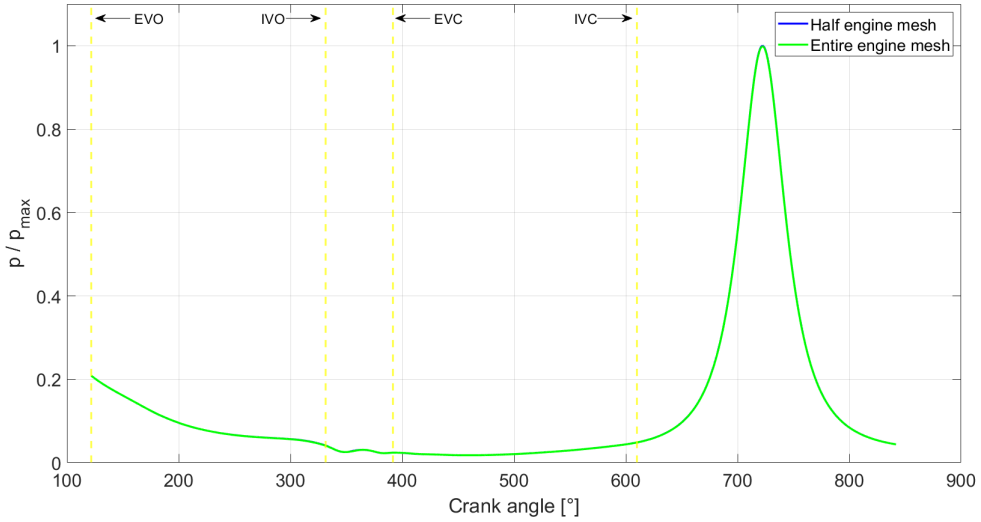

(a) Cylinder

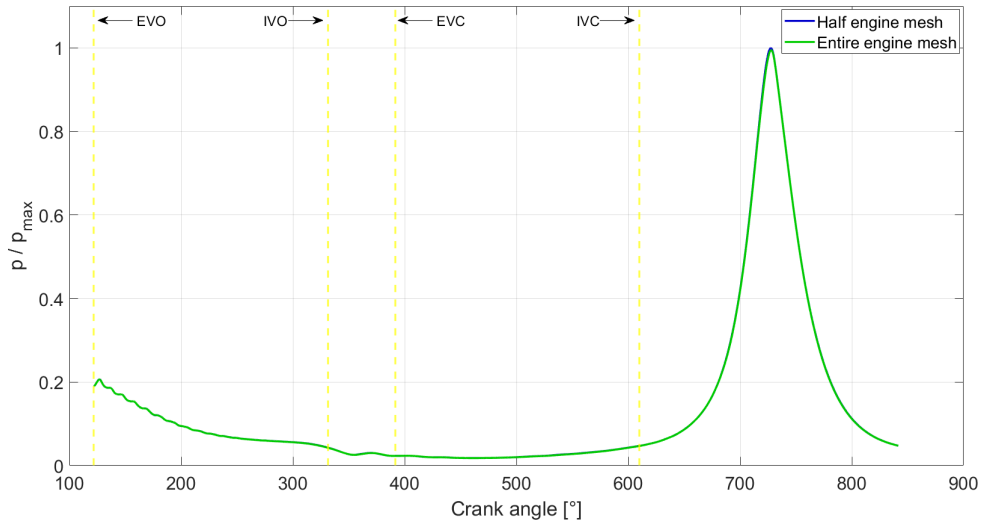

(b) Pre-chamber

Figure 5.35: Pressure curves comparison: half mesh vs entire mesh

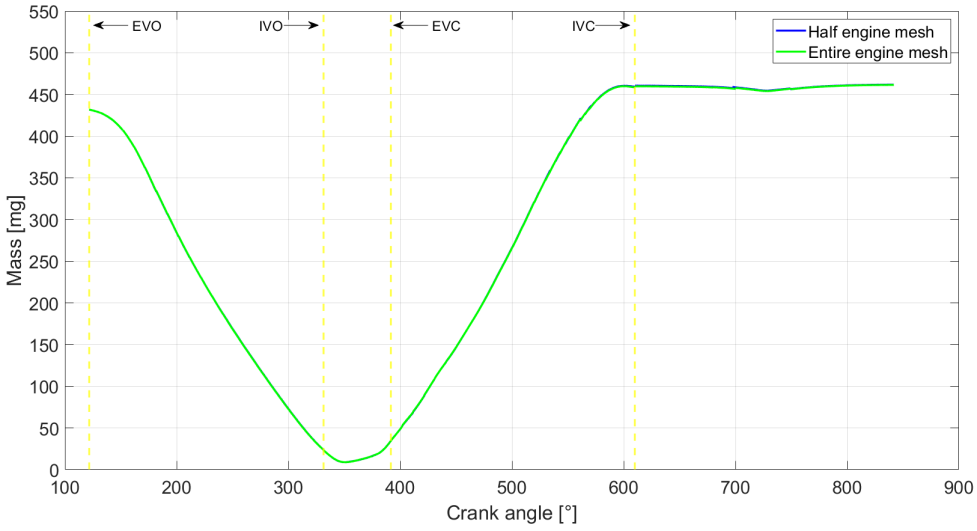

(a) Cylinder

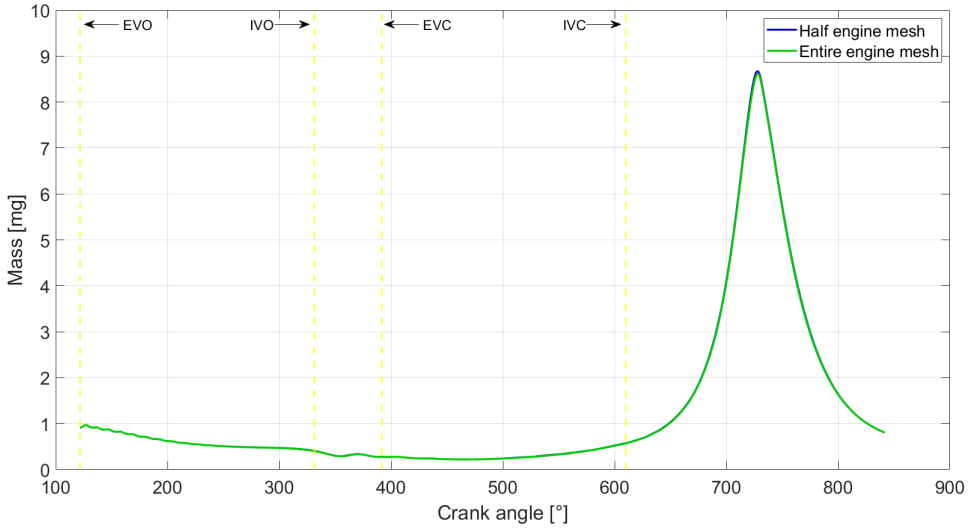

(b) Pre-chamber

Figure 5.36: Trapped mass curves comparison: half mesh vs entire mesh

The differences between the curves for the two simulations are totally negligible, with a difference of mass trapped at IVC of much less than 1%. Even the curves of temperature and mass fractions in cylinder and pre-chamber are almost perfectly overlapped for the two cases.

Therefore, the previous figures proved that the results obtained by simulating on a mesh of only half of the engine are completely reliable, leading to the conclusion that it is really advantageous to exploit the engine symmetry when possible, in order to save a good amount of time (i.e. +80% of time needed for the simulation with the entire engine

mesh).

5.5.2. Refined mesh

The use of a mesh with a higher refinement level is convenient to better reproduce the geometry of the real engine (i.e. discretizing the surfaces with a higher number of points) and to obtain more accurate results thanks to the reduction of the truncation error resulting from the discretization of the integrals composing the flow governing equations, which is usually proportional to the mesh spacing, as explained in section 2.2.1.
For the present thesis work, it was chosen to apply only one step of refinement compared to the base mesh, but with a conspicuous increase of the number of cells. The higher refinement level was obtained by reducing the base size of the cell, moving from 2.5 mm to 1.5 mm. All the regions where a higher level of refinement was applied are automatically scaled by halving each time the base size of the mesh, as illustrated for the reference mesh in table 4.1.
The new average number of cells for each mesh phase is shown in the following table, in comparison with the original mesh.

	Exhaust	**Overlap**	**Intake**	**Compression**
Average mesh number of cells (base size 2.5 mm)	215k	410k	306k	158k
Average mesh number of cells (base size 1.5 mm)	843k	1262k	1080k	608k

Table 5.1: Mesh number of cells comparison

In the following figures are plotted the curves of pressure, temperature and mass trapped, comparing the results between original mesh and refined mesh.

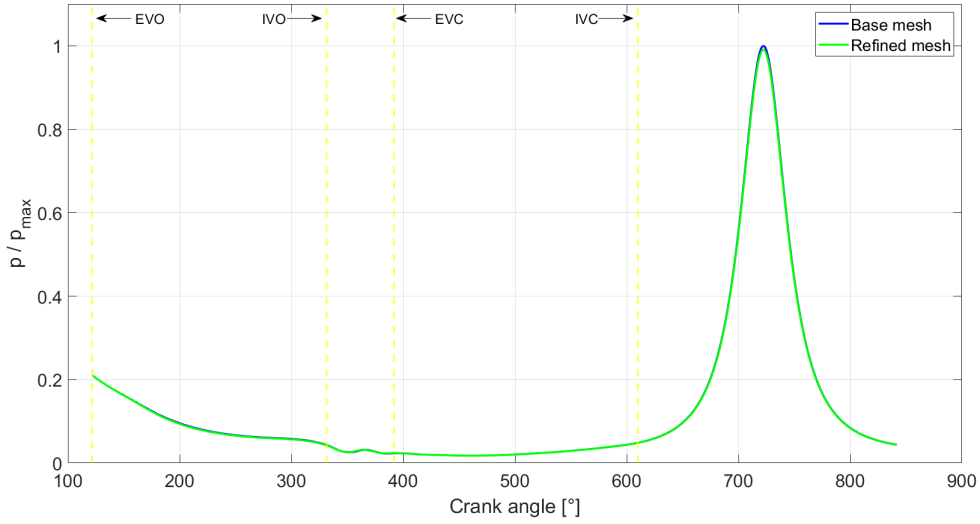

(a) Cylinder

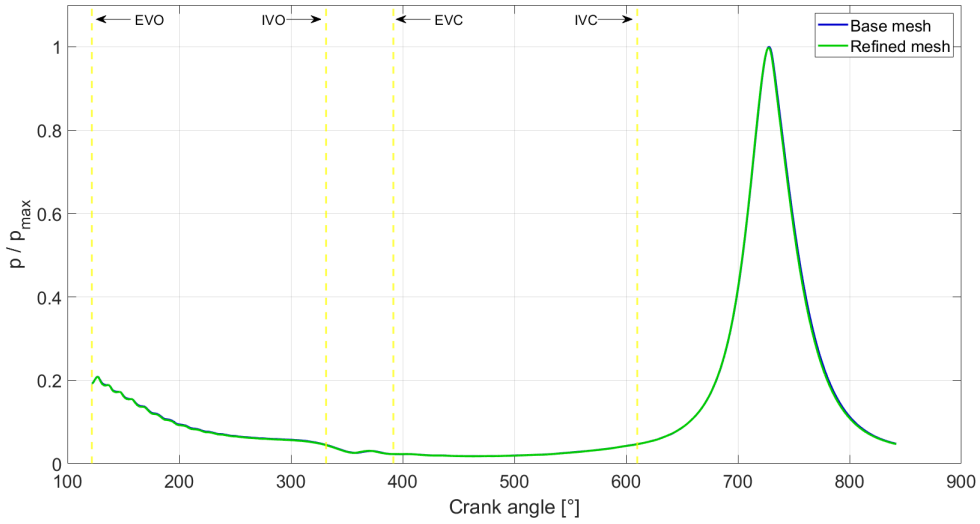

(b) Pre-chamber

Figure 5.37: Pressure curves comparison: base mesh vs refined mesh

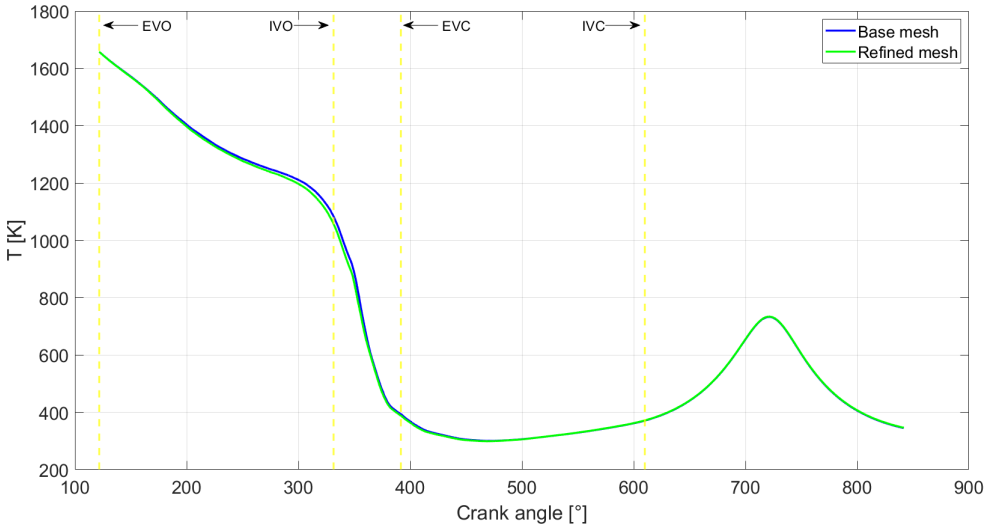

(a) Cylinder

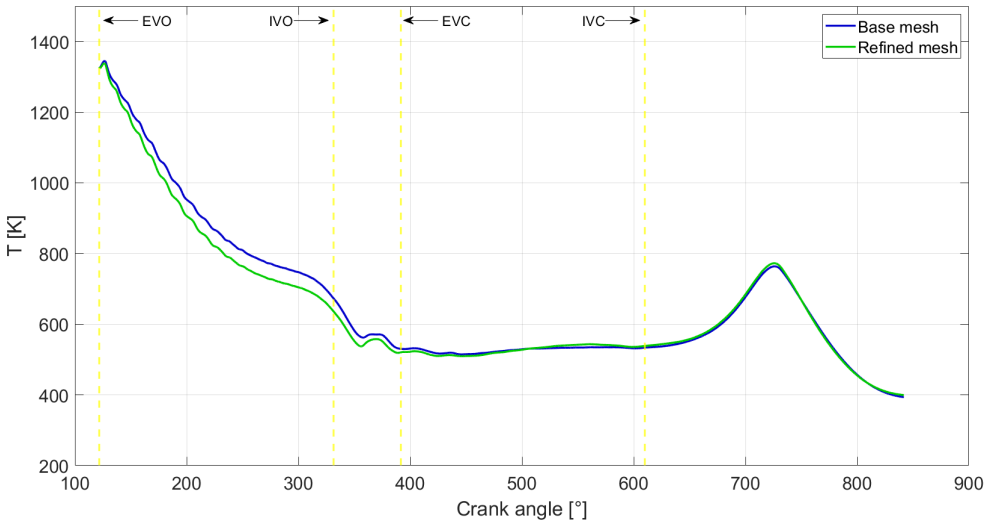

(b) Pre-chamber

Figure 5.38: Temperature curves comparison: base mesh vs refined mesh

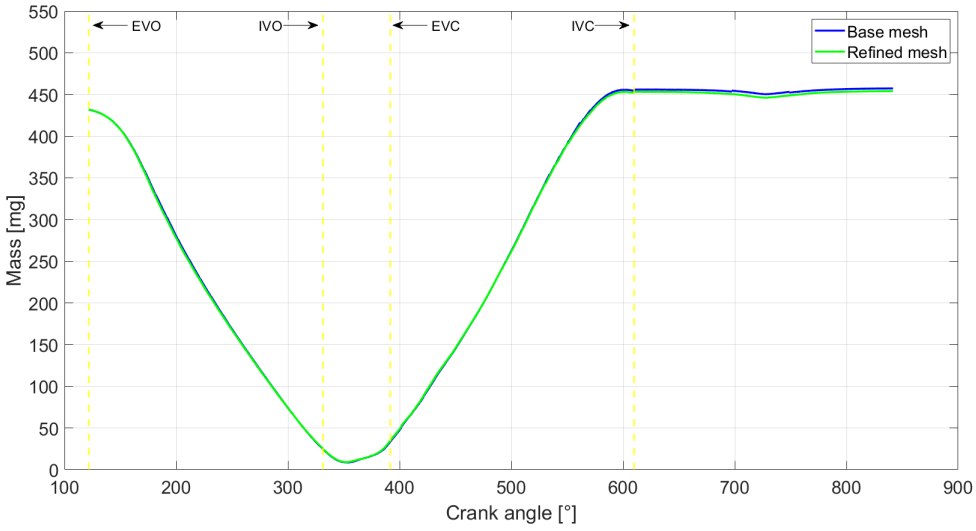

(a) Cylinder

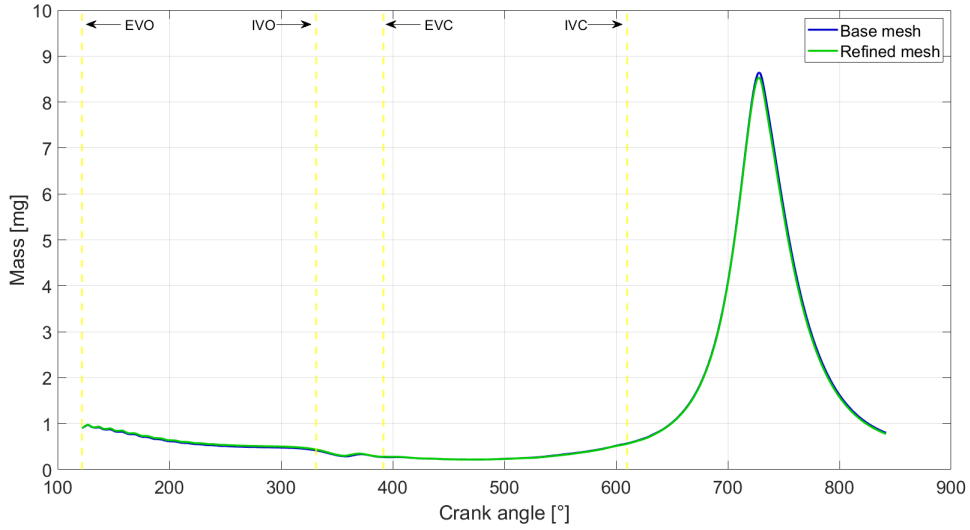

(b) Pre-chamber

Figure 5.39: Trapped mass curves comparison: base mesh vs refined mesh

From the previous figures it can be noticed that the results for the two cases are quite similar, with a difference of mass trapped of less than 1%.
The only not negligible difference is for the temperature curves, during the exhaust and overlap phases. Anyway, the values of temperature in cylinder and pre-chamber during the compression phase are almost equal in the two cases (i.e. difference of less than 10 K for the maximum temperature peak in the pre-chamber and around 1 K for the maximum temperature peak in the cylinder), therefore the results obtained with the less refined mesh are considered satisfactory looking forward to the a following combustion

simulation.
It can be concluded that the reference mesh used up to now is a good trade off between accuracy of the results and computational time required, especially considering that the simulation of the refined mesh took more than three times the time needed for simulating the reference mesh (i.e. +223%).

5.5.3. Increased time step

The results of the cold-flow simulation presented in the previous sections were obtained using a time step to have a maximum Courant number for each mesh always below or close to 1, in order to be in compliance with the CFL condition described at the end of section 4.2. However, since the Courant number depends on the local mesh size and flow velocity, its maximum value is often reached in small cells where the velocity is high, which are usually just few cells in comparison with the total number, and not always located in regions of particular interest for the flow description. Indeed, the mean value of Courant number over the entire mesh is always orders of magnitude lower than 1. For this reason, especially looking to industrial practice, it may be convenient to increase the time step everywhere, except for those critical phases like when the valves are in proximity of the minimum lift position, in order to reduce the computational time needed for each simulation. Of course, it is sensible to do it only if the results are not significantly affected (i.e. the trade off between additional error and saved time is acceptable).
For the less time-consuming simulation the time step was increased of 5 times during the overlap phase (i.e. from 0.002 CAD to 0.01 CAD), except for the few initial and final mesh where the valves are close to the minimum lift position, and of 2 times for the exhaust, intake and compression phases (i.e. generally from 0.01 CAD to 0.02 CAD). This setup guaranteed a time saving of -162% compared to the reference simulation.

The results obtained were definitely satisfying, showing negligible differences for all the most meaningful flow quantities, as demonstrated by the following figures.

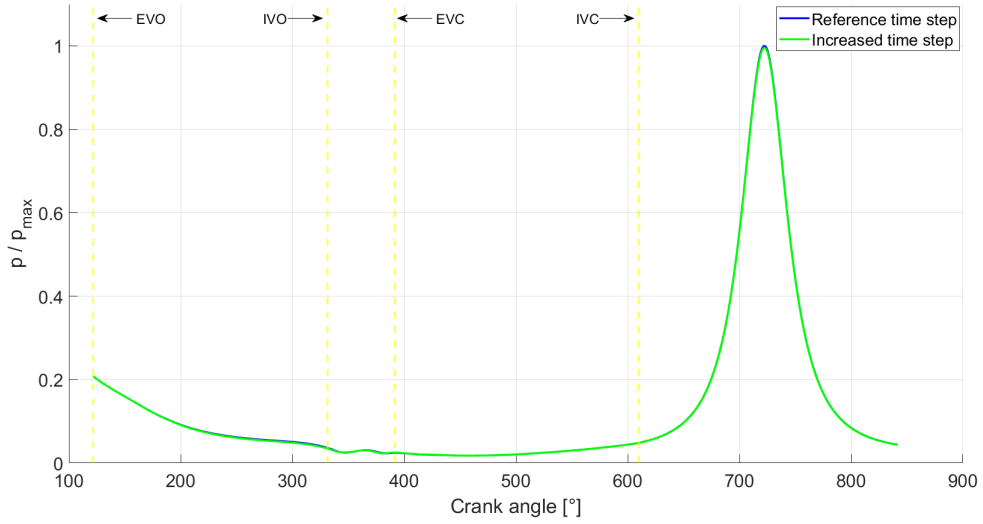

(a) Cylinder

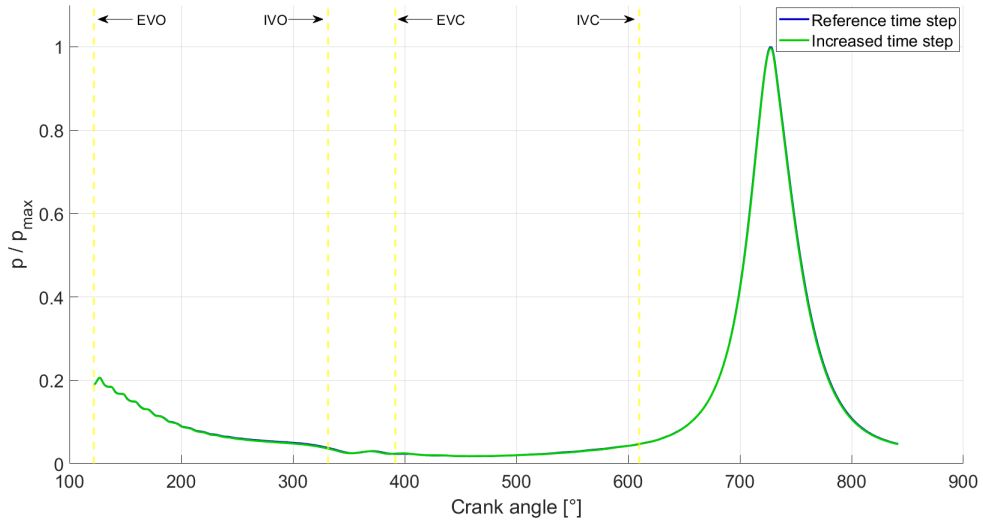

(b) Pre-chamber

Figure 5.40: Pressure curves comparison: reference time step vs increase time step

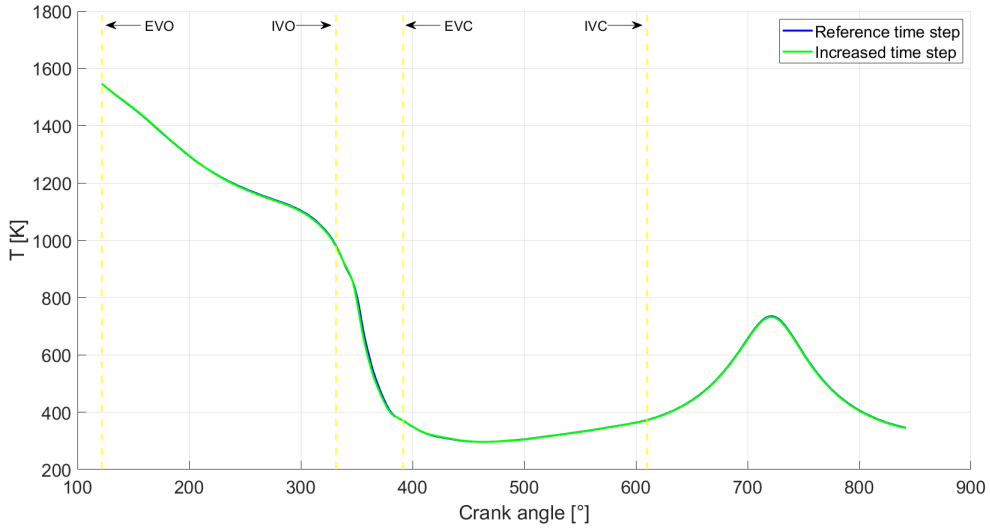

(a) Cylinder

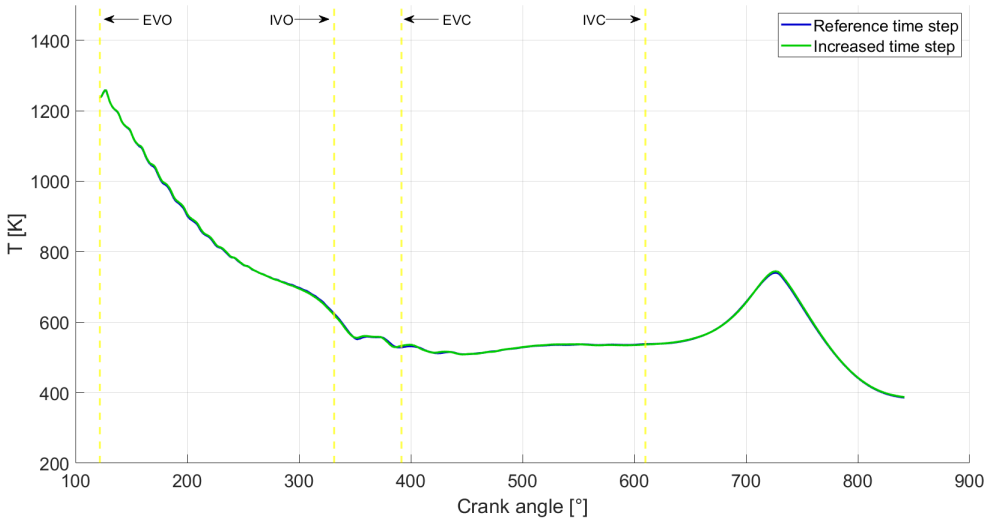

(b) Pre-chamber

Figure 5.41: Temperature curves comparison: reference time step vs increase time step

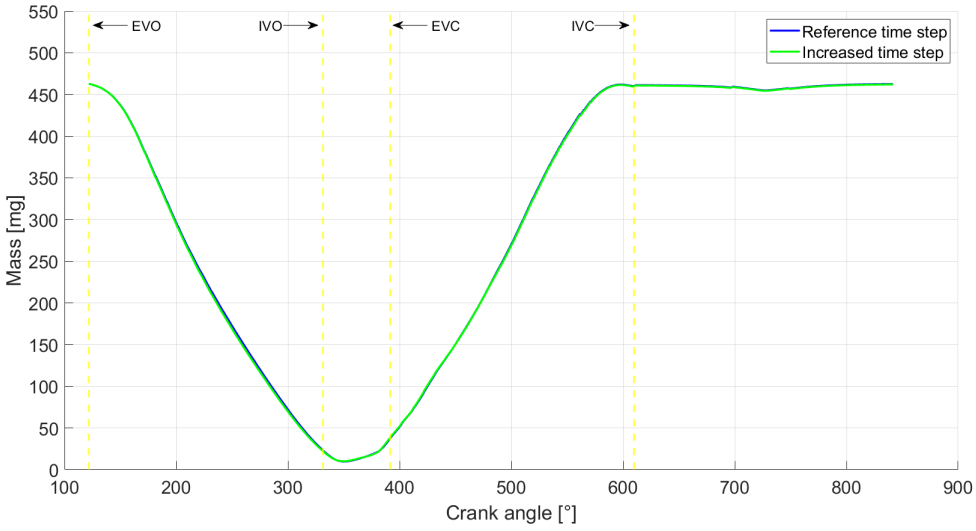

(a) Cylinder

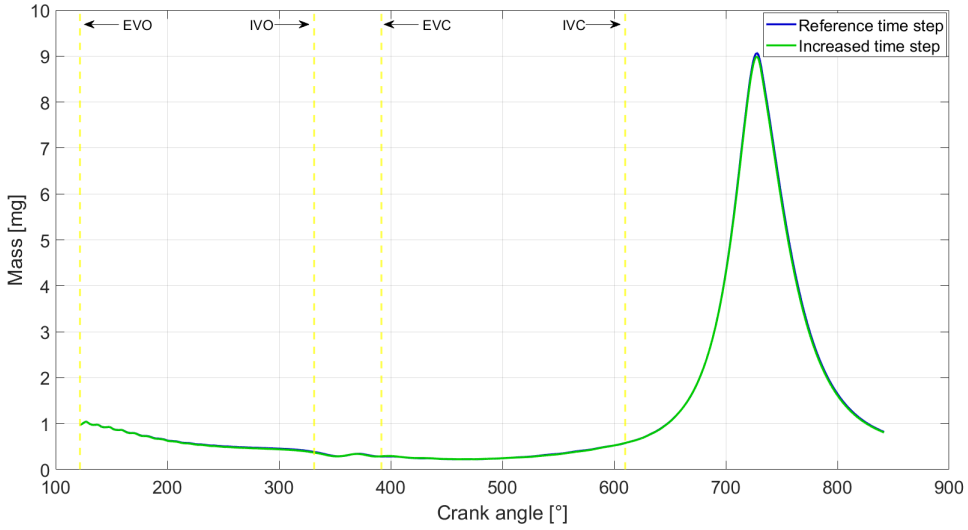

(b) Pre-chamber

Figure 5.42: Trapped mass curves comparison: reference time step vs increase time step

6 | Power-cycle simulation

In the final part of this thesis work it was possible to perform some preliminary simulations also including the combustion process, thanks to a novel approach implemented in the LibICE library that now allows to run a simulation with a combustion solver on a multi-mesh case, exactly like it was done for the gas exchange simulation. This new approach is much more user-friendly, since no significant modifications must be applied to the standard setup used for the cold-flow simulation: the same mesh already created can be used and the global numerical setup remains the same, with the only differences that are closely related to the new dictionaries that have to be setup for choosing the simulation parameters to model the ignition and combustion processes.
Once again the target was to obtain results from the simulation as close as possible to the experimental data available. The gas exchange process was already correctly reproduced by tuning the cold-flow simulation, as described in the previous chapter, hence the conditions up to the spark timing are considered as defined. As a consequence, now the focus is on the pressure curve, paying close attention to the pressure behaviour inside the pre-chamber, since the pressure trend in the main chamber is directly linked to what happens during the first phase of the combustion development inside the pre-chamber.

6.1. Combustion simulation setup

The overall numerical setup does not present any significant differences compared to the cold-flow simulation, except for the definition of the ignition and combustion model parameters.
The new approach was thought so that the solver for simulating combustion works in a similar way as it was for the cold-flow solver. Indeed, one can also think of simulating a brand new case directly with a fired cycle by specifying from which crank angle the combustion solver must replace the standard cold-flow solver. From the first case in which the combustion solver begins, new fields necessary for the combustion simulation are defined (e.g. unburned gas temperature, mass fraction burned, transported EGR, laminar flame speed and many others...) and mapped each time the simulation switches to the following

mesh.

The simulation was performed starting from few CAD before the spark triggering, to reduce as much as possible the computational effort needed. The initial conditions are defined by mapping the fields from a mesh of a case coming from the cold-flow simulation to a following clean case and initialising all the new fields needed for the combustion solver.

The new and most important parameters to be defined are the ones related to the ignition of the gas mixture inside the pre-chamber, according to the energy deposition model described in section 2.3.
The spark ignition location was specified between the two spark plug electrodes. The parameters regulating the energy deposition are the spark strength and duration, that were defined according to typical values considered as reliable for this kind of spark plug, based on data available from previous researches. Therefore, the main parameters that were tuned during this thesis work were the spark diameter and the spark advance.
The spark diameter represents the dimension of the sphere where the energy deposition takes place at the specified spark timing. With this kind of ignition model, the very first phases of flame initiation and propagation are not simulated, but it is simply assumed that a considerable amount of energy is introduced inside a sphere where the mixture completely burns according to the specified parameters for the energy deposition. Consequently, in the light of such simplified approach, it is reasonably expected that the experimental value of spark-advance needed to be slightly calibrated to improve the prediction of the experimental heat release rate.

As a first attempt, the ignition kernel was centered between the spark plug electrodes and it was chosen a sphere with a diameter of 4 mm. The location and dimension of the ignition kernel are shown in the following picture.

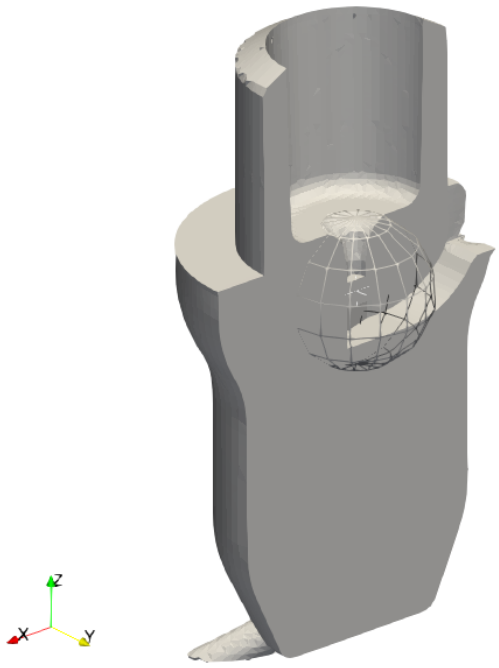

Figure 6.1: 3D representation of the ignition kernel location

Initially, the spark timing was set equal to reference value (i.e 697.7 CAD).

6.2. Combustion simulation results

In the following figures are shown the results of the first combustion simulation concluded, with the setup parameters specified in the previous section.

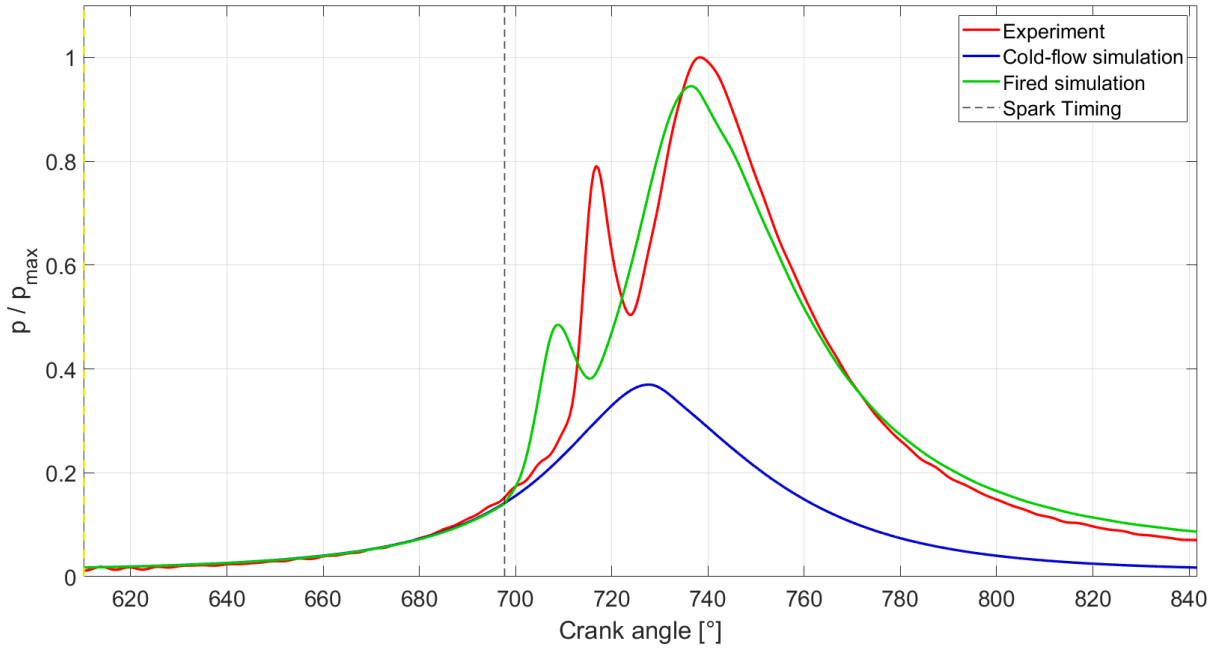

Figure 6.2: Fired cycle pre-chamber pressure curve

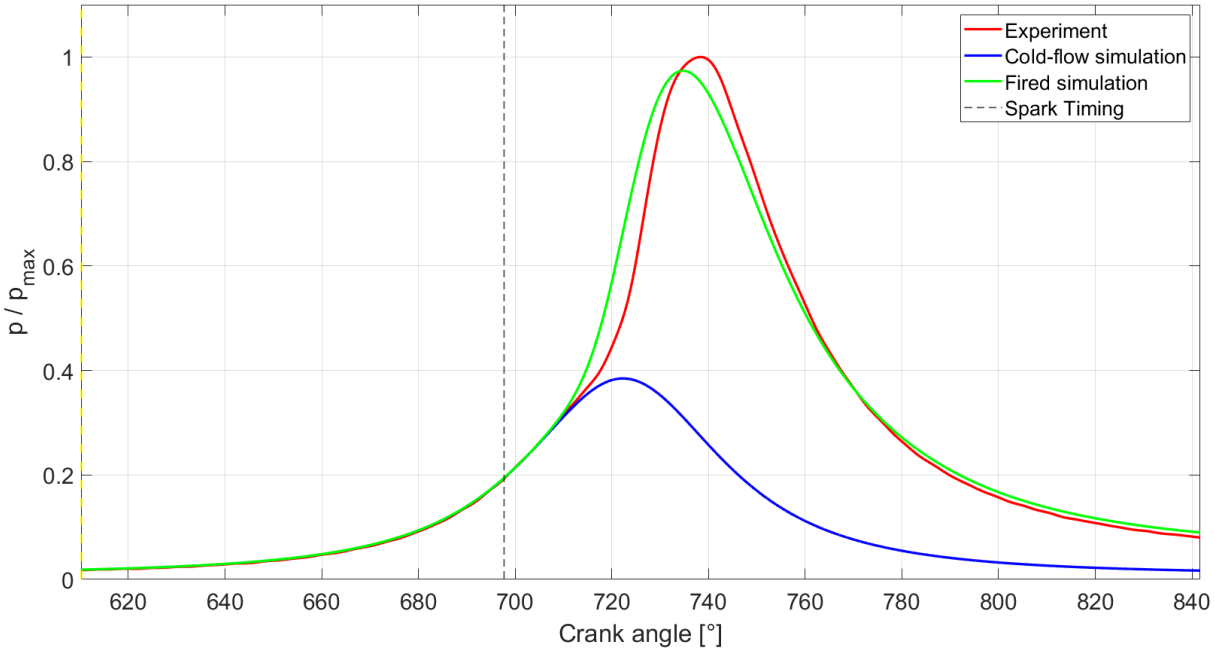

Figure 6.3: Fired cycle cylinder pressure curve

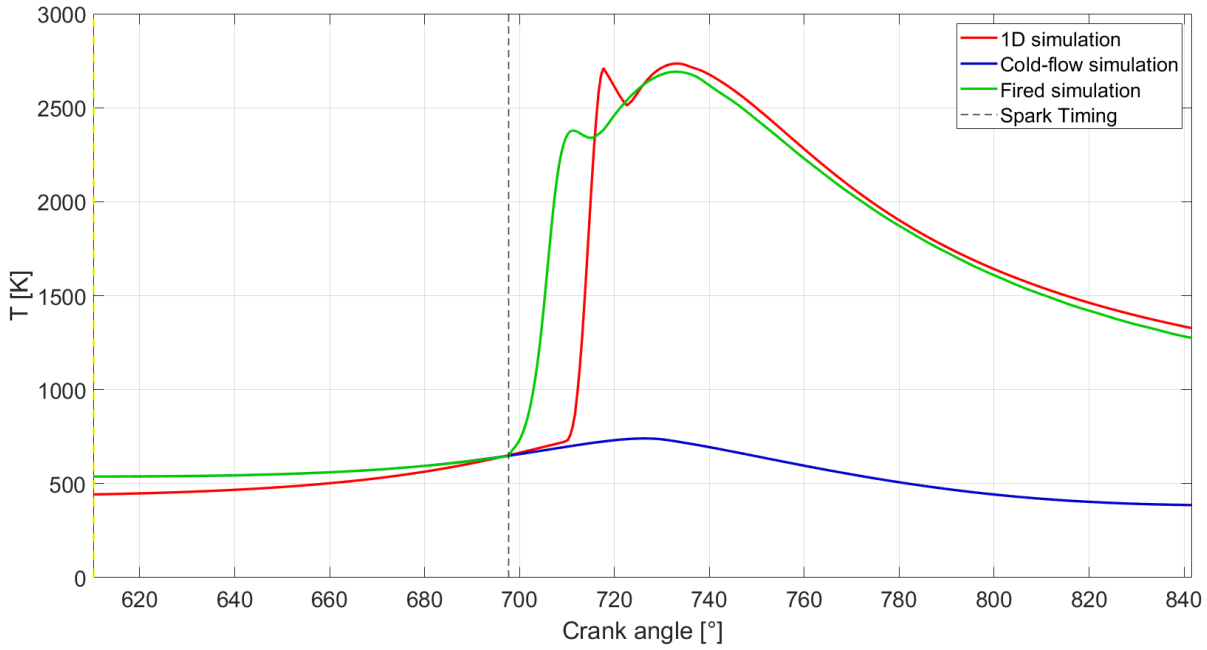

Figure 6.4: Fired cycle pre-chamber temperature curve

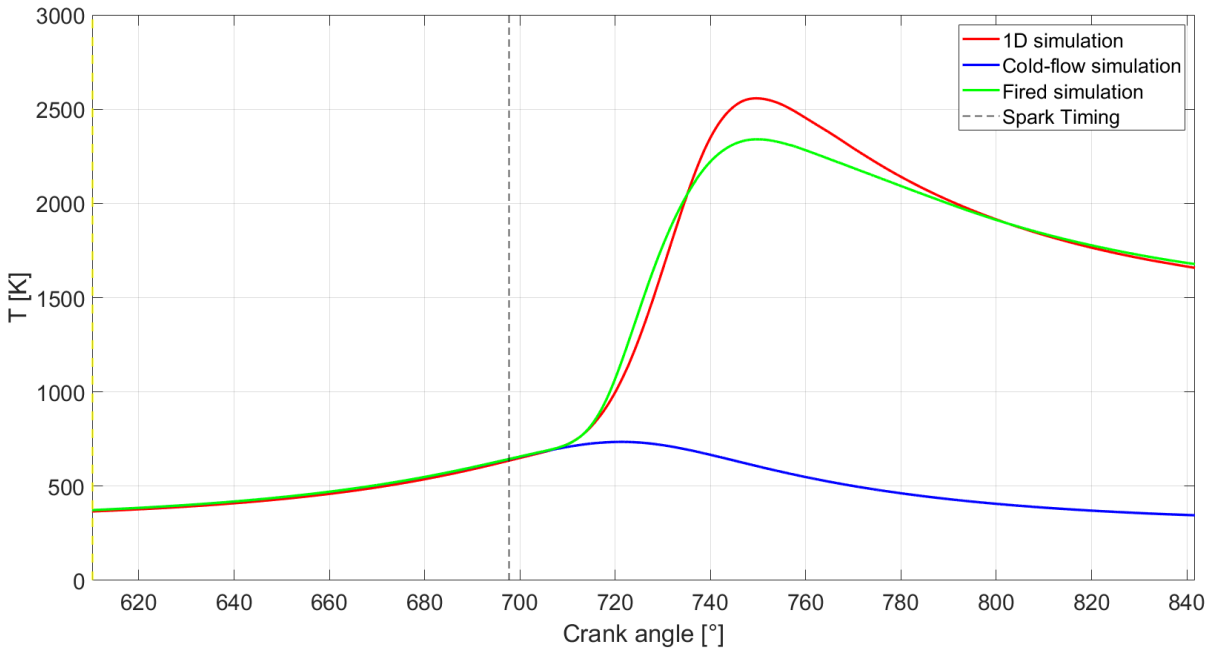

Figure 6.5: Fired cycle cylinder temperature curve

It is clear from Figures 6.2 and 6.4 that the spark advance is too early compared to the experimental curve. This is probably caused by two main aspects. First, the adopted

ignition model, which initialises a static sphere of burned mass between the electrodes, without considering possible stretch effects caused by the mixture velocity in the spark-gap. Second, the spark triggering in the real engine can be retarded with respect to the signal sent by the ECU, due to an electric delay.
The early ignition of the charge causes an anticipated and lower first pressure peak in the pre-chamber due to the lower mass trapped inside it, since the ignition generates a rapid temperature and pressure increase, that first of all blocks the pre-chamber filling process, and then causes the ejection of the burned mass.

Having seen the results of the first simulation, it was decided to delay the spark timing in order to obtain a first pressure peak in the pre-chamber which is properly phased with the peak of the experimental pressure trace. To obtain such result, it was necessary to delay the spark timing of 10 CAD.
The following figures show the graphs of some of the most interesting flow quantities resulting from the combustion simulation with the reduced spark advance.

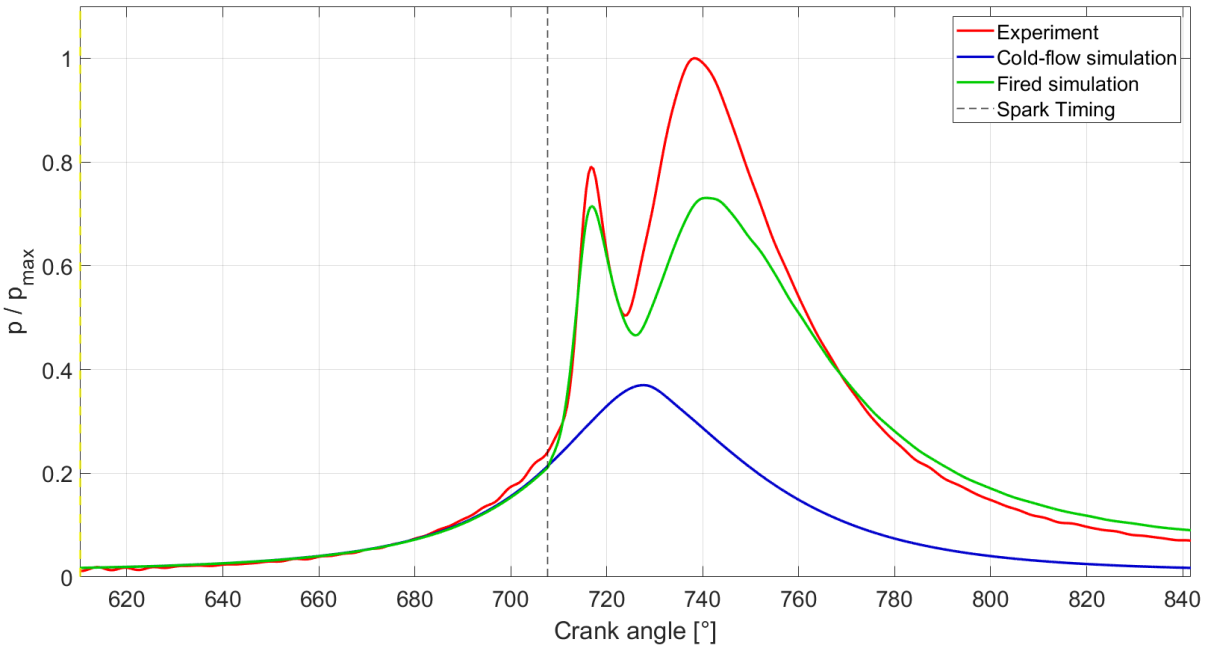

Figure 6.6: Fired cycle pre-chamber pressure curve: delayed spark timing

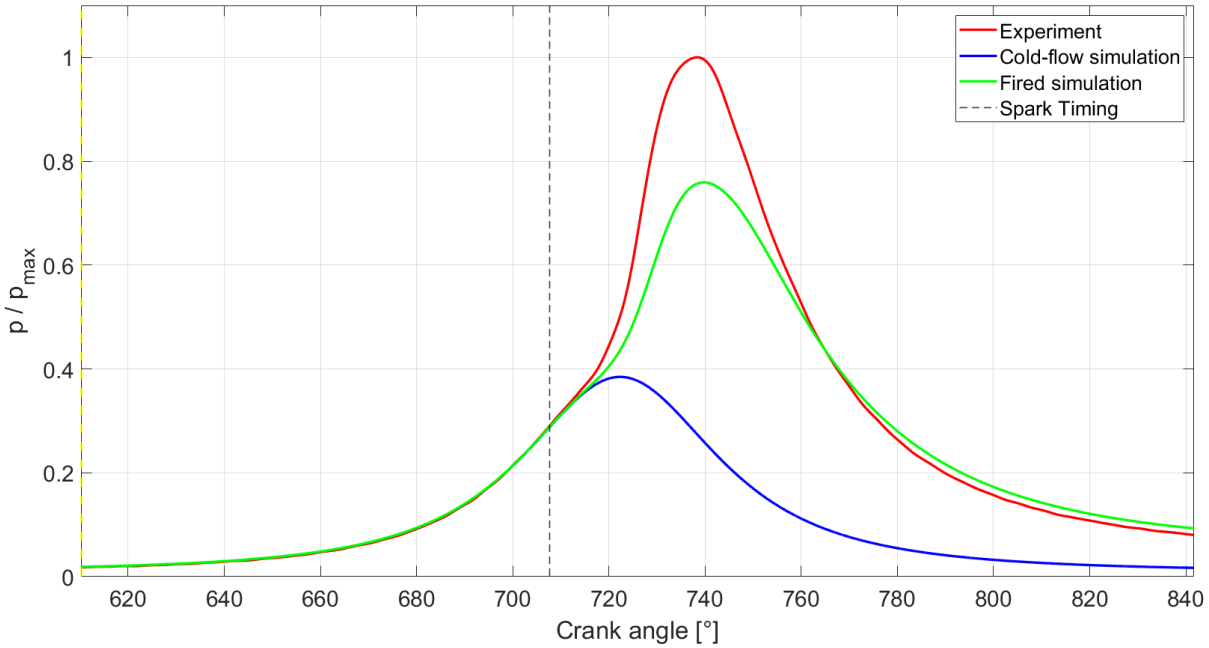

Figure 6.7: Fired cycle cylinder pressure curve: delayed spark timing

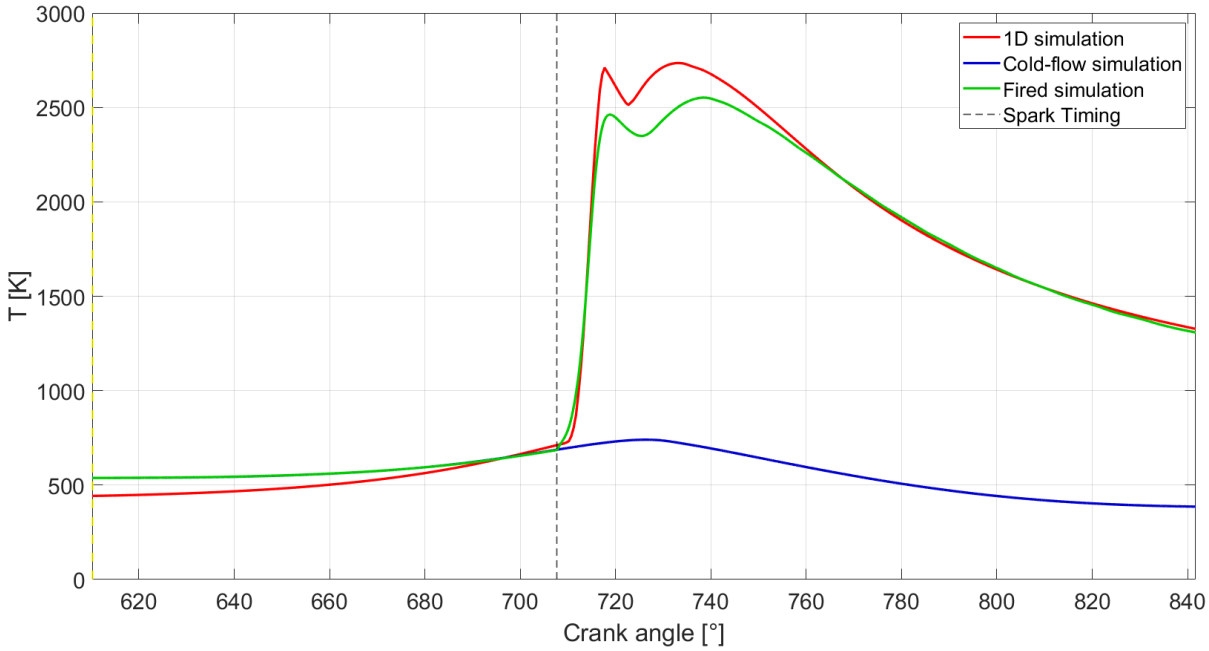

Figure 6.8: Fired cycle pre-chamber temperature curve: delayed spark timing

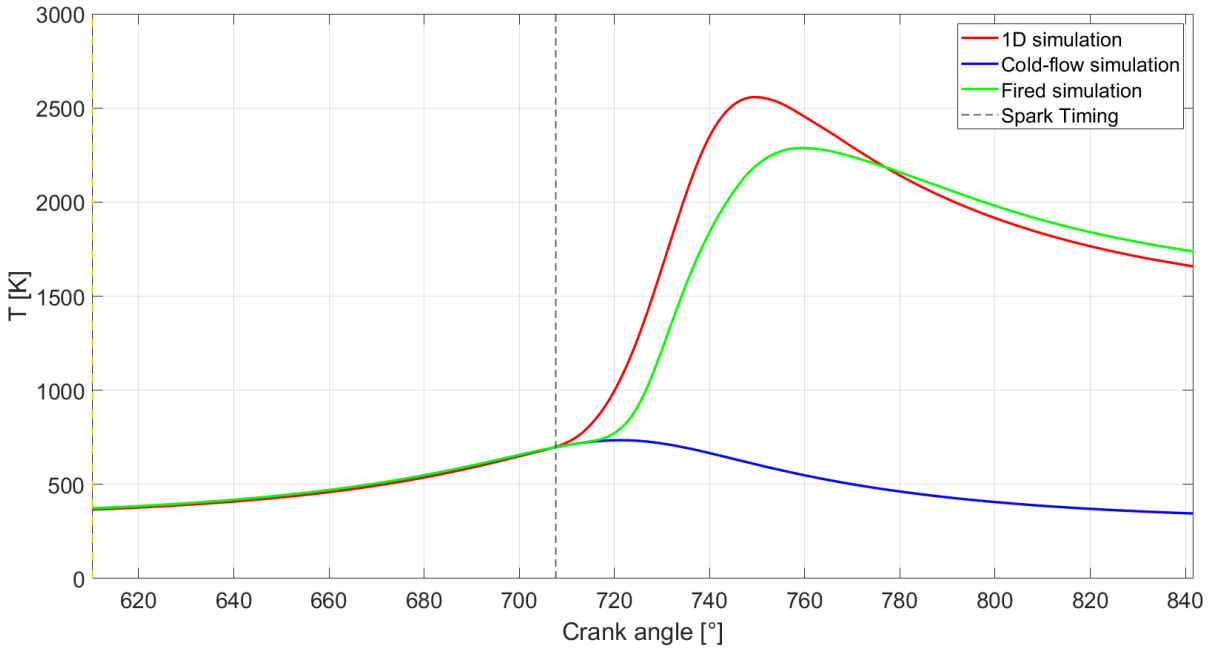

Figure 6.9: Fired cycle cylinder temperature curve: delayed spark timing

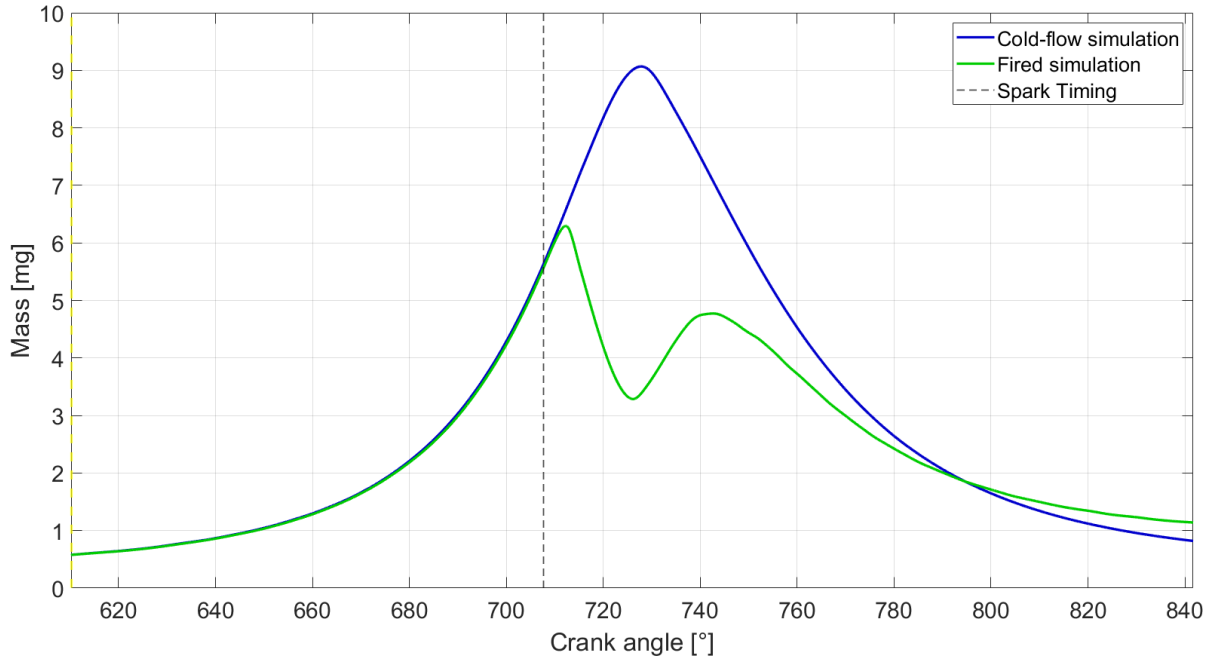

Figure 6.10: Fired cycle pre-chamber trapped mass: delayed spark timing

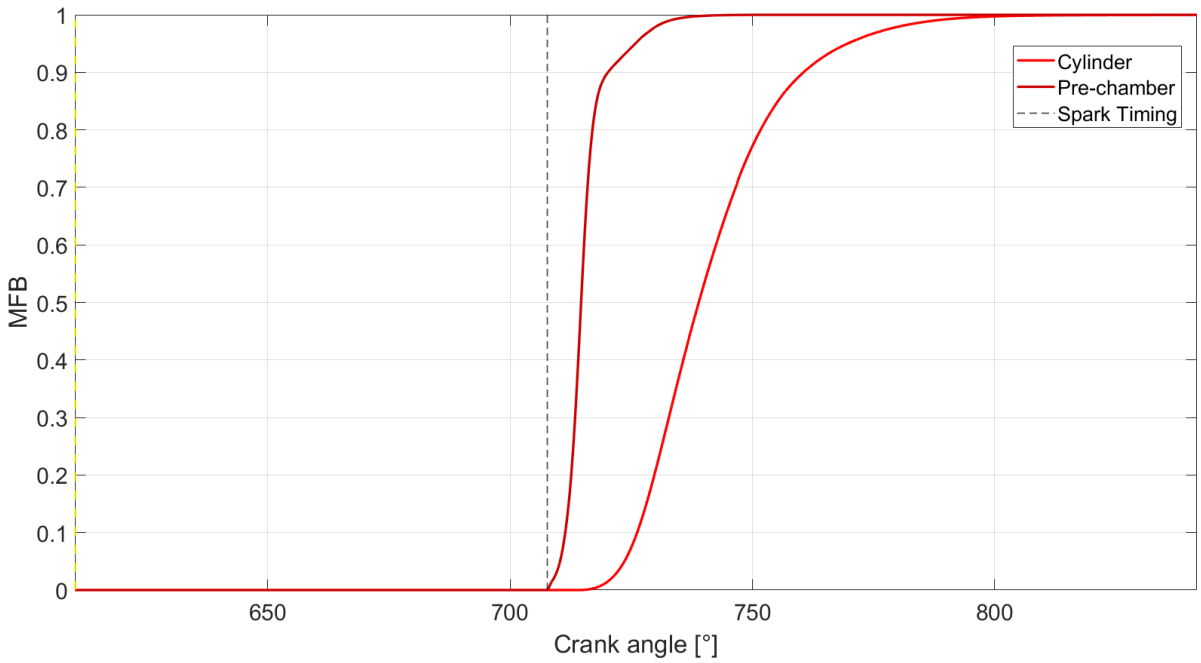

Figure 6.11: Mass Fraction Burned in cylinder and pre-chamber

Looking at Figure 6.6, it can be appreciated that the first pressure peak caused by the combustion inside the pre-chamber is now perfectly aligned with the pressure peak of the experimental curve. However, it is still lower, consequently causing weak jets that in turn lead to a delayed and low pressure peak in the main chamber (Figure 6.7). The second pressure peak inside the pre-chamber is caused by the burned gas entering inside it following the combustion process in the main chamber, therefore if the initial pressure trend inside the pre-chamber is not the desired one, of course also the second pressure peak will not be matched.

From Figure 6.10 it can be appreciated that the maximum value of mass trapped inside the pre-chamber is far from the maximum ideal value achieved in the cold-flow simulation. This is inevitable and caused by the fact that combustion must be initiated before the TDC to reach the MBT point, thus the mass trapped in the pre-chamber at the spark timing is burned and ejected from the orifices, preventing a further filling.

Figure 6.11 shows the trends of the MFB curves in pre-chamber and cylinder: clearly the mass inside the pre-chamber starts to burn earlier, since the mixture is first ignited there, and burns much more quickly, obviously because the volume where the flame front has to travel is much smaller compared to the main chamber volume.

In conclusion, it can be stated that if the combustion development inside the pre-chamber does not lead to a first pressure peak coherent with the one visible from the experimental data, it is natural that also the pressure curve inside the main chamber will not match the experimental trend (and consequently also the second pre-chamber pressure peak will be different).
The reasons behind the underestimation of the combustion intensity inside the pre-chamber must be investigated. The most likely cause could be an underestimation of the laminar flame speed by the combustion model, which might be caused by the fact that the semi-empirical correlations used to model the laminar flame speed might not be valid for the fluid conditions inside the pre-chamber. This assumption was done after looking at Figures 6.6 and 6.8, where it can be noticed that the initial slope of the simulated pressure and temperature curves in the pre-chamber caused by the mixture ignition is less sharp than the one of the experimental curves. Therefore, some more tests have to be carried out to understand what actions have to be taken to finally obtain the correct trend of the pre-chamber pressure curve.

6.2.1. Pre-chamber ignition combustion development

Even if the simulation results do not yet precisely reproduce the experimental data, it may be interesting to analyze the combustion development inside the pre-chamber and the consequent ejection process, in order to have a preliminary overview of the main characteristics of the TJI combustion.
It is important to analyze the flow behaviour inside the pre-chamber, to understand the motions generated during the filling process, because the velocity field has a significant influence on the combustion development right after the mixture ignition and consequently also on the ejection process of the burned gas from the pre-chamber to the main chamber.

The presence of a sort of tumble motion in pre-chamber, as shown in Figure 5.30a, has a significant influence on the flame front development, as it can be noticed by the following figure illustrating an instant few CAD after the spark timing. The quantity b represents the combustion regress variable, where 1 is fresh mixture and 0 is completely burned gas.

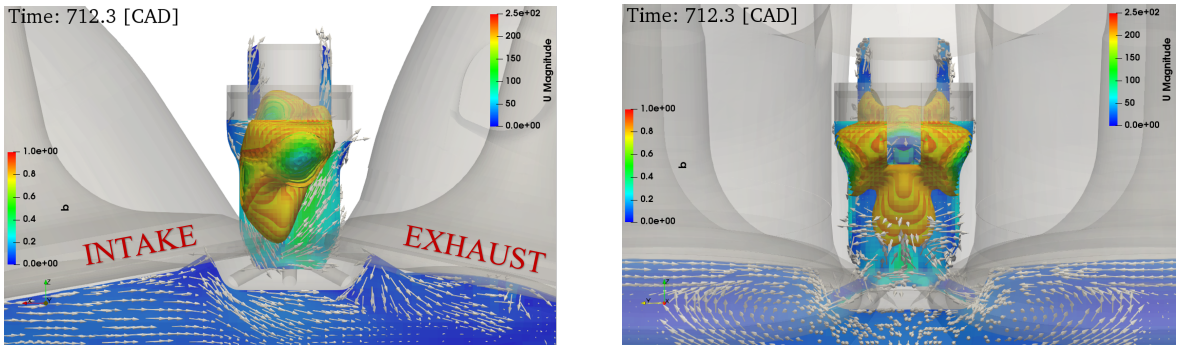

(a) Section on y-plane (b) Section on x-plane

Figure 6.12: Combustion development in pre-chamber

Figure 6.12a clearly shows that the combustion develops faster in the left side of the pre-chamber, due to the deformation of the initial flame front caused by the existing velocity field. Moreover, Figure 6.12b shows that also the space occupied by the spark plug electrode has an influence on the initial combustion phase, since the flame front develops around it, thus representing a further adversity to the combustion development in the right part of the pre-chamber.
This asymmetric development of combustion in the pre-chamber leads to the ejection of jets that have different penetrations into the main chamber. In particular, the two jets on the side of the pre-chamber facing the exhaust valves are ejected later and are weaker compared to the others, as can be seen from the following figure.

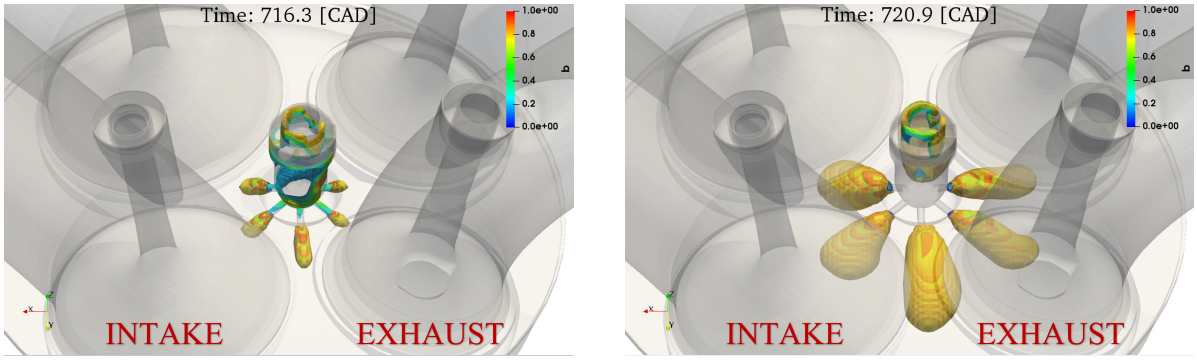

(a) (b)

Figure 6.13: Ejection process

Moreover, from Figure 6.13 it can be noticed that even the jets on the side of the pre-chamber facing the intake ducts have a lower penetration and higher diffusion compared to

the jets shooting between the intake and exhaust valves. A possible assumption to justify this issue is that once they come out from the pre-chamber they are facing a residual tumble motion in cylinder that probably tends to slow them down.
The different penetration and diffusion of each of the jets can be appreciated also looking at their marks on a section of the cylinder depicted in the following figure.

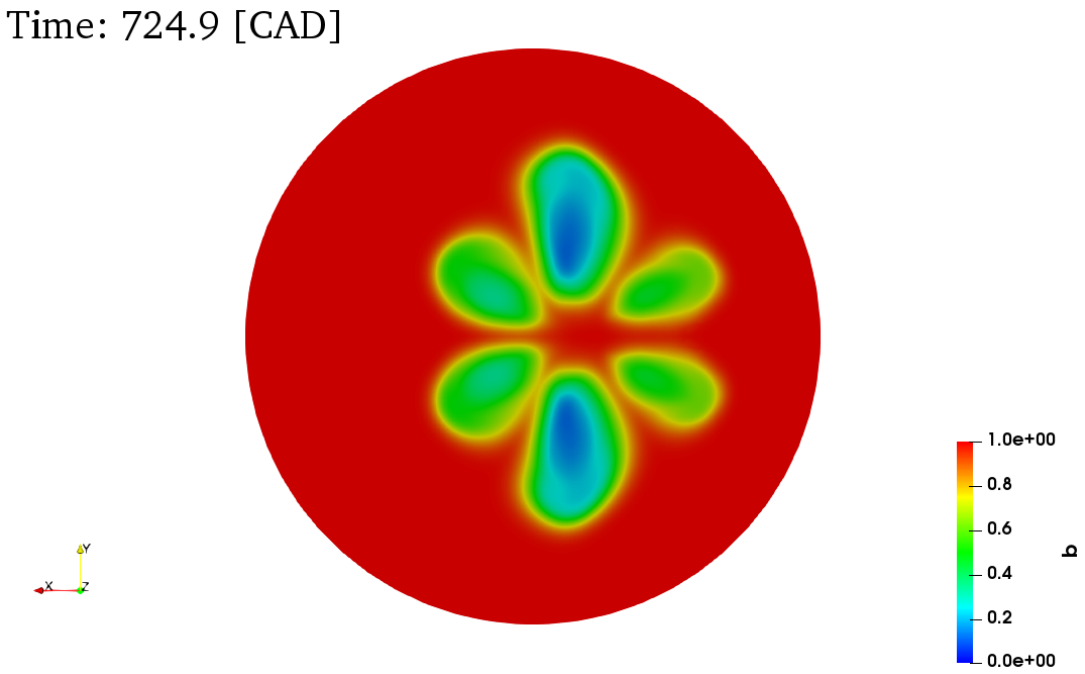

Figure 6.14: Ejection process: cylinder section

6.2.2. Heat transfer

The analysis of the heat transfer through the surfaces of both the pre- and main chambers allows to quantify which part of the combustion chamber walls provides the most significant contribution to the heat dissipation. This analysis is of specific importance for TJI engines, since their main drawback is probably related to the heat losses, which might prevent to improve the efficiency as much as desired.
The following figure shows the heat transfer contribution provided by the main combustion chamber walls.

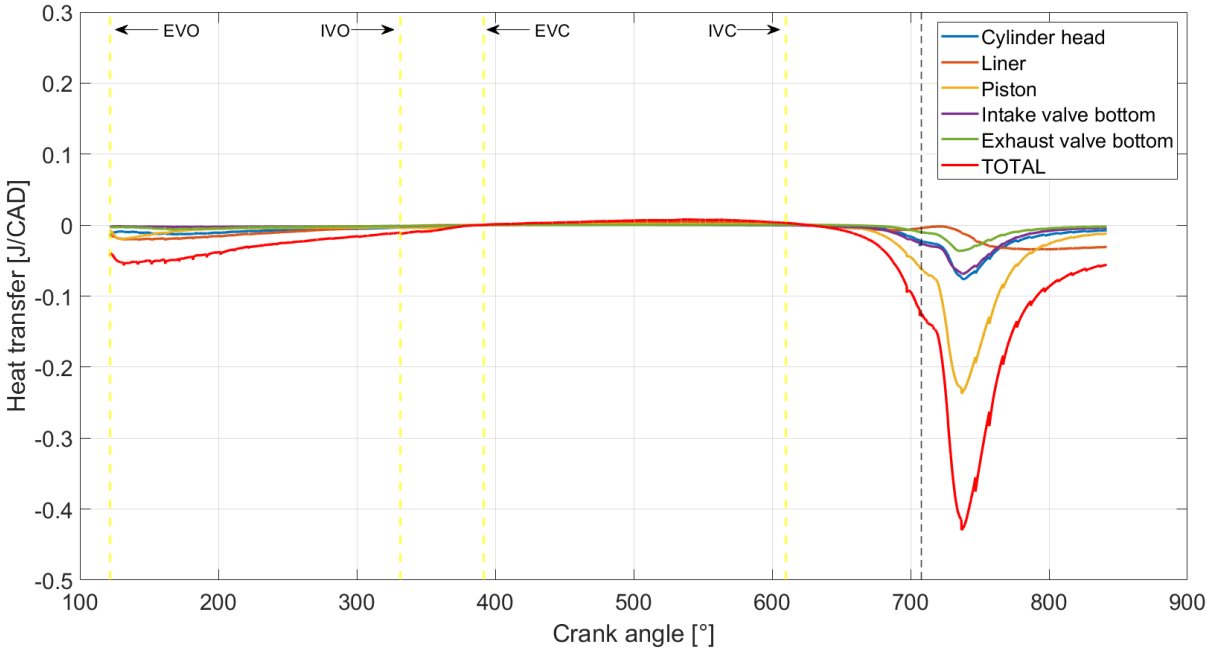

Figure 6.15: Heat transfer through the main chamber walls

Clearly, the highest heat losses are during the compression and expansion strokes, more specifically after the spark timing, when the temperature inside the main chamber is high because of combustion.

It can be noticed that the biggest contribution is given by the piston, because it is the widest surface among the ones represented in Figure 6.15 and also because the hot jets coming out from the pre-chamber are directly impinging against the piston (which is in the proximity of the TDC during the ejection phase), thus causing a significant heat loss. The liner has a negligible effect on the total heat losses, since when the temperature is very high the piston is close to the TDC, hence the liner surface is very small.

For what concerns the cylinder head, it might be interesting to sum the heat transfer through all the surfaces on the upper part of the combustion chamber (i.e. cylinder head, exhaust valve bottom and intake valve bottom), to better understand the contribution of the whole surface, which in this way has a similar extension as the piston, hence it is more straightforward to compare the heat loss through the surfaces defining the top and the bottom of the main chamber. The result of the summation can be seen in the following figure.

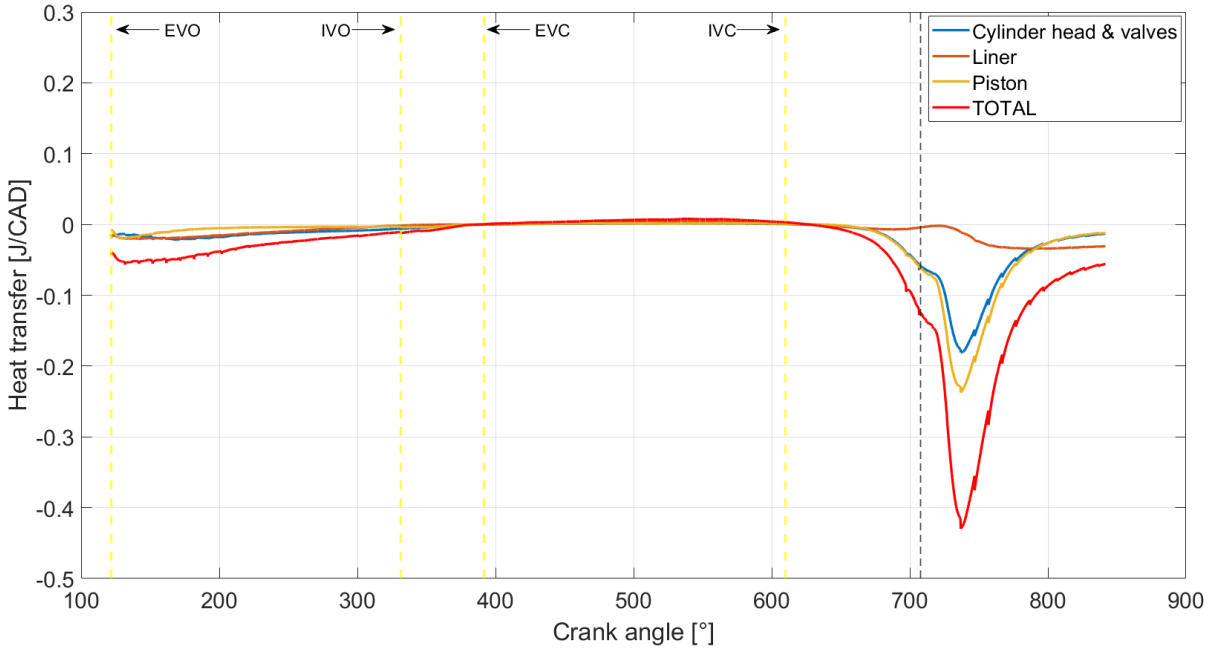

Figure 6.16: Heat transfer through the main chamber walls: sum of cylinder head and valves bottom

The contribution given by each surface of the cylinder to the total heat losses trough the main chamber walls is: 55% piston, 42% cylinder head and 3% liner.
Figure 6.16 proves that the heat loss through the piston surface (i.e. bottom part of the main chamber) is higher than the heat loss through the upper part of the combustion chamber, despite the greater extension of the latter surface since this engine is characterised by a pent-roof combustion chamber. It may be concluded that the difference between these two is caused by the heat loss resulting by the impingement of the hot jets on the piston during the ejection from the pre-chamber. The weight of this contribution can be roughly quantified as the heat transfer difference between the two surfaces, which is the 24% of the total heat transfer through the piston surface.

A similar chart as the one in Figure 6.15 was done also for the surfaces of the pre-chamber.

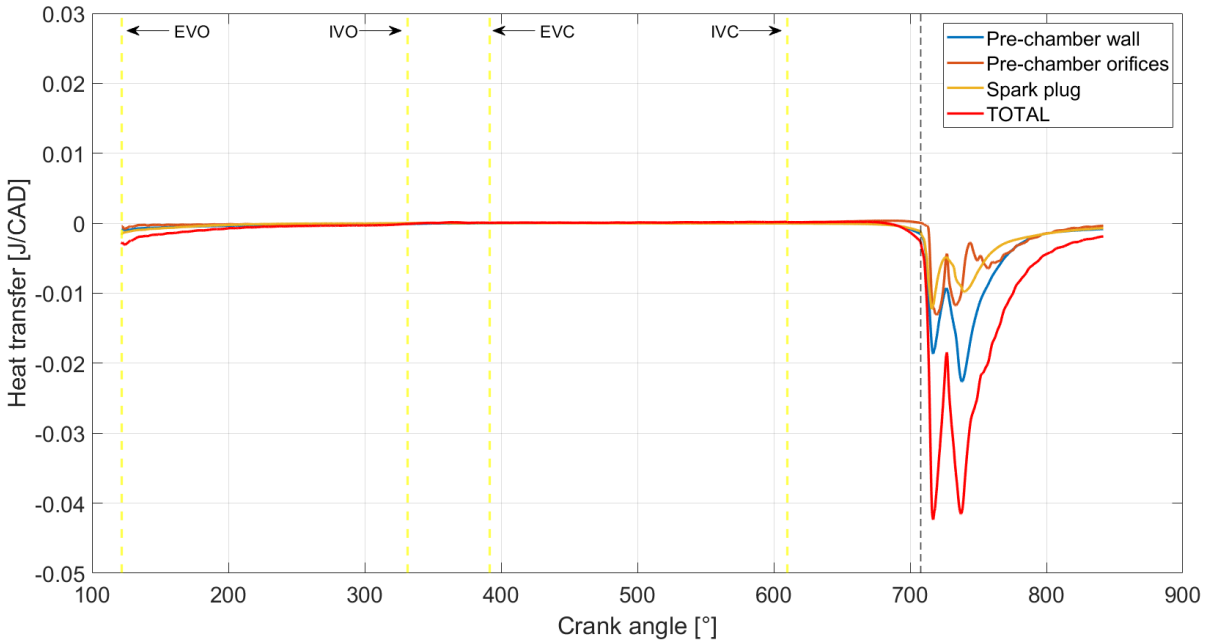

Figure 6.17: Heat transfer through the pre-chamber walls

Obviously for the pre-chamber the main share of the total heat losses is given by the pre-chamber wall, that constitutes without any doubt the widest surface. Nevertheless, it can be noticed that the contribution given by the pre-chamber orifices is even higher than the one given by the spark plug surface and, at the same time, not so far from that of the pre-chamber walls, despite the very low surface available for heat transfer. This is probably caused by a significant component of convective heat transfer, due to the high velocity of the flow when passing through the orifices.
It can be noticed that all the curves are characterised by two peaks: the first one is caused by the combustion in the pre-chamber, whereas the second one is caused by the hot residual gases pushed inside the pre-chamber after the combustion development in the main chamber.
More in detail, the contribution given by each surface to the total heat losses through the pre-chamber is:

- In correspondence of the first peak: 44% pre-chamber wall, 28.5% orifices and 27.5% spark plug.
- In correspondence of the second peak: 54% pre-chamber wall, 24.5% orifices and 21.5% spark plug.

The value of the second peak is very similar to the first one, however it is characterised by lower contributions given by spark plug and orifices. This is probably caused by the fact that the spark plug is more affected by heat transfer during the combustion inside the pre-chamber (i.e. first high temperature peak), since it is influenced by the flame kernel placed between the electrodes for the mixture ignition. Regarding the orifices, their contribution to the second peak is lower probably due to the lower velocity of the gas flowing through them, hence giving rise to a lower convective heat transfer compared to what happens when the gas flow out after the combustion inside the pre-chamber. The lower contribution of these two surfaces is compensated by the higher share given by the pre-chamber walls, which now are in contact with gas at higher temperature (see Figure 6.8) compared to what was happening for the first heat transfer peak.

In conclusion, the following figure shows the contributions to the total heat transfer of all the main chamber and pre-chamber walls summed together, to understand the weight of the heat losses through the pre-chamber walls over the total.

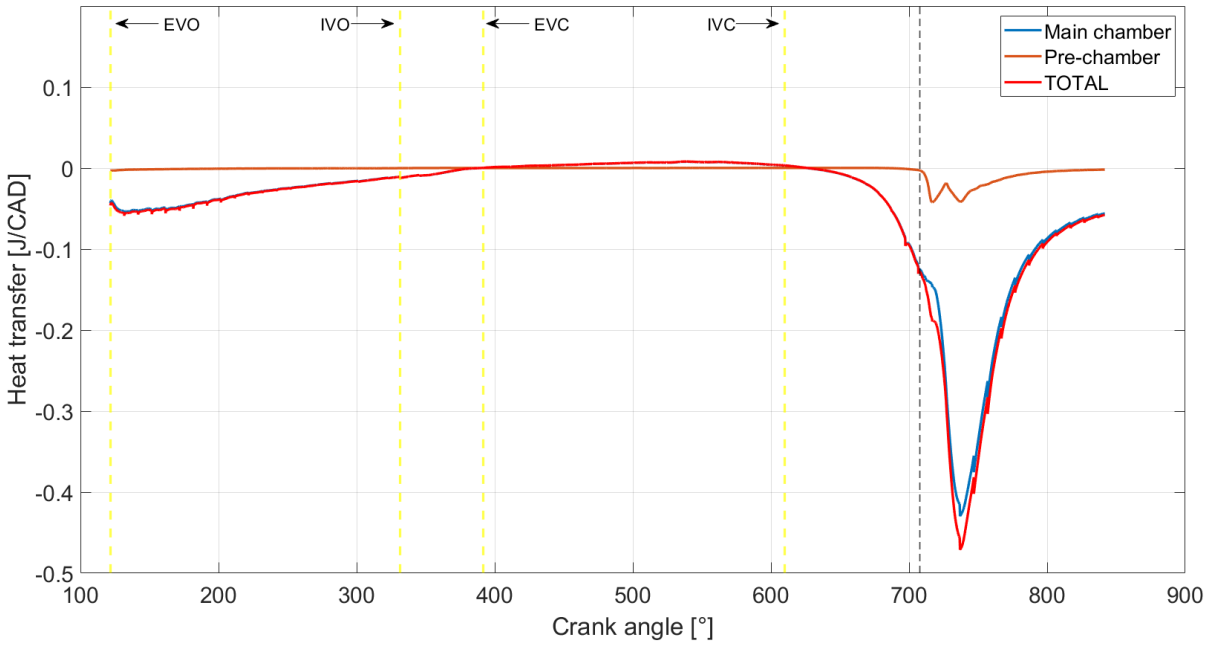

Figure 6.18: Heat transfer through the engine head walls

Figure 6.18 shows that the contribution of the heat rejection through the pre-chamber walls is small compared to the heat losses through the main chamber, but surely not negligible. In particular, the weight of the pre-chamber walls is of 8.8% over the total heat losses.

7 | Conclusions and future developments

This thesis work was focused on the full cycle simulation of a motorbike engine characterised by the application of a passive pre-chamber. The simulations were carried out with the open-source CFD software OpenFOAM, integrated with an additional library called LibICE, created by the ICE group at Politecnico di Milano with the specific purpose of performing CFD analyses on internal combustion engines.
The main goal was to obtain reliable results from the simulation, assessing their compatibility with the available experimental data. In this context, it is worth to take into account the uncertainties affecting both the signal acquisition on the test bench and the 1D simulation data used as boundary conditions for the 3D analysis, as well as the numerical errors inherently part of the CFD simulation itself. It was necessary to apply some minor modifications to the temperature initial and boundary conditions in order to precisely match the value of mass trapped in the engine found from the experiments, but eventually the trends of the most significant flow quantities resulting from the gas exchange simulation were considered as satisfactory. A thorough analysis was performed on the cold-flow simulation outcomes, with specific care given to the flow interaction between main chamber and pre-chamber.

For what concerns the numerical setup of the simulation, the following conclusions can be drawn:

- By applying mesh refinements only where required, it is possible to obtain satisfactory results with a rather limited number of cells (i.e. ranging approximately from 100k to 750k cells, with an average over the full engine cycle of 275k cells), thus with a limited computational effort (i.e. approximately 50 hours for a full cycle simulation with 16 cores).
- The tests carried out on the effect of the discretization schemes showed no dramatic variations in the simulation results by moving towards more accurate schemes, thus

proving the good quality of the employed mesh.

- It was demonstrated that for the discretization of the divergence terms in the turbulence model equations, a higher order scheme does not produce more accurate results. On the contrary, a first order scheme seemed to give the most realistic outputs.

For what concerns the cold-flow simulation results, the trend of all the analyzed flow quantities can be considered realistic and compatible with the experimental data, even if some considerations must be performed:

- Slight modifications to the temperature initial and boundary conditions had to be applied to improve the consistency with the experimental measurements. This proved that the 1D simulation data cannot be considered as fully reliable.
- The uncertainties on the experimental pressure traces prevent to obtain a perfect match with the simulated pressure curves. Indeed, the polytropic index investigation showed an inconsistent behaviour during the compression stage. In any case, the differences were considered as sufficiently small to be acceptable.
- The sensitivity analysis demonstrated the validity of the results obtained with the reference mesh, since the results obtained with the more refined mesh exhibited negligible differences. Moreover, the choice of exploiting the symmetry plane to simulate only half of the engine proved to be convenient, since all the results were extremely similar to the ones obtained with the entire engine mesh, with just one exception: the charge motions may be affected by the presence of the symmetry plane, thus this aspect must be taken into account for a correct analysis of the flows inside the cylinder.

The availability of reliable results from the cold-flow simulation was considered as an essential prerequisite to have a correct initialisation of the power-cycle simulation. However, an additional important variable is introduced when simulating combustion, which is the combustion modelling strategy. The results obtained from the power-cycle simulation were encouraging, even if not precisely reproducing the experimental pressure trace. Further work must be carried out to identify the cause of the underestimation of the laminar flame speed, in order to obtain a combustion behaviour more similar to the one exhibited by the experimental results. Moreover, since a novel approach implemented in the LibICE was used for simulating combustion, an assessment of the proposed methodology is needed, taking as benchmark a conventional SI engine for which an extended and robust experimental data set is available.

For what concerns the analysis of the flow inside the pre-chamber:

- It was demonstrated that the gas exchange process inside the pre-chamber weakly begins before the IVC. However, the filling process and the most important part of the pre-chamber scavenging take place only when the valves are completely close and the piston is moving towards the TDC.
- Due to the pre-chamber geometry characteristics, the scavenging process inside it is not as effective as it is in the main chamber, showing a concentration of residual gases trapped inside its volume at the spark timing six times higher compared to the mass fraction in the main chamber. Anyway, for the analysed engine, most of the residual gases were trapped in the upper part of the pre-chamber, above the spark plug electrodes, thus not negatively influencing the mixture ignition.
- The velocity field in the cylinder during the compression stroke causes a pre-chamber filling process more facilitated for the orifices facing the intake valves, thus giving rise to an asymmetric velocity field inside the pre-chamber. This, in turn, leads to an asymmetric combustion development caused by the convection of the flame front by the action of the velocity field.

The future work should be focused on finding a simulation setup featuring a more reliable combustion model for engines with a TJI combustion system. This achievement would allow to quantitatively estimate the main advantages and drawbacks of this technology, helping to understand how to optimize the engine characteristics for the various operative conditions, from both the fluid-dynamic and thermodynamic points of view. The final purpose is to maximize the benefits provided by a pre-chamber ignition for the application on future motorbike engines with increased efficiency.

Bibliography

[1] W. Attard, N. Fraser, P. Parsons, and E. Toulson. A turbulent jet ignition pre-chamber combustion system for large fuel economy improvements in a modern vehicle powertrain. In *SAE Technical Paper Series*. SAE International, 2010. doi: 10.4271/2010-01-1457.

[2] F. Bedogni, S. Magistrali, D. Mazzoni, E. Musu, G. Pivetti, and P. Zolesi. Gasoline internal combustion engine, with a combustion pre-chamber and two spark plugs, Mar. 2019.

[3] J. Benajes, R. Novella, J. Gomez-Soriano, P. Martinez-Hernandiz, C. Libert, and M. Dabiri. Evaluation of the passive pre-chamber ignition concept for future high compression ratio turbocharged spark-ignition engines. *Applied Energy*, 248:576–588, aug 2019. doi: 10.1016/j.apenergy.2019.04.131.

[4] A. Bianco, F. Millo, and A. Piano. Modelling of combustion and knock onset risk in a high-performance turbulent jet ignition engine. *Transportation Engineering*, 2 (trans-):100037, dec 2020. doi: 10.1016/j.treng.2020.100037.

[5] M. Bunce, H. Blaxill, W. Kulatilaka, and N. Jiang. The effects of turbulent jet characteristics on engine performance using a pre-chamber combustor. In *SAE Technical Paper Series*. SAE International, apr 2014. doi: 10.4271/2014-01-1195.

[6] K. Bureshaid, R. Shimura, H. Zhao, D. Feng, and M. Bunce. Investigation on knock resistance with turbulent jet ignition at different engine load in an optical engine. In *SAE Technical Paper Series*. SAE International, 2019. doi: 10.4271/2019-01-2151.

[7] A. Cooper, A. Harrington, M. Bassett, S. Reader, and M. Bunce. Application of the passive mahle jet ignition system and synergies with miller cycle and exhaust gas recirculation. In *SAE Technical Paper Series*. SAE International, 2020. doi: 10.4271/2020-01-0283.

[8] A. Cooper, A. Harrington, M. Bassett, and D. Pates. Knock mitigation benefits achieved through the application of passive mahle jet ignition enabling increased

output under stoichiometric operation. In *SAE Technical Paper Series*. SAE International, 2021. doi: 10.4271/2021-01-0477.

[9] G. D'Errico. *Slides of the course "Internal Combustion Engines"*. Politecnico di Milano, 2021.

[10] W. Duan, Z. Huang, H. Chen, P. Tang, L. Wang, and W. Chen. Effects of passive pre-chamber jet ignition on combustion and emission at gasoline engine. *Advances in Mechanical Engineering*, 13(12), dec 2021. doi: 10.1177/16878140211067148.

[11] J. H. Ferziger, M. Perić, and R. L. Street. *Computational Methods for Fluid Dynamics*. Springer, 4th edition, 2020.

[12] C. Greenshields. *OpenFOAM User Guide, Version 8*, 2020.

[13] L. Gussak, V. Karpov, and Y. Tikhonov. The application of lag-process in prechamber engines. 1980. doi: 10.4271/790692.

[14] J. Hua, L. Zhou, Q. Gao, Z. Feng, and H. Wei. Effects on cycle-to-cycle variations and knocking combustion of turbulent jet ignition (TJI) with a small volume prechamber. In *SAE Technical Paper Series*. SAE International, apr 2020. doi: 10.4271/2020-01-1119.

[15] M. Kettner, M. Rothe, A. Velji, U. Spicher, D. Kuhnert, and R. Latsch. A new flame jet concept to improve the inflammation of lean burn mixtures in si engines. *SAE Technical Paper Series*, 2005. doi: 10.4271/2005-01-3688.

[16] G. Montenegro and G. Persico. *Slides of the course "Modeling Techniques for Fluid Machines"*. Politecnico di Milano, 2022.

[17] R. Novella, J. Pastor, J. Gomez-Soriano, I. Barbery, C. Libert, F. Rampanarivo, C. Panagiotis, and M. Dabiri. Experimental and numerical analysis of passive prechamber ignition with EGR and air dilution for future generation passenger car engines. In *SAE Technical Paper Series*. SAE International, apr 2020. doi: 10.4271/2020-01-0238.

[18] R. Novella, J. Gomez-Soriano, P. Martinez-Hernandiz, C. Libert, and F. Rampanarivo. Improving the performance of the passive pre-chamber ignition concept for spark-ignition engines fueled with natural gas. *Fuel*, 290:119971, apr 2021. doi: 10.1016/j.fuel.2020.119971.

[19] T. Poinsot and D. Veynante. Theoretical and numerical combustion. *Prog. Energy Combust. Sci.*, 28, Jan. 2005.

[20] C. Robinet, P. Higelin, B. Moreau, O. Pajot, and J. Andrzejewski. A new firing concept for internal combustion engines: "l'apir". In *SAE Technical Paper Series*. SAE International, 1999. doi: 10.4271/1999-01-0621.

[21] P. Sementa, F. Catapano, S. D. Iorio, and B. M. Vaglieco. Effects of prechamber on efficiency improvement and emissions reduction of a SI engine fuelled with gasoline. In *SAE Technical Paper Series*. SAE International, oct 2019. doi: 10.4271/2019-24-0236.

[22] L. Sforza, T. Lucchini, G. Gianetti, and G. D'Errico. Development and validation of si combustion models for natural-gas heavy-duty engines. In *SAE Technical Paper Series*. SAE International, 2019. doi: 10.4271/2019-24-0096.

[23] L. Sforza, T. Lucchini, G. Gianetti, and G. D'Errico. A 3d-cfd methodology for combustion modeling in active prechamber si engines operating with natural gas. In *SAE Technical Paper Series*. SAE International, 2022. doi: 10.4271/2022-01-0470.

[24] M. Silva, S. Sanal, P. Hlaing, E. Cenker, B. Johansson, and H. G. Im. Effects of geometry on passive pre-chamber combustion characteristics. In *SAE Technical Paper Series*. SAE International, apr 2020. doi: 10.4271/2020-01-0821.

[25] A. Stadler, M. Wessoly, S. Blochum, M. Härtl, and G. Wachtmeister. Gasoline fueled pre-chamber ignition system for a light-duty passenger car engine with extended lean limit. *SAE International Journal of Engines*, 12(3):323–339, jun 2019. doi: 10.4271/03-12-03-0022.

[26] A. Stadler, H. Sauerland, M. Härtl, and G. Wachtmeister. The potential of gasoline fueled pre chamber ignition combined with elevated compression ratio. In *SAE Technical Paper Series*. SAE International, apr 2020. doi: 10.4271/2020-01-0279.

[27] E. Toulson, H. Schock, and W. Attard. A review of pre-chamber initiated jet ignition combustion systems. In *SAE Technical Paper Series*. SAE International, 2010. doi: 10.4271/2010-01-2263.

[28] H. Versteeg and W. Malalasekera. *An Introduction to Computational Fluid Dynamics THE FINITE VOLUME METHOD*. Pearson Education Limited, 2nd edition, 2007.

[29] S. Yamaguchi, N. Ohiwa, and T. Hasegawa. Ignition and burning process in a divided chamber bomb. *COMBUSTION AND FLAME*, 59:177–187, 1985. doi: 10.1016/0010-2180(85)90023-9.

[30] S. Zhu, S. Akehurst, A. Lewis, and H. Yuan. A review of the pre-chamber ignition sys-

tem applied on future low-carbon spark ignition engines. *Renewable and Sustainable Energy Reviews*, 154:111872, feb 2022. doi: 10.1016/j.rser.2021.111872.

A | Appendix A

The aim of this appendix is to give a clearer idea about the mathematical steps needed to move from a generic partial differential equation to its corresponding discretized linear equation that can be solved by a CFD code, topic briefly discussed in chapter 2, by means of a practical example. For the sake of simplicity, the shortest of the Navier-Stokes equations will be considered: the starting point is the continuity equation (2.4a) in its differential form.
The first step is to convert the differential equation into the integral form used in the finite volume method adopted by most of the CFD codes.

$$\frac{\partial \rho}{\partial t} + \boldsymbol{\nabla} \cdot (\rho \boldsymbol{U}) = 0 \qquad \Longrightarrow \qquad \frac{\partial}{\partial t} \oint_V \rho \, dV + \oint_S \rho \boldsymbol{U} \cdot \boldsymbol{n} \, dS = 0 \tag{A.1}$$

As it can be seen from equation (A.1), two integrals need to be discretized: a volume integral and a surface integral which in this case is representing the convective flux. No diffusive flux is present in the mass conservation equation and no surface or volume sources are considered.

For the purpose of this dissertation, the control volume V referred by equation (A.1) will be the volume of a generic cell with center P placed inside a regular 3D hexahedral mesh, thus featuring six neighbouring cells indicated with the letters of their centers N,S,E,W,T,B in figure A.1, that from now on will be all referred to with the generic letter i. Each of the neighbouring cells shares a face with cell P of surface S.

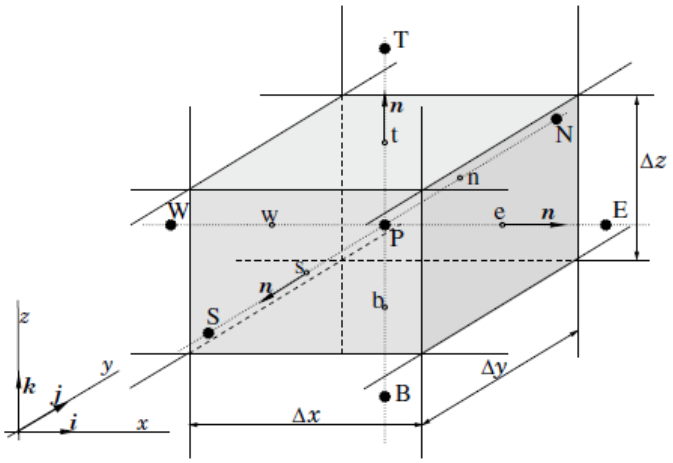

Figure A.1: Example of a generic cell P in a regular 3D mesh [11]

For the discretization of the volume integral the usual midpoint rule is chosen; for the time derivative, the most used approach is the Euler method, which is a first order scheme that takes advantage of the known value of the flow property at the previous time step.

$$\oint_V \frac{\partial \rho}{\partial t}\, dV = \left(\frac{\partial \rho}{\partial t}\right)_P V_P = \frac{{\rho_P}^{new} - {\rho_P}^{old}}{\Delta t} V_P \tag{A.2}$$

A midpoint rule discretization is chosen also for the surface integral and then, as an example, a linear scheme is used for computing the value of the flow property in the center of each face, in order to keep a global second order accuracy.

$$\begin{aligned} \oint_S \rho \boldsymbol{U} \cdot \boldsymbol{n}\, dS = \sum_{i=1}^{6} \rho_f U_n S = \sum_{i=1}^{6} U_n S(\zeta \rho_i + (1-\zeta)\rho_P) = \\ = 6 U_n S(1-\zeta)\rho_P + \sum_{i=1}^{6} U_n S \zeta \rho_i \end{aligned} \tag{A.3}$$

In this simplified example, it is supposed to use an implicit method for time advancement, therefore the value of the neighbouring cells are taken in the new time step. Nevertheless, the explicit method (i.e. values of the neighbouring cells taken in the old time step) is generally preferred for the CFD codes because it allows to obtain a diagonal matrix, thus saving a significant amount of computational time, even if it adds the necessity of checking the value of the Courant number.
By combining equations (A.2) and (A.3), the final discretized form of equation (A.1) is obtained:

$$\left(\frac{V_P}{\Delta t} + 6U_n S(1-\zeta)\right)\rho_P + \sum_{i=1}^{6}(U_n S\zeta)\rho_i = \left(\frac{V_P}{\Delta t}\right){\rho_P}^{old} \tag{A.4}$$

The term multiplied by ρ_P goes on the diagonal of the matrix, whereas each of the terms multiplying the density value in the neighbouring cells constitutes the off-diagonal components of the matrix; all the terms multiplied by a value of the density referred to an old time step go into the vector of known terms. Equation (A.4) finally leads to the linear system:

$$[A]\boldsymbol{\rho} = \boldsymbol{Q} \tag{A.5}$$

In this very simple example just a couple of integrals had to be discretized. For more complex equations a greater number of terms will have to be treated (e.g. momentum conservation equation, turbulent kinetic energy equation, ...), sometimes also including diffusive flux terms featuring a gradient of the diffusive property that also needs its own discretization scheme.
Furthermore, in this case a very regular mesh was considered (i.e. perfectly orthogonal, not skewed); in real problems the mesh irregularities must be taken into account, since they cause the presence of additional contributions generally to be joined to the vector of known terms $\boldsymbol{Q}$.

The procedure explained above is performed for all the equations needed to model the flow behaviour in all the cells composing the mesh, finally leading to a number of linear systems equal to the number of fluid flow equations to be solved (e.g. 7 in case a $k-\varepsilon$ turbulence model is used: 5 RANS equations + 2 turbulence model equations), each of them formed by a matrix with a rank equal to the number of cells of the mesh.
Different algorithms can be used to compute the value of the flow properties sequentially solving all the equations, depending on the type of problem: steady-state or transient, compressible or incompressible, ...
One of the most well-known algorithms, also available in the OpenFOAM CFD code used in the present thesis work, is the PIMPLE algorithm, which is a segregated pressure-based transient solver that can be used also for turbulent compressible flows.

List of Figures

List of Tables

List of Symbols

Variable	Description	SI unit
$\boldsymbol{t}$	Time	s
$\boldsymbol{\rho}$	Density	kg/m^3
$\boldsymbol{U}$	Velocity	m/s
$\boldsymbol{g}$	Gravity acceleration	m/s^2
$\bar{\bar{\boldsymbol{\sigma}}}$	Internal stress tensor	N/m^2
$\boldsymbol{p}$	Pressure	N/m^2
$\bar{\bar{\boldsymbol{\tau}}}$	Shear stress tensor	N/m^2
$\boldsymbol{E}$	Total energy	J
$\boldsymbol{\kappa}$	Thermal conductivity	$W/(m \cdot K)$
$\boldsymbol{T}$	Temperature	K
$\boldsymbol{q}_H$	Heat source	W/m
$\boldsymbol{\mu}$	Dynamic viscosity	$(N \cdot s)/m^2$
$\boldsymbol{H}$	Enthalpy	J
$\boldsymbol{u}$	Internal energy	J
$\boldsymbol{R}$	Specific gas constant	$J/(kg \cdot K)$
$\boldsymbol{c}_p$	Specific heat capacity at constant pressure	$J/(kg \cdot K)$
$\boldsymbol{C}_p$	Heat capacity at constant pressure	J/K
$\boldsymbol{S}_\mu$	Sutherland constant	K
$\boldsymbol{\mu}_T$	Turbulent viscosity	$(N \cdot s)/m^2$
$\boldsymbol{\kappa}_T$	Turbulent thermal diffusivity	$W/(m \cdot K)$
$\boldsymbol{u}_T$	Turbulent velocity scale	m/s
$\boldsymbol{l}_T$	Turbulent length scale	m
$\boldsymbol{k}$	Turbulent kinetic energy	m^2/s^2
$\boldsymbol{\varepsilon}$	Turbulent dissipation rate	m^2/s^3

Variable	Description	SI unit
$\boldsymbol{Y}_k$	Mass fraction of chemical species k	$kg_k/kg_{mixture}$
$\boldsymbol{V}_k$	Diffusion velocity chemical species k	m/s
$\dot{\boldsymbol{\omega}}_k$	Reaction rate chemical species k	W/m
$\boldsymbol{b}$	Unburned mass fraction	$kg_{unburned}/kg_{burned}$
$\boldsymbol{\Xi}$	Flame wrinkle factor	$-$
$\boldsymbol{S}_u$	Unstrained laminar flame speed	m/s
$\boldsymbol{S}_t$	Turbulent flame speed	m/s
$\boldsymbol{\rho}_u$	Unburned gas density	kg/m^3
$\boldsymbol{C}_s$	Ignition strength	$-$
$\boldsymbol{\Delta t}_{ign}$	Ignition duration	s
$\boldsymbol{r}_k$	Flame kernel radius	m
$\boldsymbol{\delta}_l$	Laminar flame thickness	m
$\boldsymbol{\phi}$	Equivalence ratio	$-$
$\boldsymbol{V}$	Cell volume	m^3
$\boldsymbol{S}$	Cell face surface	m^2
$\boldsymbol{\Phi}$	Generic flow quantity	$-$
$\boldsymbol{n}$	Surface normal vector	$-$
$\boldsymbol{q}_V$	Volume source	W/m
$\boldsymbol{q}_S$	Surface source	W/m
$\boldsymbol{x}$	Generic coordinate of a point in a cell	m
$\boldsymbol{\zeta}$	Normalized distance from cell face to centroid P	$-$
$\boldsymbol{rpm}$	Revolutions per minute	s^{-1}
$\boldsymbol{\lambda}$	Equivalent air-to-fuel mass ratio	$-$
$\boldsymbol{y}^+$	Non-dimensional wall distance	$-$
$\boldsymbol{\Delta t}$	Simulation time step	s
$\boldsymbol{\Delta x}$	Mesh spacing	m
$\boldsymbol{U'}$	Fluctuating component of the flow velocity	m/s
$\boldsymbol{I}$	Turbulence intensity	$-$
$\boldsymbol{c}_v$	Specific heat capacity at constant volume	$J/(kg \cdot K)$
$\boldsymbol{\gamma}$	Ratio of specific heats	$-$

List of Abbreviations

Abbreviation	Meaning
CFD	Computational Fluid Dynamics
RANS	Reynolds Average Navier-Stokes
TJI	Turbulent Jet Ignition
SI	Spark Ignition
CI	Compression Ignition
PFI	Port Fuel Injection
DI	Direct Injection
MFB	Mass Fraction Burned
IMEP	Indicated Mean Effective Pressure
MBT	Maximum Brake Torque
CAD	Crank Angle Degree
TDC	Top Dead Center
BDC	Bottom Dead Center
STL	Standard Triangulation Language
EVO	Exhaust Valve Opening
EVC	Exhaust Valve Closing
IVO	Intake Valve Opening
IVC	Intake Valve Closing
ECU	Electronic Control Unit